Infulence of atmospheric stability on the spatial structure of turbulence

Chougule, Abhijit S.; Mann, Jakob; Kelly, Mark C.

Publication date:
2013

Document Version
Publisher's PDF, also known as Version of record

Citation (APA):
Chougule, A. S., Mann, J., & Kelly, M. C. (2013). Infulence of atmospheric stability on the spatial structure of turbulence. Kgs. Lyngby: Technical University of Denmark (DTU).

Influence of atmospheric stability on the spatial structure of turbulence

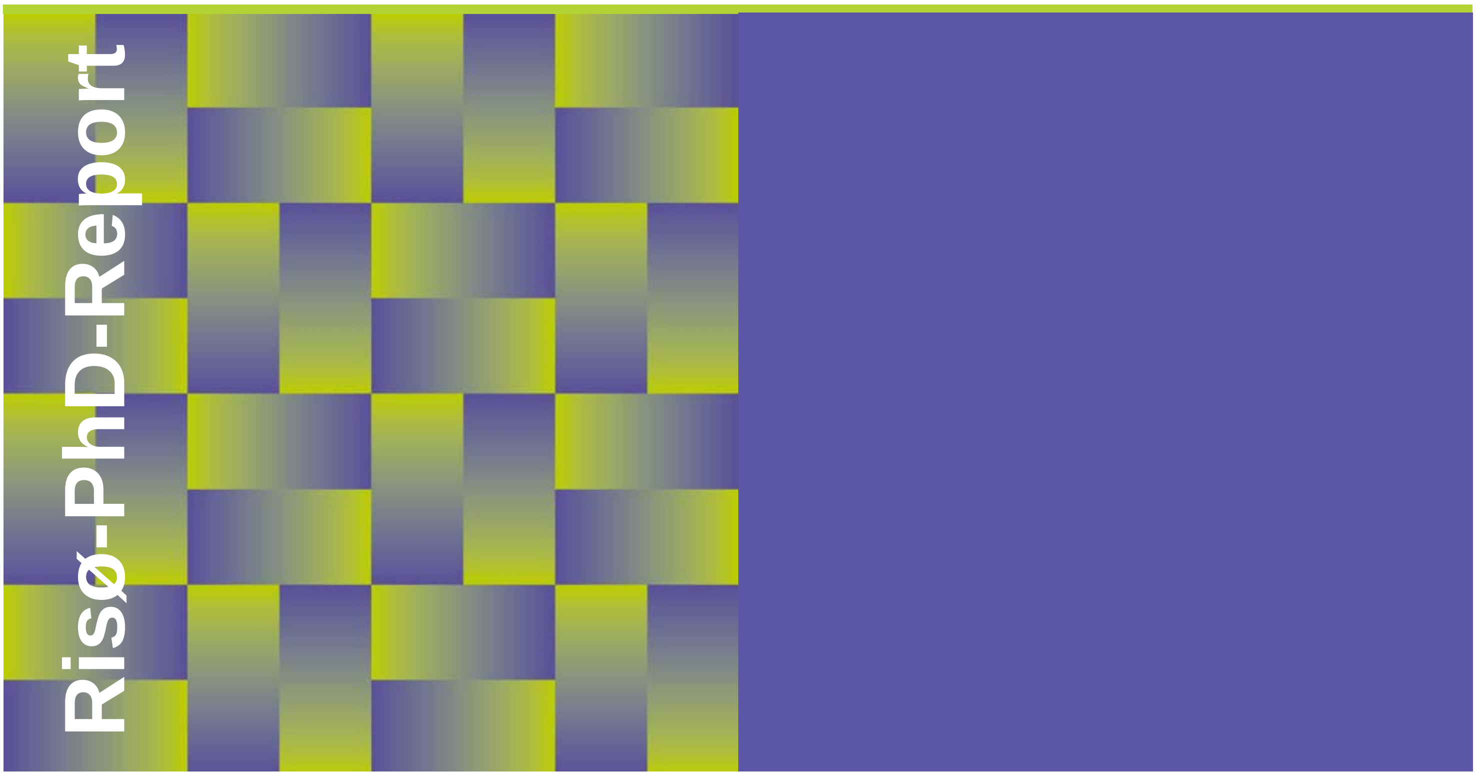

Abhijit Chougule
Risø-PhD-xxx(EN)
May 2013

DTU Wind Energy
Department of Wind Energy

Influence of atmospheric stability on the spatial structure of turbulence

Abhijit Chougule

Roskilde 2013
DTU Wind Energy-PhD-xxx(EN)

Acknowledgements

One summer day of April 2010, my supervisor and co-supervisor were just about to *play dice*, in order to explain me probability, and, that was just the begining of my PhD. I could not have imagined being at the better place with the better people during my PhD study in *turbulence*.

I would like to express my sincere gratitude to my advisor Prof. Jakob Mann for the continuous support of my PhD study and research. Jakob's patience, motivation, enthusiasm, and immense knowledge helped me in all the time of research and writing of this thesis. I also owe thanks to Jakob for helping me in understanding of his model, though, there is still a lot to learn about.

Spacial thanks to Mark Kelly, my co-advisor, with whom I enjoyed a lot discussing on the PhD subject, especially on rapid distortion theory. Our discussions have always inspired me in what I was doing. I also thank Mark for his petience in correcting my English.

Thanks to Jacob Berg for helping me with C++ coding, in his way, which actually helped me to learn many things in a very short period of time. I have also enjoyed a teaching assitanceship with Jacob, which brought me the level of confidence in my PhD.

Many thanks to Dr. Donald H. Lenschow for my four and half months stay at the National Center for Atmospheric Research (NCAR). Don's interest and criticisms made me to try out many different forms of the model parameters in Chapter 3.

Many thanks to my old officemates, PhD colleagues, for helping me with many practical things. I also thank Ameya sathe for sharing with me his knowledge and experience in the field of Wind Energy.

I would also like to thank Claus and Lis, for their generous support and care. I must admit that it was huge moral and emotional support for me to have friends like them in Denmark. I thank Claus and Lis for all the great moments that we shared together.

I acknowledge the financial support from the Siemens Wind Power A/S and the WindScanner.dk project, which was funded by the Danish Agency for Science.

I take this opportunity to give my warmest thanks to my parents for their support in all my pursuits and for the education they gave me. And finally, to Sonal– for patience and everything else.

Author: Abhijit Chougule
Title: Influence of atmospheric stability on the spatial structure of turbulence
Department: DTU Wind Energy

Abstract:

This thesis consists of three chapters. In the first chapter, the cross-spectral phases between velocity components at two heights are analyzed from observations at the Høvsøre test site under diabatic conditions. These phases represent the degree to which turbulence sensed at one height leads (or lags) in time the turbulence sensed at the other height. The phase angle of the cross-wind component is observed to be significantly greater than the phase for the along-wind component, which in turn is greater than the phase for the vertical component. The cross-wind and along-wind phases increase with stream-wise wavenumber and vertical separation distance, but there is no significant change in the phase angle of vertical velocity. The phase angles for all atmospheric stabilities show similar order in phasing. The phase angles from the Høvsøre observations under neutral conditions are compared with a rapid distortion theory model, which shows similar order in phase shift.

In the second chapter, a velocity spectral tensor model was evaluated using single point measurements of wind speed. The model contains three parameters, representing the dissipation rate of specific turbulent kinetic energy, a turbulence length scale and the turbulence anisotropy, respectively. Sonic anemometer measurements taken over a forested and an agricultural landscape were used to calculate the model parameters for neutral, slightly stable and slightly unstable atmospheric conditions over a selected wind speed interval. The dissipation rate above the forest was 9 times that at the agricultural site. No significant differences were observed in the turbulence length scales between the forested and agricultural areas. A small difference was observed in the turbulence anisotropy at the two sites, except near the surface, where the forest turbulence was more isotropic. The turbulence anisotropy remained more or less constant with height at the forest site, whereas the turbulence became more isotropic with height for the agricultural site. Using the three parameters as inputs, we quantified the performance of the model in coherence predictions for vertical separations. The model coherences of all the three velocity components were overestimated for the analyzed stability classes at both the sites. The model performed better at both sites for neutral stability than slightly stable and unstable conditions. The model predictions of coherence of the along-wind and vertical components were better than that of the cross-wind component. No significant difference was found between the performance of the model at the forested and the agricultural areas.

The last chapter summarizes the present state of the theory, in which an attempt is made to investigate the spectral tensor model of both wind velocity and temperature fluctuations, which treats the effects of mean uniform vertical shear and mean uniform temperature gradient. The model is based on rapid distortion theory, which gives the linearized Navier-Stokes equations in Fourier space. We incorporate the general concept of an eddy life time in order to make the model stationary. The parameterized eddy life time from Mann (1994) is used. In addition to the three parameters from the spectral tensor model of Mann (1994), the model contains two extra parameters as a result of introducing a mean uniform temperature gradient. These parameters are: a stability parameter in the form of the Richardson number, and a measure of the rate of destruction of temperature variance. The model seems to work better for stable than unstable conditions. The model is able to predict well the length scales (corresponding to the peaks of (co-) spectra) of the temperature spectrum and temperature-velocity co-spectra. In the intertial subrange, the model shows that the velocity-temperature co-spectra are proportional to the $-7/3$ power of streamwise wavenumber, which is consistent with the measurements. The model is able to predict the temperature-coherence, moreso in the stable case than in the unstable case. We compare the model predictions against those of Mann (1994) in the coherence estimations, where the new model seems to give slightly improved results.

The thesis is submitted to the Danish Technical University in partial fulfilment of the requirements for the PhD degree.

Risø-PhD-XX(EN)
May 2013

ISBN
XXXXXXXXXXXXXXXXX

Contract no.:

Group's own reg. no.:

Sponsorship:
XXXXXXXXXX
XXXXXXXXXX

Pages:XX
References:XX

Information Service Department
RisøNational Laboratory for
Sustainable Energy
Technical University of Denmark
P.O.Box 49
DK-4000 Roskilde
Denmark
Telephone +45 46774005
bibl@risoe.dtu.dk
Fax +45 46774013
www.risoe.dtu.dk

Forfatter: Abhijit Chougule
Titel: Indflydelse af atmosfærisk stabilitet på den rumlige struktur af turbulens
Institut: DTU Vindenergi

Dansk Resumé:

Denne afhandling har tre kapitler. I det første kapitel behandles kryds-spektrale faser mellem vindhastighedskomposanter målt i to forskellige højder. Vindhastighederne er målt ved det nationale testcenter ved Høvsøre under ikke-neutrale, d.v.s. diabatiske atmosfæriske forhold. Disse faser udtrykker i hvor høj grad turbulens målt i den ene højde er foran eller bagud turbulens i den anden højde. Fasevinklen for tværkomposanten af vinden ses at være betydeligt større end for vindfluktuationerne i middelvindsretningen som igen er større en fasevinklen for den vertikale komposant. Faserne for komposanterne på tværs og langs af middelvindretningen vokser med bølgetallet og den vertikale højdeforskel, mens fasen for de vertikale fluktuationer ikke ændrer sig synderligt med disse parametre. Fasevinkler for alle atmosfæriske lagdelinger udviser stort set samme opførsel. Fasevinklerne for neutral atmosfærisk lagdeling bliver sammenlignet med en "rapid distortion" teori, som viser den samme rækkefølge af faserne som observationerne.

I det anden kapitel vurderes en model for den spektrale hastighedstensor udfra et-punktsmålinger af vinden. Modellen indeholder tre parametre, som repræsenterer destruktionsraten af den specifikke turbulente kinetiske energi, en længdeskala for turbulensen samt et mål for turbulensens anisotropi. Målinger foretaget med soniske anemometre over skov og landbrugsland er blevet brugt til at beregne modellens parametre for neutral, let stabil of let ustabil atmosfærisk lagdeling for et bestemt hastighedsinterval. Destruktionsraten af energi over skoven var 9 gange højere end over landbrugsområdet. Ingen betydelig forskel på turbulensens længdeskala blev observeret over de to typer terræn. Der var heller ikke forskelle på graden af anisotropi på de to steder med undtagelse at tæt på overfladen, hvor turbulensen over skoven var lidt mere isotrop. Turbulens anisotropien var nogenlunde konstant med højden over skoven, mens den faldt let over landbrugslandet. Ved brug af de fundne parametre kvantificeredes modellens evne til at forudsige kohærens mellem vertikalt adskilte målinger. Modellen overestimerede kohærensen for alle tre hastighedskomposanter ved begge steder for de analyserede stabilitetsklasser. Modellen gav bedre forudsigelser for neutral stabilitet, end for let stabil og ustabil lagdeling. Modellens forudsigelser var bedre for fluktuationer i middelvindens retning og i den vertikale retning end for tværkomposanten. Der var ingen betydelig forskel på modellens præstation over de to terræn typer.

Det sidste kapitel opsummerer status for en spektral tensormodel i hvilken de fysiske effekter på turbulensen af både shear og temperaturlagdeling er modelleret. Modellen er baseret på "rapid distortion" teori, som bruger de lineariserede Navier-Stokes ligninger i Fourier-rummet. Begrebet hvirvellevetid er brugt til at give de lineære ligninger en stationær løsning. Den parametriserede hvirvellevetid fra Mann (1994) er brugt. Udover de tre parametre fra Mann's (1994) spektrale tensormodel indeholder modellen to ekstra parametre som en konsekvens af indførslen af temperaturvariationerne. Disse parametre er Richardson-tallet, som er en stabilitetsparameter, samt et mål for destruktionsraten af turbulente temperaturfluktuationer. Modellen ser ud til at virke bedre for stabile end for ustabile atmosfæriske tilstande. Modellen er i stand til at estimere længdeskalaerne for temperatur spektre og temperatur-hastigheds kryds-spektrene godt. I det inertielle underområde (inertial subrange) viser modellen at hastigheds-temperatur kryds-spektrene er proportionelle med bølgetallet i strømningsretningen opløftet til potensen $-7/3$, hvilket er foreneligt med observationerne. Modellen kan forudsige temperatur kohærenser, dog med større held for stabil lagdeling end for ustabil. Modellens forudsigelser af kohærenser sammenlignes med dem fra Mann (1994), og den nye model giver let forbedrede resultater.

Contents

List of Figures

Chapter 1

Vertical cross-spectral phases in atmospheric flow

1.1 Introduction

The structure of atmospheric turbulence can be analysed in terms of two-point statistics such as normalized cross-spectra (also known as coherences), which are typically studied both experimentally and theoretically as a function of horizontal separation distance for homogeneous turbulence in the atmospheric surface-layer (Mann [1994a]; Tong and Wyngaard [1996]). The coherences of the along-wind, cross-wind and vertical velocity components (u, v, w) decrease with increasing separation distance, as seen from both observations and theory (Mann [1994a]).

In this paper[1] we investigate cross-spectra with particular emphasis on the associated phases φ for vertical separations Δz, using observations at Høvsøre under diabatic conditions (Sathe et al. [2012]). Chougule et al. [2012][2] studied the vertical phase angles for all three velocity components (i.e. φ_u, φ_v and φ_w), including their behavior in the neutral, horizontally homogeneous atmospheric boundary layer (ABL) using measurement from Høvsøre and Cooperative Atmosphere-Surface Exchange Study in 1999 (CASES-99) (Poulos et al. [2002]; Sun et al. [2002]). Mann [1994a] studied φ_{vw}

---

[1] This paper, co-authored with J. Mann and M. Kelly, was presented in conference proceedings of The Science of Making Torque from Wind, Oldenburg 2012.

[2] The paper titled “Vertical cross-spectral phases in neutral atmospheric flow” based on this study is published in the *J. Turb.* co-authored by J. Mann, M. Kelly, J. Sun, D. H. Lenschow and E. G. Patton. (c. f. Appdx A)

(the phase angle between v and w) for horizontal separations, and $\varphi_{uu}(\equiv \varphi_u)$ and φ_{uw} for vertical separations where the w-component was measured further from the surface. Few experimental investigations have been done on the phases. Heidrick et al. [1977] experimentally studied the phases of the axial velocity component in fully developed pipe flow using measurements taken at two different points, where the separation vector was oriented at different angles to the mean flow. Komori et al. [1983] studied the phase angle between the vertical velocity-component and temperature in stably-stratified open-channel flow. Both Heidrick et al. [1977] and Komori et al. [1983] assumed turbulent motions approach as wavelike motions. The Sandia (Veers) method from Veers [1988], which is used in wind engineering for load calculations on wind turbines, assumes an average of zero phase between any two points because of an exponential form of the coherence function as given in Ref. Veers [1984]. The method in Mann [1998], based on the Mann spectral tensor model from Mann [1994a] and widely used in wind engineering, does give non-zero phases.

In addition to the observations, we also evaluate the phase angles from the Mann spectral tensor model, which incorporates rapid distortion theory (RDT) (Pope [2000]; Townsend [1976]). The phases are determined by calculating the two-point cross-spectra of velocity components and corresponding spectra as defined in Section 1.1.2. The observations and the model used for the analysis are described in Section 1.2 and Section 1.3, respectively. The results from the observations and the RDT model are given in Section 1.4. In Section 1.5, we discuss more details, followed by conclusions in Section 6.

1.1.1 Motivation

Mann [1994a] modeled the evolution of turbulence induced by uniform shear using RDT in a neutral surface-layer. Mann [1998] used the model of Mann [1994a] to develop a method to simulate the three-dimensional wind in the time domain. The model in Mann [1994a] and the method in Mann [1998] are the industry standards for aero-elastic calculation of wind turbine loads (IEC [2005]). Turbulence simulations from Mann [1998] show systematic behavior in u, v and w fluctuations in the rotor plane of a horizontal axis wind turbine, and when used to predict the respective phase angles between two heights, we see that $\varphi_v > \varphi_u > \varphi_w$ for $k_1 \Delta z \leq 1$, where k_1 is stream-wise wavenumber. We expect that this behaviour in phasing is due to the vertical shear as depicted in Figure 1.1.

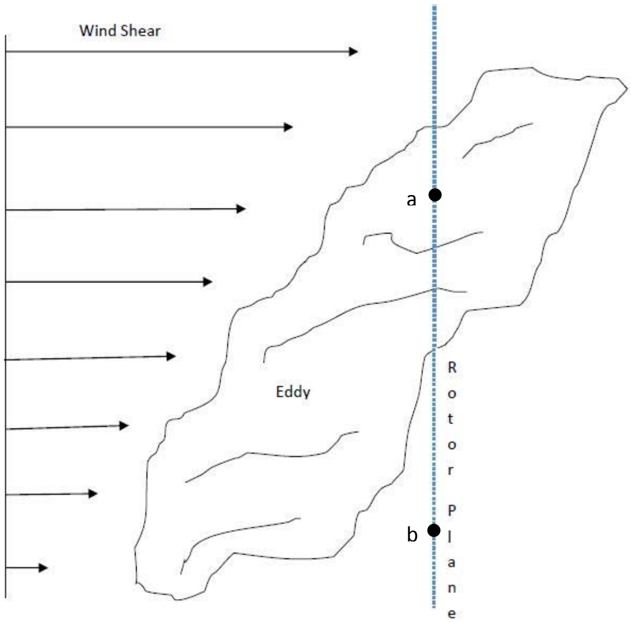

Figure 1.1: Sketch of the eddy stretching due to the shear. The turbulence sensed at point **a** leads in phase with respect to the turbulence sensed at point **b** in the rotor plane of a horizontal axis turbine.

Chougule et al. [2012] shown that under neutral, horizontally homogeneous ABL, $\varphi_v > \varphi_u > \varphi_w$ and the RDT and LES modeled phases are consistent with the observed phases under neutral condition. There are two basic assumptions considered in the study of Chougule et al. [2012], one neutral stratification and second horizontally homogeneous flow. In order to confirm in more detail about the phase shift due to the shearing effect and the phase behavior, we analyze diabatic data from Høvsøre with the essentially inhomogeneous flow.

1.1.2 Definitions

The phases are calculated from complex cross-spectra. The cross-spectrum between velocity components $u_i(t)$ $(i = 1,2,3)$ and $u_j(t)$ $(j = 1,2,3)$ at heights z_1 and z_2, respectively, is defined as

$$\chi_{ij}(f,\Delta z) = \langle \hat{u}_i(f,z_1)\hat{u}_j^*(f,z_2) \rangle, \tag{1.1}$$

where f is frequency, $\Delta z = z_2 - z_1$, $\langle\ \rangle$ denotes ensemble averaging, $*$ denotes complex conjugate and $\hat{u}_i(f,z_1)$ is the complex-valued Fourier transform of the i^{th} velocity component $u_i(t)$ at height z_1. The phase between the two velocity components is then

$$\varphi_{ij}(f,\Delta z) = \arg(\chi_{ij}(f,\Delta z)). \tag{1.2}$$

The coherences, sometimes known as "squared coherences", are calculated from the cross-spectra and the single-point power-spectra via

$$\mathrm{coh}_{ij}(f,\Delta z) = \frac{|\chi_{ij}(f,\Delta z)|^2}{F_i(f,z_1)F_j(f,z_2)}, \tag{1.3}$$

where $F_i(f,z) = \langle \hat{u}_i(f)\hat{u}_i^*(f) \rangle$ is the single-point power-spectrum of the i^{th} velocity component $u_i(t)$ at height z.

If we assume that Taylor's hypothesis of "frozen turbulence" is valid, then the measured time series can be related to spatial fluctuations. So for the stream-wise direction, single-point measurements can be related through $k_1 = 2\pi f/U$, where U is the stream-wise mean wind speed.

1.2 Høvsøre

The measurements are taken from the 116.5 m tall mast at the Høvsøre test site on the west coast of Denmark. Sonic anemometers, sampling at 20 Hz and measuring in three dimensions, are installed on the mast at heights of 10, 20, 40, 60, 80 and 100 m. The land to the east of the mast can be considered as flat, homogeneous terrain. On the west side of the mast, land extends 1500 m to the North Sea coast, including a dune which can affect the flow. Five wind turbines are situated to the north of the mast. More details about the location and instrumentation can be found in Refs. Sathe et al., 2012].

Winds are selected from directions between 240° and 300° from where the flow is

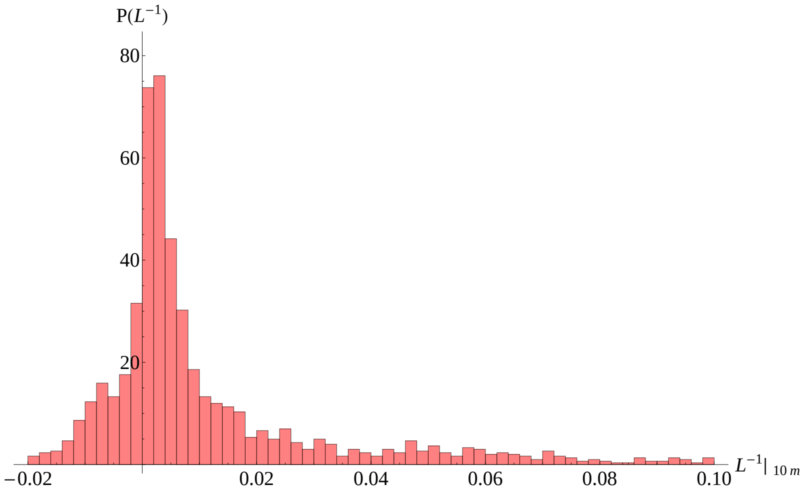

Figure 1.2: Histogram of atmospheric stabilities based on Obukhov lengths for wind directions between 240° and 300°, for all wind speed bins at the Høvsøre test site in the west coast of Denmark. ABL is classified into 7 stabilities (c. f. Table 1.1).

essentially inhomogeneous and the data limited to when the 80 m mean wind speeds fall between 8 and 9 $\mathrm{m\,s^{-1}}$. The calculations are done for diabatic conditions, where atmospheric stability is classified based on the range of Obukhov lengths L_0 as given in Table 1.1 following Gryning et al. [2007]. The height interval chosen in the phase analysis spans 40 – 100 m. Analysis is done using seven years of data from 2004 to 2010.

Table 1.1: Classification of ABL into seven atmospheric stabilities following Gryning et al. [2007].

Obukhov Length (m)	Atmospheric Stability
$-100 \leq L_o \leq -50$	Very Unstable (VU)
$-200 \leq L_o \leq -100$	Unstable (U)
$-500 \leq L_o \leq -200$	Near Unstable (NU)
$\lvert L_o \rvert \geq 500$	Neutral (N)
$200 \leq L_o \leq 500$	Near Stable (NS)
$50 \leq L_o \leq 200$	Stable (S)
$10 \leq L_o \leq 50$	Very Stable (VS)

The Figure 1.2 show the probability of occurrences of different atmospheric stabilities from very unstable (negative L_o) to very stable (positive L_o) case. The Obukhov length L_o is defined as

$$L_o = \frac{-{u_*}^3}{\kappa(g/T)\overline{w'T'}_0}, \tag{1.4}$$

where u_* is the surface friction velocity which is constant within the surface layer and decrease with the height above the surface layer, κ is the von Kármán constant (typically the value 0.4 is used), g is the acceleration due to gravity, T is the reference temperature (if moisture is included then T is the virtual temperature and due to conserved scalar, T becomes virtual potential temperature), $\overline{w'T'}_0$ is the virtual potential temperature flux at the surface.

1.3 Spectral tensor model

The Mann spectral velocity tensor model incorporates RDT with an assumption of a mean uniform shear, plus a wavenumber-dependent eddy lifetime, to estimate the structure of turbulence over uniform flat terrain, which has been extended to cover gently varying orography (Mann [2000]). The model calculates the evolution of turbulence in Fourier modes from an initial isotropic state, the energy spectrum of which is given by the von Kármán form von Kármán [1948].

The Mann model contains three adjustable parameters:

- A length scale L describing the size of energy-containing eddies
- A non-dimensional anisotropy parameter Γ used in the parameterization of eddy lifetime
- A measure of the energy dissipation $\alpha\varepsilon^{2/3}$, where the Kolmogorov constant $\alpha = 1.7$ and ε is the rate of viscous dissipation of specific turbulent kinetic energy.

The analytical form of the spectral velocity tensor in Mann [1994a] is a function of these three parameters and can be expressed as $\Phi_{ij}(\boldsymbol{k}, L, \Gamma, \alpha\varepsilon^{2/3})$, where $\boldsymbol{k} = (k_1, k_2, k_3)$ is the three-dimensional wavenumber vector. The modeled cross-spectra which also become functions of the three parameters, are given as

$$\chi_{ij}(k_1, L, \Gamma, \alpha\varepsilon^{2/3}, \Delta y, \Delta z) = \int \Phi_{ij}(\boldsymbol{k}, L, \Gamma, \alpha\varepsilon^{2/3}) \exp(\mathrm{i}(k_2\Delta y + k_3\Delta z))\mathrm{d}\boldsymbol{k}_\perp, \tag{1.5}$$

where $\int \mathrm{d}\boldsymbol{k}_\perp \equiv \int_{-\infty}^{\infty}\int_{-\infty}^{\infty} \mathrm{d}k_2 \mathrm{d}k_3$ and Δy is the transverse separation distance. The three parameters are determined by fitting model single-point power-spectra, which from Equation 1.5, are given by $F_i(k_1, L, \Gamma, \alpha\varepsilon^{2/3}) = \chi_{ii}(k_1, L, \Gamma, \alpha\varepsilon^{2/3}, 0, 0)$ (no summation), to the measured single-point power-spectra through chi-squared fitting as given in Ref. Mann [1994a].

Figure 1.3 gives an example of a model fit of power-spectra to the Høvsøre data at 40 m height for unstable, neutral and stable conditions illustrating extraction of L, Γ and $\alpha\varepsilon^{2/3}$. However, the Mann spectral tensor model assumes neutral stratification, and the three parameters for non-neutral conditions can be obtained by forcing the model to fit with measured spectra through chi-squared fits. The three parameters subsequently used as an input to calculate numerically the cross-spectrum between any two velocity components through Equation 1.5. Thus for vertical separations ($\Delta y = 0$), the model cross-spectra and phases are expressed as $\chi_{ij}(k_1, L, \Gamma, \alpha\varepsilon^{2/3}, \Delta z)$ and $\varphi_{ij}(k_1, L, \Gamma, \Delta z)$, respectively. The model phases are unaffected by ε.

The distortion of the wave vector due to shear $\mathrm{d}U/\mathrm{d}z$ is given by $\boldsymbol{k}(t) = (k_1, k_2, k_{30} - k_1(\mathrm{d}U/\mathrm{d}z)t)$, with the initial wave vector $\boldsymbol{k}_0 = (k_1, k_2, k_{30})$. The model assumes a uniform shear so $\mathrm{d}U/\mathrm{d}z$ is constant with height which is an approximation, but we do not expect that a non-zero $\mathrm{d}^2U/\mathrm{d}z^2$ would significantly alter the results. In addition to the uniform shear, the vertically inhomogeneous effect of blocking due to the surface (e.g. ground) was included in Mann [1994a]; however, it does not produce significantly different results. Nevertheless, as discussed above, χ_{ij}, F_i and φ_{ij} are functions of L, which itself depends on the distance z from the ground. In this way the model treats vertical inhomogeneity in application.

In the next section, the results from the observations and the model are provided, followed by discussion in Section 5.

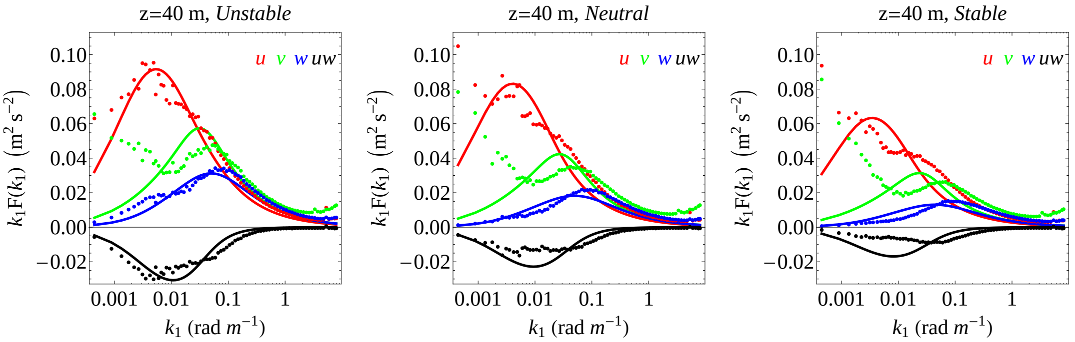

Figure 1.3: Example of the model spectral fits (smooth lines) to the Høvsøre data (points) at $z = 40$ m, for wind directions between 240° and 300° and wind speed bin 8-9 ms^{-1}. Number of thirty-minute time series: Unstable; 165, Neutral; 176 and Stable; 538.

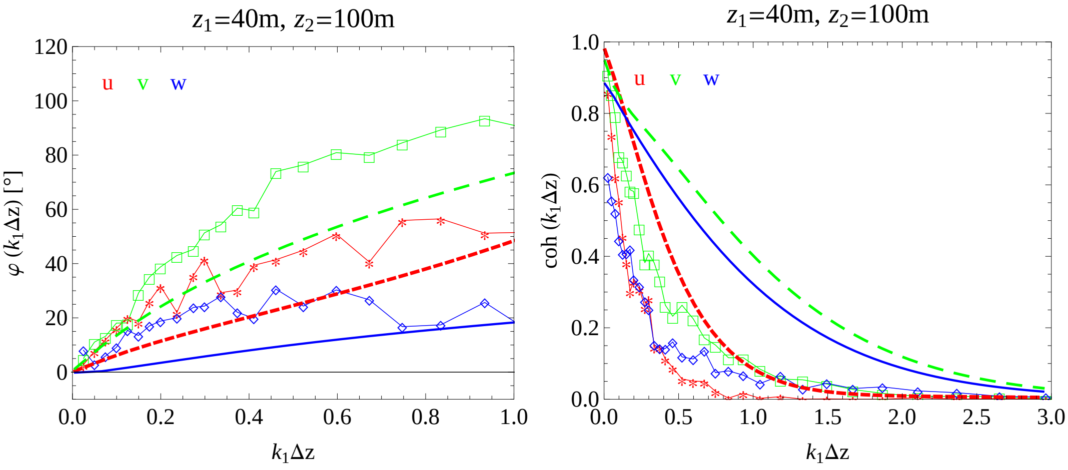

Figure 1.4: The cross-spectral phases (a) and the coherences (b) between 40 and 100 m at Høvsøre for a neutral ABL fitted with the spectral tensor model. Measurements: φ_u; $-\ast-$, φ_v; $-\Box-$, φ_w; $-\diamond-$. Model: φ_u; **- - -**, φ_v; − − −, φ_w; ——. Similar notations are followed for the coherences.

1.4 Results

The phases and coherences from the Høvsøre observations are shown in Figure 1.4, along with the predictions from the Mann model for neutral ABL. As described in Section 3.1, the three adjustable parameters in the model are determined by fitting the one-dimensional power-spectra of the model to that from the data at heights 40 and 100 m (see Figure 1.3). The average of the parameters at the two heights is used to calculate the model cross-spectra.

The slopes of the phase curves predicted by the model are different than those calculated from the measurements. However, the model is able to predict the order in phasing, $\varphi_v > \varphi_u > \varphi_w$, for $k_1\Delta z \leq 1$. The model overestimates the *u*-, *v*- and *w*-coherence for $k_1\Delta z \leq 1$. So at a given length scale, the fluctuations at two corresponding heights in the modeled coherent eddies are more correlated than those from the observation. It is also observed that the modeled phases are smaller than the phase angles from the measurements. When phases are examined with different atmospheric stabilities, we observe same order in phase shift for three velocity components as depicted in Figure 1.5.

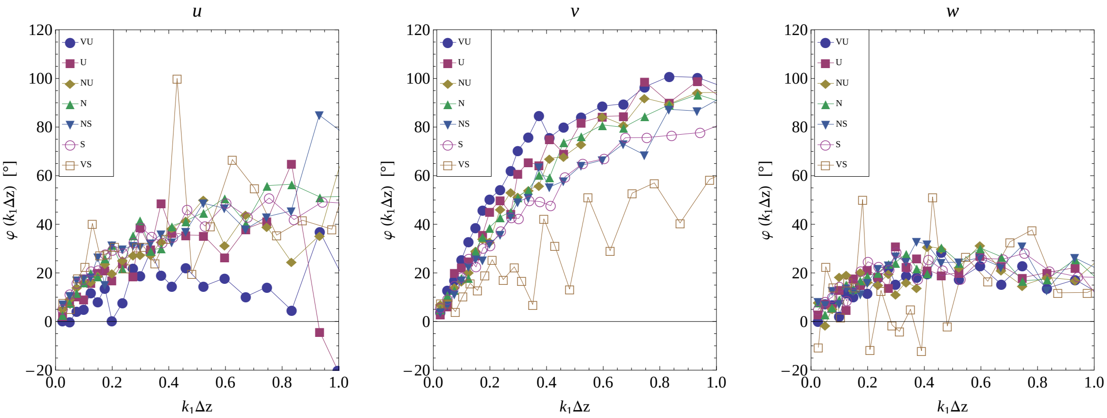

Figure 1.5: The phases between 40 and 100 m at Høvsøre for different atmospheric stabilities for wind directions between 240° and 300°.

1.5 Discussion

In this section we describe some more details about the behaviour of the phases under diabatic conditions. The phase angles for neutral ABL are studied and compared with the RDT and LES model in Chougule et al. [2012], where the winds at Høvsøre are selected from east (between 60° and 120°) with essentially homogeneous flow over flat terrain. Here we represent the results corresponding to winds from west (from North sea, inhomogeneous terrain). There is no significant difference in the phase angles as compared with Chougule et al. [2012]. However, it is observed that the L and Γ parameters are significantly greater for the winds from west than those from east for the same height span as given in Table 1.2.

Table 1.2: Average of L and Γ parameters at Høvsøre for the winds from east (Chougule et al. [2012]) and west, for the given height span 40-100 m.

Wind direction	$\overline{L}$ (m)	$\overline{\Gamma}$
60° and 120°	40	3.3
240° and 300°	92	4.0

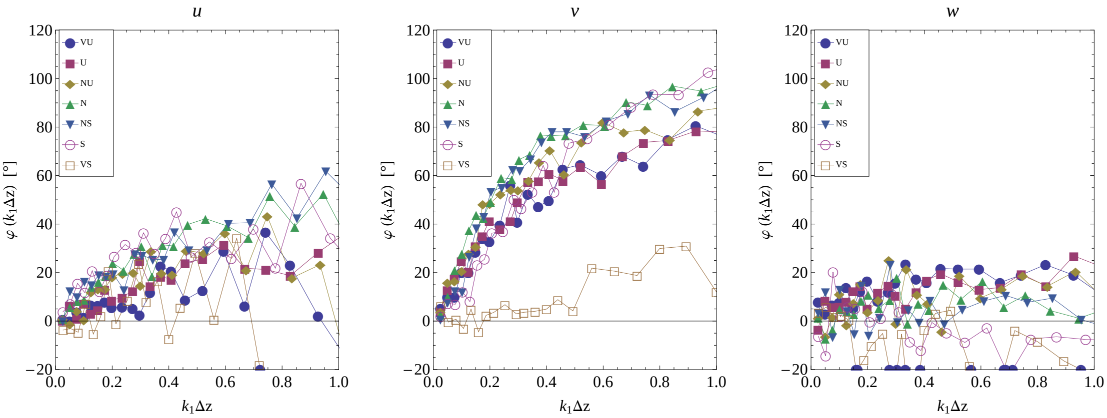

Figure 1.6: The phases between 40 and 100 m at Høvsøre for different atmospheric stabilities for wind directions between 60° and 120°.

It should be noted that the model spectra fits in Figure 1.3 are very poor because the upstream surface conditions are inhomogeneous, and that the fits from the eastern sector presented in Chougule et al. [2012] are much better. The predicted coherences in Figure 1.4 (left plot) are correspondingly poor (again much worse than those in Chougule et al. [2012]), but the phases are still reasonable.

As discussed in Section 3.1, the phases from the spectral tensor model are functions of L and Γ parameters. The model phases increase with the decrease in L parameter and increases with the increment in Γ. At a given mean wind speed (say 8 m s^{-1}), the turbulence length scale decrease from very unstable towards very stable (Ref. Sathe et al. [2012]) and hence the model phases should increase. However, as shown in Sathe et al. [2012] there is no systematic effect of atmospheric stability on Γ at a given mean wind speed. Following this discussion, it can be concluded that there is no systematic effect of atmospheric stability on the phase angles. This can also be seen from Figure 1.5. The stability based phase analysis is new relative to Chougule et al. [2012]. However, the study in Sathe et al. [2012] is also restricted to winds at Høvsøre from east and the above discussion should make more sense when we observe the diabatic phase angles corresponding to winds from east as depicted in Figure 1.6. For the winds from west reader may able to find systematic decrease in v-phase from very unstable towards vary stable by observing Figure 1.5.

More intuitive explanation behind the behavior of the phase angles due to shear based on rapid distortion theory may be found in Chougule et al. [2012].

1.6 Conclusions

The phase angles of all the three velocity components are analysed from Høvsøre data for inhomogeneous terrain under diabatic conditions. These phases behave similarly to those under neutral ABL with no significant changes. The diabatic phase angles from inhomogeneous flow are insignificantly different than those for homogeneous flow. There is no systematic effect of atmospheric stability on the phase angles. Phases of the cross-spectra of all three velocity components show systematic behaviour: $\varphi_v > \varphi_u > \varphi_w$ for $k_1 \Delta z \leq 1$. RDT model is able to predict the observed neutral, inhomogeneous phase ordering.

Acknowledgements

This study is a part of the Ph.D. project funded by Siemens Wind Power A/S and WindScanner.dk which is funded by the Danish Agency for Science. We are also obliged to the COMWIND project funded by Danish Council of Strategic Research (DSF- contract: 09-067216).

Chapter 2

Spectral tensor parameters for wind turbine load modeling from forested and agricultural landscapes

---

2.1 Introduction

An adequate description of the structure of atmospheric turbulence is important for the calculation of dynamic loads on wind turbines. The classical concepts used for describing such structure include the velocity spectra, co-spectra, as well as the cross-spectral properties coherence and phase (Kaimal and Finnigan [1994]; Kristensen and Kirkegaard [1986]; Townsend [1976]). Spectral analysis is useful for analysis of the length scales inherent in turbulent motion (Tennekes and Lumley [1972]). In addition to the length scale estimations, coherences are also important to wind engineers (Davenport). Coherences are usually described as a function of separation perpendicular to the mean velocity as in Tong and Wyngaard [1996].

Spectral tensor models are often used to model the spectra and cross-spectra e.g., Kristensen et al. [1989], and such models can be used for the estimation of dynamic loads on turbines through simulation of the wind field toward the rotor. Models developed by Kaimal et al. [1972], Veers [1988] (Sandia method), and Mann [1994b] are commonly used in wind energy industry. The three-dimensional spectral tensor model of Mann (M94) differs from the other models mentioned above in many respects. It incorporates rapid distortion theory (RDT) (Pope [2000]; Townsend [1976]) with an assumption of uniform mean shear and consideration of eddy life time, while the model by Kristensen et al. [1989] is a kinematic model, and the models by Kaimal et al. [1972] and Veers [1988] are more empirical models incorporating many model parameters. The stationary M94 model is applicable for homogeneous neutral surface-layer turbulence. RDT has previously been used in non-stationary spectral tensor modeling of homogeneous uniform sheared (Maxey [1982]), unsheared stably stratified (Hanazaki and Hunt [1996]), and sheared stably stratified (Hanazaki and Hunt [2004]) turbulent flows.

IEC [2005] recommends the use of M94 for the estimation of loads on wind turbines through simulation of rotor inflow (Mann [1998]). The spectral shapes and coherences that the model predicts have previously been compared with the data measured over sea, over a flat rural terrain, and even in boundary-layer wind-tunnels as described in Mann [1994a]. In these studies, coherences of the along-wind, cross-wind, and vertical velocity components (u, v, and w, respectively) have been found to decrease with increasing cross-wind separation distance, which matched with both observation and theoretical predictions, but coherences of all the velocity components for given vertical separations have never been estimated. The boundary-layer wind-tunnel testing described in Mann [1994a] showed that the wind tunnel turbulence was slightly more isotropic than the natural turbulent wind. None of the M94 tests were conducted beyond 70 m above the terrain. Later, the model one-point spectra were fitted to observations of wind speed made by sonic anemometer at higher heights even for non-neutral conditions (Peña et al. [2010a]), although the model was not extended to account for temperature effects. The study conducted by Peña et al. [2010a,b] demonstrated a close connection between the mixing length derived from the wind speed profile and the turbulence length scale from the M94 model. The spectral tensor resulting from the fitting of the measured one-point spectra was used to investigate how dynamic wind loads depend on atmospheric stability (Sathe et al. [2012]). However, the cross-spectral properties were never investigated in the studies described in Peña et al. [2010a,b]; Sathe et al. [2012]. The exception from only looking at one-point spectra was Chougule et al. [2012], who compared the predicted two-point cross-spectral phases with measurements. Chougule et al. [2012] demonstrated that the v-phase φ_v was significantly greater than the u-phase φ_u, which in turn was greater than the w-phase φ_w for $k_1 \Delta z \leq 1$, where k_1 is the stream-wise wave number and Δz is the vertical separation; the M94 model predicted this phase behavior correctly. The Sandia method of Veers [1988], on the other hand, assumes an average of zero phase between any two points such that the imaginary parts of the cross-spectra are zero. However, the actual consequence of the differences in the cross-spectral phases on the wind loads of horizontal axis wind turbines has never been studied.

Generally, wind turbines are placed in open landscapes with low aerodynamic roughness; hence, wind engineering model tools have been developed keeping in mind that they have to perform well in such conditions. However, during the last decade, the siting of wind turbines in forested areas has become increasingly common. One of the drawbacks associated with forested areas is the increased load on the rotor caused by the high turbulence levels of the atmospheric flow. The model has never been compared with turbulence spectra measured over a forest, let alone the comparison with two-point statistics such as coherences or cross-spectral phases. It is therefore highly relevant to extend the validation to data taken in forested areas.

In this study[1], we investigated the performance of the M94 model concerning the prediction of velocity spectra measured over a forest, compared the parameters describing the model spectra with those from a low-roughness agricultural landscape, and tested the performance of the model in coherence predictions for both the agricultural and forested sites. This study differs from the previous studies mainly in the following respects:

1. Validation of M94 in a forested area
2. Evaluation of coherences of all three velocity components for vertical separation
3. Quantification of the model performance in the prediction of coherences

Our approach to the study is described in Section 2.2. For the analysis, we used data from two different sites, the Ryningsnäs site in Sweden (forested landscapes) and the Høvsøre test site in Denmark (agricultural landscapes), as described in Section 2.2.1. We selected the data based on the selection criteria described in Section 2.2.2, followed by the spectral tensor modeling described in Section 2.2.3. Analysis of both observed and modeling results are provided in Section 2.3, with discussions in more detail in

---

[1] This manuscript is submitted to the *Wind Energy* with the same title and co-authoring with J. Mann, A. Segalini and E. Dellwik.

Section 2.4. We conclude our study in Section 2.5 with some final considerations and guidelines.

2.2 Method

We estimated the velocity spectra and co-spectrum of u and w from the measured time series as

$$F_{ij}(f,z) \equiv \langle \hat{u}_i(f)\hat{u}_j^*(f)\rangle, \tag{2.1}$$

where $i, j = 1, 2, 3$; $(u_1, u_2, u_3) = (u, v, w)$; f is the frequency; $\langle\ \rangle$ denotes ensemble average operator; the superscript $*$ denotes complex conjugate, and $\hat{u}_i(f)$ is the complex-valued Fourier transform of the ith velocity component at height z.

We selected the data according to the classification of atmospheric stability in terms of the Obukhov length L_o following Gryning et al. [2007], where L_o is defined as (Kaimal and Finnigan [1994])

$$L_o = \frac{-{u_*}^3}{\kappa(g/T)\overline{w'T'}_0}, \tag{2.2}$$

where u_* is the surface friction velocity, $\kappa = 0.4$ is the von Kármán constant, g is the acceleration due to gravity, T is the mean surface-layer temperature and $\overline{w'T'}_0$ is the vertical heat flux at the surface. The measured spectra and co-spectra given in Equation 2.1 change with atmospheric stability (Kaimal et al. [1972]), i.e., $F_{ij}(f,z)$ is a function of L_o.

We performed χ^2-fits (described in Mann [1994b]) of the M94 model to the measured power-spectra in Equation 2.1 to obtain the three parameters (described in Section 2.3), that were used as inputs to estimate the model cross-spectra. Model coherences and cross-spectral phases were compared with those from the measurements. The cross-spectra, coherences, and cross-spectral phases were calculated from the measurements using general definitions, which can be found in Chougule et al. [2012].

2.2.1 Experimental data

Experimental data were obtained from the measurements taken at two different sites: the forested landscapes in Ryningsnäs (where data were taken from a mast above the forest canopy), and a sector with flat agricultural terrain at the Høvsøre test site in Denmark. Wind speed measurements were taken with Metek sonic anemometers (USA-1, Basic, Metek Gmbh) with a sampling frequency of $f = 20$ Hz and measuring in three dimensions. Statistical analyses were based on 30 minute intervals.

2.2.1.1 Ryningsnäs

The 138 m tall tower at Ryningsnäs is located in a relatively flat, forested terrain in Southeastern Sweden at $57°16.57'$N, $15°59.19'$E. Data from the sector between 235° and 275° were selected. In this sector, the influence from a local clearing as well as two nearby turbines to the south and the north-east, respectively, is avoided. Further, the flow distortion from the mast on the measurements is minimal and the upstream terrain is forested for more than 100 km, such that the whole boundary layer should be adapted to the high surface roughness. The forest near the tower is 20-25 m tall and consists mainly of Norway spruce (*Pinus Sylvestris*). Generally, the forest cover is not homogeneous, but rather consists of patches of different tree heights intercepted with clearings, lakes and lower-roughness areas.

The sonic anemometers were installed at the heights of 40, 59, 80, 98, 120 and 138 m. The measurements were performed between November 2010 and February 2012. More information on the site and the measurements can be found in Bergström et al. [2013].

2.2.1.2 Høvsøre

The measurements were taken from the 116.5 m tall mast located at the coordinates $56°26'26''$N, $08°09'03''$E in the Høvsøre test site near the west coast of Denmark. Sonic anemometers were installed on the mast at heights of 10, 20, 40, 60, 80, and 100 m. The land to the east of the mast is flat, consisting mostly of agricultural landscapes. Five wind turbines were placed to the north of the mast. To avoid the wake effects of wind turbines, winds were selected from the region between 60° and 120°. Around 65° and at 8 km from the mast, there are lines of trees and a big forest that extends about 12 km in both north-south and east-west directions. A small village is situated at approximately 100° about 2.8 km from the mast, which could also have affected the flow downstream to west. On the west side of the mast, land extends 1500 m to the North Sea coast, including a dune. More details about the location and instrumentation can be found in Sathe et al., 2012]. The analysis was done using seven years of data from 2004 to 2010.

2.2.2 Data selection

Data from both the sites were selected based on a narrow wind speed interval measured at 80 m height as well as bins of L_o measured at 40 and 10 m on the masts at Ryningsnäs and Høvsøre sites, respectively. Due to limitations on the availability of data and in order to compare the results from two sites, we analyzed NNS, neutral (N), and NNU stability cases (cf. Table 2.1). Since the results for the other wind speeds were similar, the results for the wind speed bin 7-8 ms^{-1} only are provided.

Table 2.1: Classification of atmospheric stability according to the Obukhov length intervals (in m^{-1}).

Near-neutral stable (NNS)	$0.002 \leq L_o^{-1} \leq 0.005$
Neutral (N)	$\lvert L_o^{-1} \rvert \leq 0.002$
Near-neutral unstable (NNU)	$-0.005 \leq L_o^{-1} \leq -0.002$

Figure 2.1 shows the histogram of atmospheric stability in terms of L_o from the Ryningsnäs (left plot) and Høvsøre (right plot) sites, for the velocity bin 7-8 ms^{-1}. For this wind speed interval, hardly any occurrences of very stable or very unstable cases were observed at the Ryningsnäs site.

2.2.3 Spectral tensor model

The velocity-spectrum tensor $\Phi_{ij}(\boldsymbol{k})$ of M94 is valid in the neutral surface-layer with the assumption of uniform shear $\mathrm{d}U/\mathrm{d}z$, where $\boldsymbol{k}(t) = (k_1, k_2, k_{30} - k_1(\mathrm{d}U/\mathrm{d}z)t)$ is a three dimensional wave vector, and t is time. The model calculates the evolution of Fourier modes under the influence of the mean shear from an initial isotropic state. In

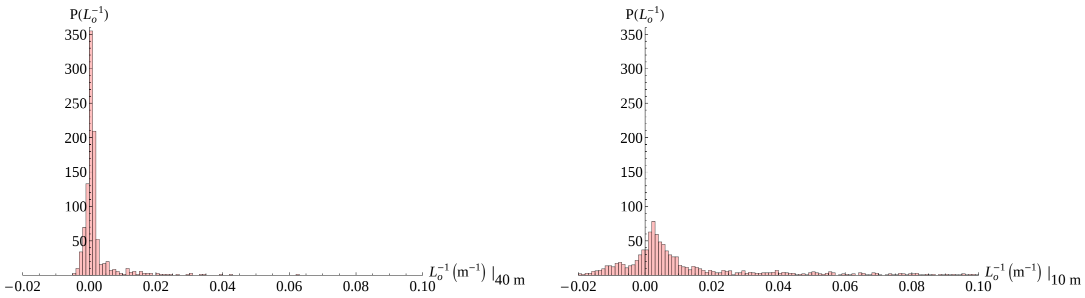

Figure 2.1: Histogram of atmospheric stabilities based on the Obukhov lengths for wind directions between 235° and 275° at the Ryningsnäs test site in Sweden (left plot) and for wind directions between 60° and 120° at the Høvsøre test site in the west coast of Denmark (right plot). The wind speed bin selected was 7-8 m s^{-1} measured at $z = 80$ m.

isotropic turbulence, the velocity-spectrum tensor is

$$\Phi_{ij}(\boldsymbol{k}_0) = \frac{E(k)}{4\pi k^2}\left(\delta_{ij} - \frac{k_i k_j}{k^2}\right), \tag{2.3}$$

where $\boldsymbol{k}_0 = \boldsymbol{k}(0)$ and k is the length of the vector $\boldsymbol{k}$. The energy spectrum $E(k)$ given by von Kármán [1948] as

$$E(k) = \alpha\varepsilon^{2/3}L^{5/3}\frac{(kL)^4}{(1+(kL)^2)^{17/6}}, \tag{2.4}$$

where $\alpha \approx 1.7$ is the Kolmogorov constant, ε is the rate of viscous dissipation of specific turbulent kinetic energy (TKE), and L is a turbulence length scale.

In order to make the model stationary, the time dependency in the model was removed by incorporating the general concept of an eddy life time, $\tau(k)$, and the parameterization of $\tau(k)$ in M94 was

$$\tau(k) = \Gamma\left(\frac{\mathrm{d}U}{\mathrm{d}z}\right)^{-1}(kL)^{-2/3}\left[{}_2F_1\left(\frac{1}{3},\frac{17}{6};\frac{4}{3};-(kL)^{-2}\right)\right]^{-1/2}, \tag{2.5}$$

where Γ is a parameter to be determined and ${}_2F_1$ is the Gaussian or ordinary hypergeometric function. The analytical forms of $\Phi_{ij}(\boldsymbol{k})$ in M94 can be expressed as

$$\Phi_{ij}(\boldsymbol{k}) \equiv \Phi_{ij}(\boldsymbol{k}, \alpha\varepsilon^{2/3}, L, \Gamma). \tag{2.6}$$

Equation 2.6 can also be given as

$$\Phi_{ij}(\boldsymbol{k}, \alpha\varepsilon^{2/3}, L, \Gamma) = \alpha\varepsilon^{2/3} L^{11/3} \Phi_{ij}(\boldsymbol{k}L, 1, 1, \Gamma), \tag{2.7}$$

and $\Phi_{ij}(\boldsymbol{k}_0) = \alpha\varepsilon^{2/3} L^{11/3} \Phi_{ij}(\boldsymbol{k}L, 1, 1, 0)$. So the model contain three adjustable parameters that were determined from the single-point measurements. These three parameters were as follows:

- $\alpha\varepsilon^{2/3}$ from Equation 2.4
- L, which represents the size of the energy containing eddies
- Γ, from Equation 2.5, which is a measure of turbulence anisotropy

Using Equation 2.6, the cross-spectrum between any two velocity components can be given as

$$\chi_{ij}(k_1, \alpha\varepsilon^{2/3}, L, \Gamma, \Delta y, \Delta z) = \int \Phi_{ij}(\boldsymbol{k}, \alpha\varepsilon^{2/3}, L, \Gamma) \exp\left[\mathrm{i}(k_2 \Delta y + k_3 \Delta z)\right] \mathrm{d}\boldsymbol{k}_\perp, \tag{2.8}$$

where $\int \mathrm{d}\boldsymbol{k}_\perp = \int_{-\infty}^{\infty} \int_{-\infty}^{\infty} \mathrm{d}k_2 \mathrm{d}k_3$. Δy and Δz are transverse and vertical separations, respectively. Using Equation 2.8, the single-point power-spectrum of the ith velocity component, can be given as, $F_i(k_1, \alpha\varepsilon^{2/3}, L, \Gamma) = \chi_{ii}(k_1, \alpha\varepsilon^{2/3}, L, \Gamma, 0, 0)$ (with no index summation), where $\Delta y = \Delta z = 0$.

The three parameters at any height z were calculated by fitting model (co-) spectra $\chi_{ij}(k_1, \alpha\varepsilon^{2/3}, L, \Gamma, 0, 0)$ with measured power-spectra (including co-spectrum of u ($i = 1$) and w ($j = 3$)) from Equation 2.1 and using Taylor's hypothesis: $k_1 = 2\pi f / U$, where U is the mean wind speed at z. For vertical separations Δz, coherences and cross-spectral phases were defined, respectively, as

$$\begin{aligned} \mathrm{coh}_{ij}(\overline{k_1}, \overline{L}, \overline{\Gamma}, \Delta z) &= \frac{|\chi_{ij}(\overline{k_1}, \alpha\varepsilon^{2/3}, \overline{L}, \overline{\Gamma}, \Delta z))|^2}{F_i(\overline{k_1}, \alpha\varepsilon^{2/3}, \overline{L}, \overline{\Gamma}) F_j(\overline{k_1}, \alpha\varepsilon^{2/3}, \overline{L}, \overline{\Gamma})}, && (2.9) \\ \varphi_{ij}(\overline{k_1}, \overline{L}, \overline{\Gamma}, \Delta z) &= \arg(\chi_{ij}(\overline{k_1}, \alpha\varepsilon^{2/3}, \overline{L}, \overline{\Gamma}, \Delta z)), && (2.10) \end{aligned}$$

where $\overline{L}$ and $\overline{\Gamma}$ are the average of L and Γ parameters at two heights z_1 and z_2 (so that $\Delta z = z_2 - z_1$), and $\overline{k_1} = 4\pi f/(U_1 + U_2)$. The model coherences and cross-spectral phases are independent of $\alpha\varepsilon^{2/3}$, which can be seen from Equation 2.7 and the definitions above.

The M94 model assumes horizontal homogeneity, zero Coriolis force, and a uniform shear $\mathrm{d}U/\mathrm{d}z$, that is constant with height. We do not expect that the curvature of the ABL velocity profile (i.e. non-zero $\mathrm{d}^2U/\mathrm{d}z^2$) would alter the results significantly; however, because the three parameters were determined from the single-point measurements, one should expect these parameters to vary with height.

Let us consider the performance of the three parameters with respect to the variances and co-variances. A change in $\alpha\varepsilon^{2/3}$ causes a shift of the spectra in the ordinate direction; an increase in $\alpha\varepsilon^{2/3}$ results in shifting of u, v and w spectra up and uw co-spectrum down and vice-versa. An increase in L results in shifting of the spectra both to the left along the abscissa and upward along the ordinate and vice-versa. The model assumes initial isotropic turbulence where $\Gamma = 0$, leading to $\sigma_u^2 = \sigma_v^2 = \sigma_w^2$ and $\langle uw \rangle = 0$. For $\Gamma > 0$ the turbulence is anisotropic, i.e., $\sigma_u^2 > \sigma_v^2 > \sigma_w^2$ and $\langle uw \rangle < 0$, so Γ describes the anisotropic nature of turbulence. The various length scales of the velocity components can be calculated as functions of L and Γ. Higher values of Γ imply larger scale separation between the three velocity components and the length scale of u is greater than that of v which again is greater than that of w.

2.3 Analysis and Results

We showed the velocity spectra and uw co-spectrum from Ryningsnäs and Høvsøre met masts measured at 80 m height for NNS, N, and NNU stratifications along with the model fits. The cross-spectra between 80-100 m height were then analyzed using the average of the three parameters determined at these two heights as an input.

2.3.1 Spectra

The measured velocity spectra along with the model spectral fits for NNS, N and NNU are shown in Figure 2.2, for Ryningsnäs (left plots) and Høvsøre (right plots) sites. The power spectral densities at the Ryningsnäs site were observed to be higher than that of

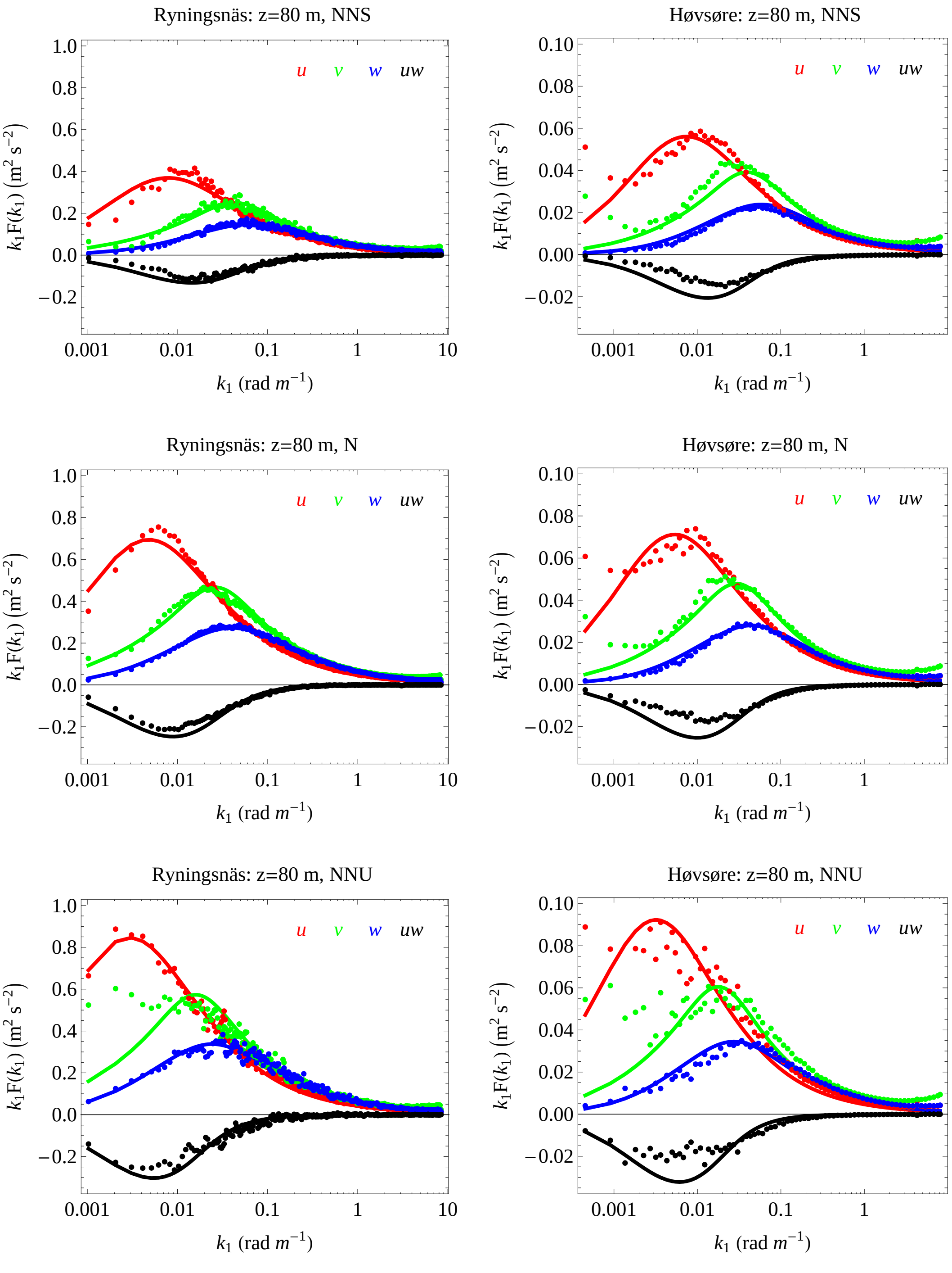

Figure 2.2: M94 spectral fits (solid lines) to the Ryningsnäs and Høvsøre measurements (dots) in NNS, N and NNU ABLs at $z = 80$ m, for the wind speed bin 7-8 m s^{-1}. The number of 30-minute time series n and the model parameters at $z = 80$ m are given in Table 2.3.

the Høvsøre site, due to the higher roughness. The mesoscale motions, identified from the excess power spectral density for $k_1 < 0.002$ m^{-1}, seemed to appear at the Høvsøre site and not at the Ryningsnäs site, which might be because the mesoscale motions at Ryningsnäs were obscured by generally higher turbulence levels at that site. The turbulence level on both sites can quantitatively be seen in terms of variances and co-variances of the velocity components, as given in Table 2.2. Table 2.2 also gives an indication of model performance in terms of Δ, which is the model estimation error of the variance relative to the measured variance. A comparison of the Δ values at the Ryningsnäs and Høvsøre sites revealed that the model performs relatively better in Ryningsnäs than Høvsøre, particularly for neutral stability. The Δ value of the *uw* co-variance was quite significant for Høvsøre NNS and N cases, and it decreased at both the sites going from NNS to NNU. The values of TKE in Ryningsnäs were ~ 5, ~ 8.5, and ~ 8 times those in Høvsøre, for NNS, N, and NNU, respectively. Comparing the model parameters determined at the given sonic heights from two sites (Figure 2.3), we found that the three model parameters from Ryningsnäs behaved similarly to those

Table 2.2: Performance of the model in variance and co-variance predictions in terms of Δ at $z = 80$ m, where Δ is the relative model over/under estimation of the variance. σ is the standard deviation. The model overestimation is denoted by '+' and underestimation by '−'.

		Ryningsnäs			Høvsøre		
Stability	σ^2 (m^{2}s^{-2})	Meas.	Model	Δ%	Meas.	Model	Δ%
NNS	σ_u^2	2.92	3.04	+4.35	0.53	0.50	−5.7
	σ_v^2	1.98	1.96	−0.94	0.39	0.31	−20.5
	σ_w^2	1.25	1.26	+0.84	0.18	0.20	+11.1
	$-\langle uw \rangle$	0.67	0.86	+28.72	0.09	0.14	+55.5
N	σ_u^2	5.37	5.34	−0.68	0.66	0.61	−7.6
	σ_v^2	3.68	3.60	−2.11	0.46	0.38	−17.4
	σ_w^2	2.35	2.32	−1.26	0.23	0.24	+4.3
	$-\langle uw \rangle$	1.32	1.54	+17.15	0.12	0.17	+41.7
NNU	σ_u^2	6.11	5.91	−3.24	0.83	0.75	−9.6
	σ_v^2	5.27	4.31	−18.36	0.65	0.48	−26.2
	σ_w^2	2.95	2.83	−3.95	0.30	0.30	0.0
	$-\langle uw \rangle$	1.60	1.75	+9.66	0.17	0.21	+23.5

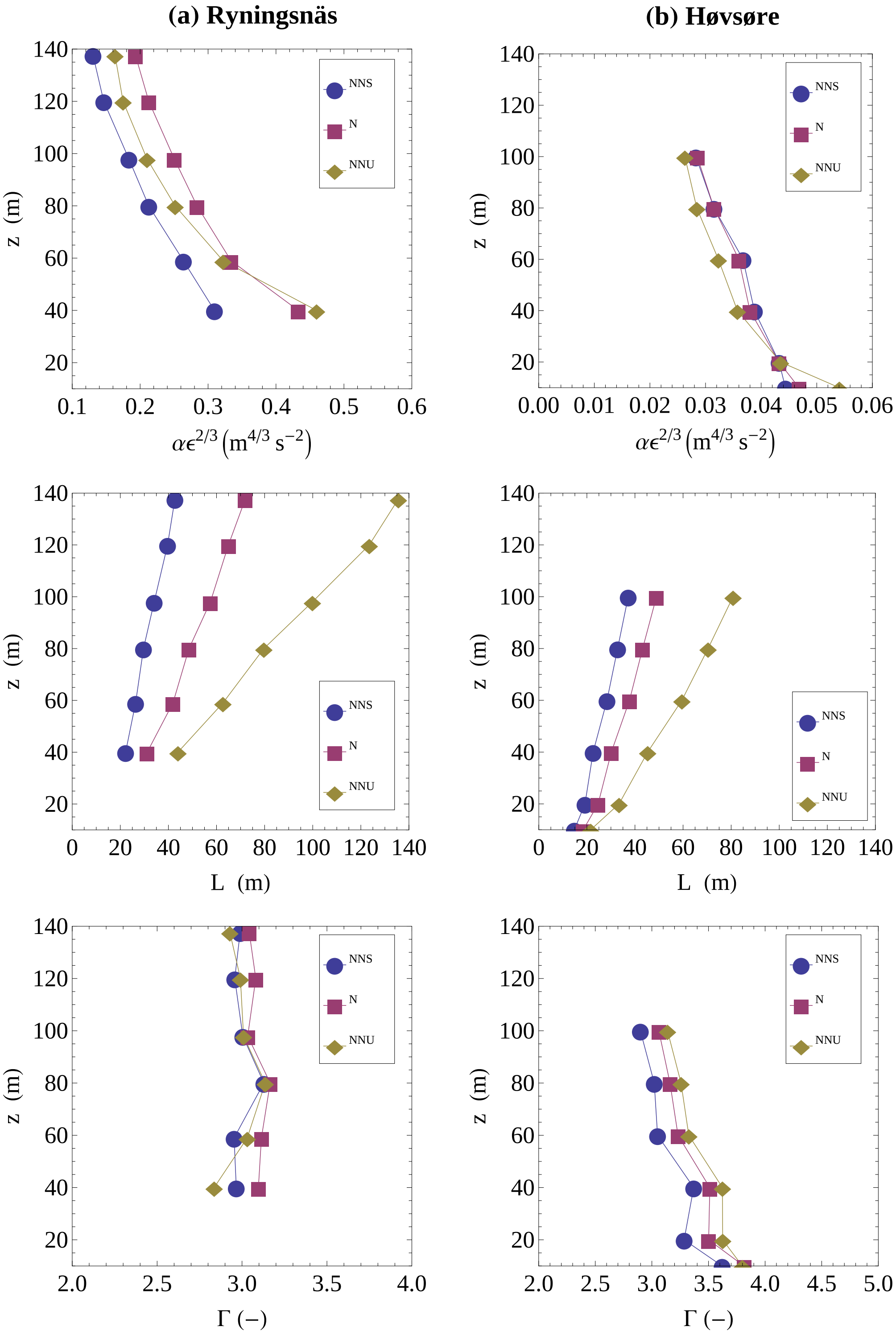

Figure 2.3: Comparison of the model parameters determined from the single-point measurements for (a) the forested landscapes in Ryningsnäs and (b) the agricultural landscapes in Høvsøre, for the wind speed bin 7-8 m s^{-1} measured at $z = 80$ m.

from a flat agricultural terrain. The three model parameters determined at 80 m from the two sites, along with the number of 30-minute time series n, are shown in Table 2.3. The value of $\alpha\varepsilon^{2/3}$ for Ryningsnäs was 8.75 times that for Høvsøre at $z = 80$ m for the neutral case. There was no significant difference in the L vertical profile beyond $z = 40$ m between the two sites. The length scales from the two sites were similar, with the notable difference that L for the NNU case at Ryningsnäs was 24% higher than that at Høvsøre at $z = 100$ m. The turbulence length scales L for all stabilities were found to increase with height, with L for NNU being the greatest. There was a very slight difference in the turbulence anisotropy at the two sites except at 40 m, where the Ryningsnäs turbulence was as much as $\sim 22\%$ more isotropic (for NNU). The turbulence anisotropy remained more or less constant with height at Ryningsnäs, whereas, the turbulence became slightly more isotropic with height at Høvsøre.

Table 2.3: Three spectral tensor parameters determined from χ^2-fits for NNS, N, and NNU stability cases at the Ryningsnäs and Høvsøre sites for the velocity bin 7-8 m s^{-1}. The measurements are taken from sonic anemometers located at $z = 80$ m.

			Model parameters		
	Stability	n	$\alpha\varepsilon^{2/3}$ (m$^{4/3}$ s^{-2})	L (m)	Γ
Ryningsnäs	NNS	60	0.21	29.6	3.13
	N	542	0.28	48.6	3.16
	NNU	33	0.25	79.7	3.14
Høvsøre	NNS	256	0.032	32.8	3.02
	N	226	0.032	43.2	3.16
	NNU	68	0.028	70.4	3.26

2.3.2 Cross-spectra

The model coherences and cross-spectral phases were calculated using Equations 2.9 and 2.10, respectively. The coherence comparisons are shown in Figure 2.4. The values of $\overline{L}$, $\overline{\Gamma}$ at Ryningsnäs were as follows -for NNS: 32 m, 3; N: 53 m, 3.1; and NNU: 90 m, 3.1; and those for Høvsøre were NNS: 35 m, 2.9; N: 46 m, 3.1; and NNU: 75 m, 3.2. Atmospheric stability was found to affect the coherence that increased from stable to unstable stratification. Thermal stability had the most noticeable effect on the

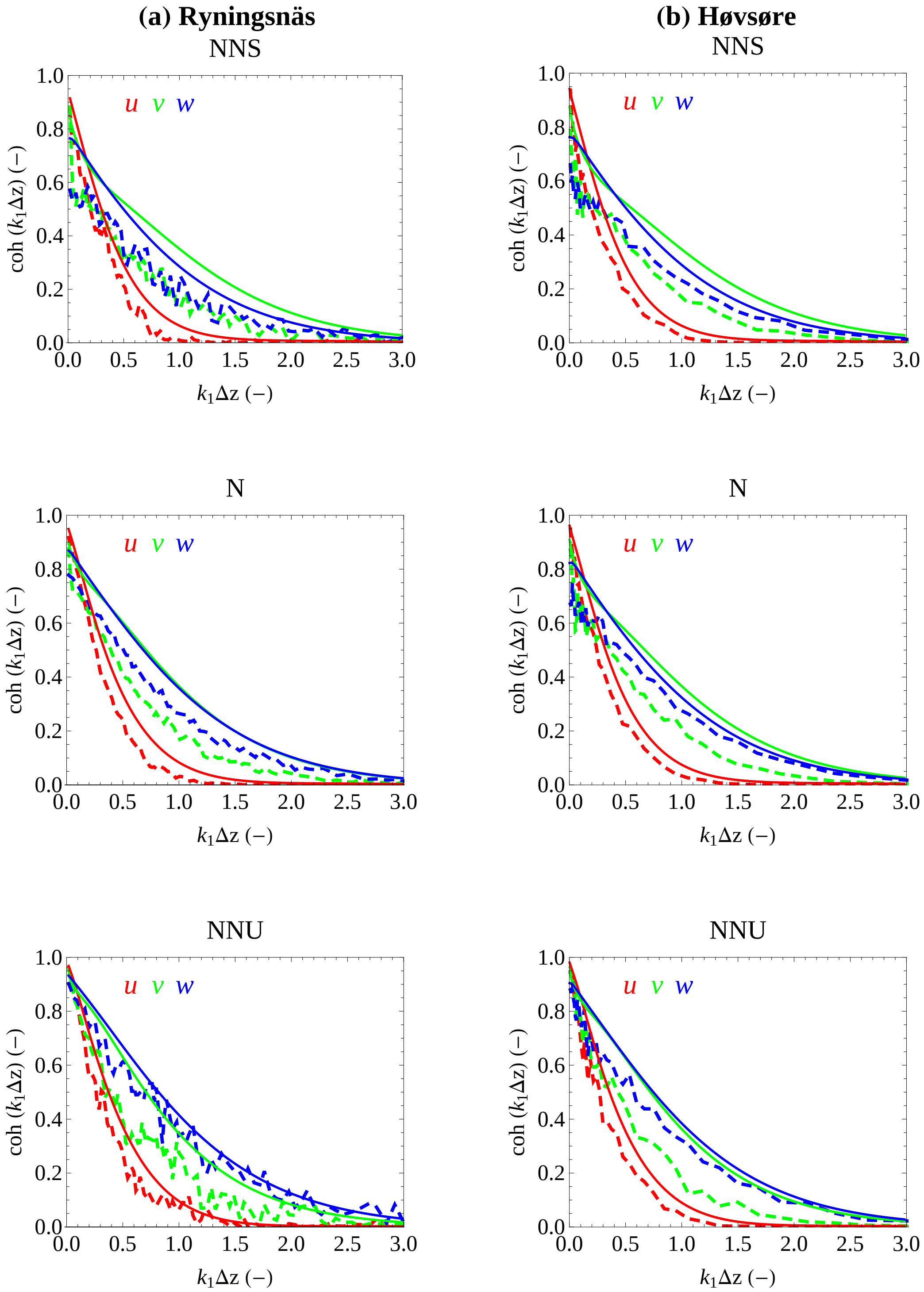

Figure 2.4: Comparison of the coherences from the measurements (dashed lines) and M94 predictions (solid lines) for the two sites: (a) Ryningsnäs and (b) Høvsøre. The average of the three parameters between two given heights was used to determine model cross-spectra using Equation 2.8 and the coherences were calculated from Equation 2.9.

w-coherence, while the u-coherence was less affected by it. From Figure 2.4, it can be observed that the u-coherence is maximum at lower frequencies ($k_1\Delta z \leq 0.2$ for NNS and 0.1 for NNU) and reduces more quickly with $k_1\Delta z$. The model overestimated u-, v-, and w-coherence at both the sites for all the given ABLs.

In order to assess the performance of the model in coherence predictions, we defined a factor G, such that

$$G = \int_0^3 |\mathrm{coh}_n(k_1\Delta z) - \langle \mathrm{coh}_{n,t}(k_1\Delta z)\rangle| \mathrm{d}(k_1\Delta z), \tag{2.11}$$

which is the absolute area between the coherence estimated from n segments of the time series $\mathrm{coh}_n(k_1\Delta z)$ (dashed lines in Figure 2.4) and the theoretically predicted coherence $\langle \mathrm{coh}_{n,t}(k_1\Delta z)\rangle$ (smooth lines). The model performance in terms of G at both sites is given in Table 2.4 for the coherences shown in Figure 2.4. For a perfect theory the value of G should be close to zero. The model performed relatively better in predicting the u-coherence at both sites for neutral stability and relatively poorly for predicting the v-coherence at both sites for all three stabilities.

Table 2.4: Model performance in terms of G factor in coherence predictions according to Equation 2.11. The coherences are shown in Figure 2.4.

		G	
Stability	coh	Ryningsnäs	Høvsøre
NNS	u	0.15	0.12
	v	0.37	0.33
	w	0.21	0.16
N	u	0.12	0.11
	v	0.31	0.33
	w	0.17	0.12
NNU	u	0.16	0.15
	v	0.32	0.35
	w	0.16	0.17

The cross-spectral phases, which provide the arrival shift time of turbulence at two heights, are shown in Figure 2.5, where it can be observed that $\varphi_v > \varphi_u > \varphi_w$. For NNS, φ_v and φ_u at Ryningsnäs were observed to be greater than those at Høvsøre. The

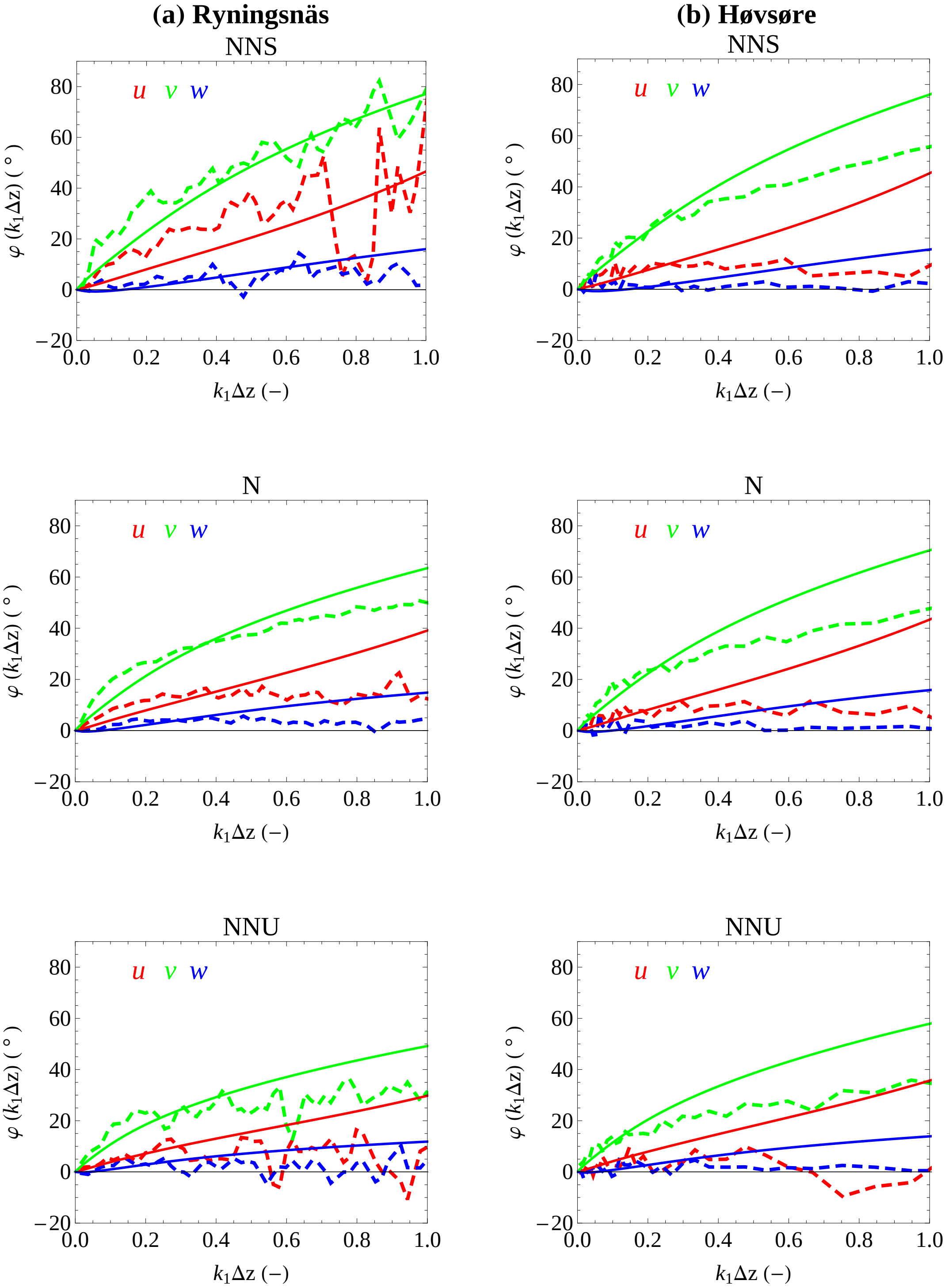

Figure 2.5: Comparions of cross-spectral phases between two heights from model predictions and observations for the (a) Ryningsnäs and (b) Høvsøre sites. The model phases were calculated using Equation 2.10.

phase shift increases with $k_1\Delta z$ $(0 < k_1\Delta z < 1)$ as long as the coherence is non-zero. From Figure 2.5, it is observed that the cross-spectral phases decreased slightly from NNS to NNU. The phase results from the forested area were consistent with those from the study by Chougule et al. [2012].

2.4 Discussion

As can be seen from the left plots of Figure 2.2, the RDT model was able to fit the one-dimensional *u*-, *v*-, *w*-spectra and *uw* co-spectrum reasonably well for forested flow in neutral and near-neutral ABLs. The Δ values from heights other than 80 m, and the velocity bins other than 7-8 ms^{-1} (5-6 and 6-7 ms^{-1}), were consistent with Table 2.2 with Δ for $\langle uw \rangle$ being greatest.

For the Ryningsnäs spectra, we see that the spectra shifted upwards along the ordinate from NNS (via N) to NNU, implying that the turbulent energy increased from NNS to NNU. However, the Ryningsnäs $\alpha\varepsilon^{2/3}$ and L curves (first two plots of first column in Figure 2.3), show that the $\alpha\varepsilon^{2/3}$ values were rather smaller, whereas, the L values were greater for NNU case. So the increased turbulence due to buoyancy effects was expressed in increased length scales which can also be seen from Høvsøre results. Also since the length scales from the two sites were more or less same, the increased turbulence due to the higher roughness was articulated more as an increased $\alpha\varepsilon^{2/3}$. As discussed in Section 3.1, where L from Ryningsnäs were grater than that from Høvsøre for NNU at 100 m, which might be because for the same L_o, the heat flux in Ryningsnäs is much larger than that at Høvsøre, resulting in the higher boundary layer height, which might have an influence on the length scale.

The three parameters from both the sites varied in similar pattern with height for other wind speed bins for all the three stabilities. For lower wind speed bins, both at the Ryningsnäs and Høvsøre site, the $\alpha\varepsilon^{2/3}$ curves shifted to the left with $\alpha\varepsilon^{2/3}$ at Ryningsnäs being approximately 10 times than that at Høvsøre, while L for NNU was slightly decreased, whereas, at Ryningsnäs, Γ remained more or less constant, and the turbulence at Høvsøre became more isotropic with height. From Equation 2.7, it can be observed that the ratio between any two variances (or co-variances), becomes function only of the Γ parameter, so the turbulence anisotropy can directly be represented in terms of that parameter.

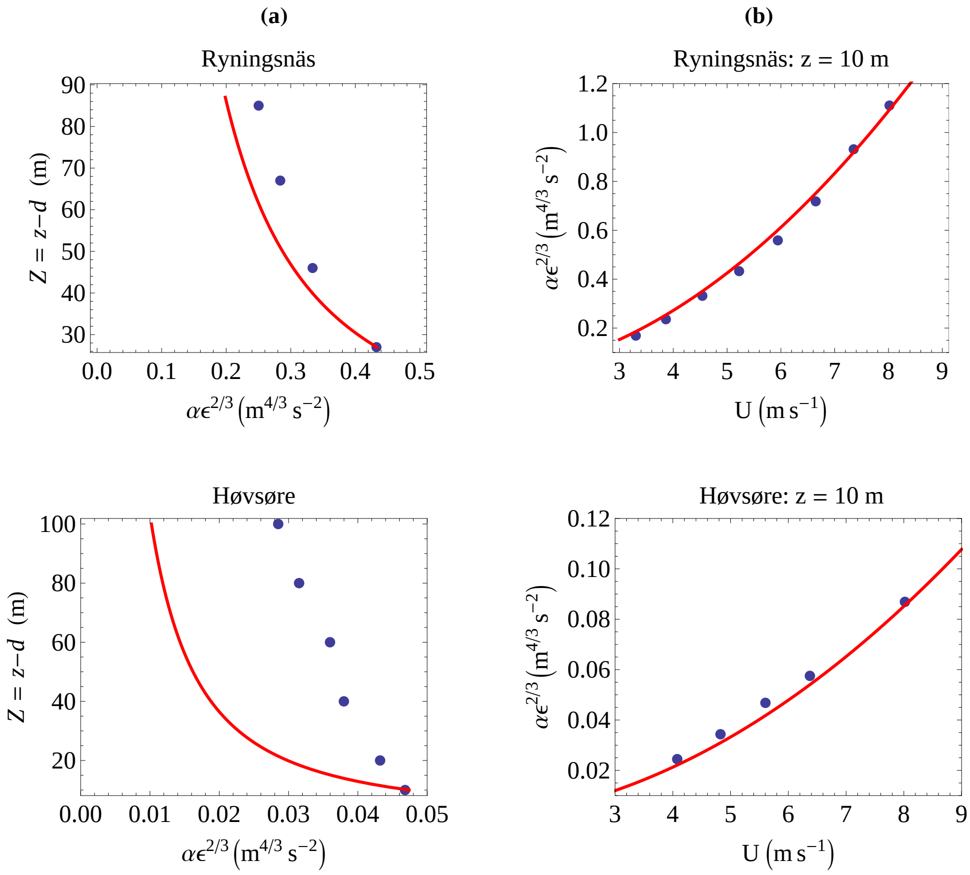

Figure 2.6: Variation of $\alpha\varepsilon^{2/3}$, shown by dots with Z at 7-8 ms^{-1} (column (**a**)) and U (column (**b**)), where $Z = z - d$. The displacement height d for Ryningsnäs is 13 m and that for Høvsøre is 0. The solid lines are the neutral surface-layer scaling: $\alpha\varepsilon^{2/3} \propto Z^{-2/3}$ in column (**a**) and $\alpha\varepsilon^{2/3} \propto U^2$ in column (**b**).

For neutral ABLs at Ryningsnäs, there was no significant variation in L or Γ with the mean wind speed bins 4-5, 5-6, 6-7, 7-8, 8-9, 9-10, and 10-11 ms^{-1}. The standard deviations calculated from these seven wind speed bins were ~ 3.0 m and ~ 0.05 at $z = 80$ m, respectively. This was consistent with the results from the Høvsøre site, as discussed in Sathe et al. [2012]. From Equations 2.9 and 2.10, it can be seen that the model coherences and cross-spectral phases are functions of L and Γ, so they should change very slightly with the mean wind speed in the neutral ABLs, which was also observed from the measurements. With L and Γ at Ryningsnäs insignificantly different from those at Høvsøre, only slight differences of the coherences and the phases between the two sites for NNS, N and NNU, were expected (Figure 2.4 and 2.5), which was consistent with observations. The above discussion was consistent with an other investigated height separation (40-100 m), and the wind speed bins mentioned above, where no significant difference was observed in L and Γ with the mean wind speed for NNS, N and NNU.

Table 2.4 provides information on the performance of the model for coherence predictions for vertical separation. The model performance was better in predicting the u-, and w-coherence than v-coherence, whereas the neutral stability predictions were slightly better than NNS and NNU, at both the sites. The model performed almost equally well at both the sites. We considered non-stationary data in order to obtain more realizations. The non-stationarity effects for Ryningsnäs were negligible, except in NNU case where there was a slight increase in σ_u and Γ, and G was reduced by 30%. Analyses of other height intervals showed similar order of G values for all three stabilities for 7-8 ms^{-1}, with G for v-coherence being the greatest ($\gtrapprox 0.3$). This was in contrast to Mann [1994b], where the w-coherences were predicted poorest (overestimated) by the model. However, in that investigation the spatial separations were horizontal, not vertical, as in the present investigation. In addition to the different height intervals, the values of G from the other wind speed bins were consistent with Table 2.4 for NNS, N and NNU, which could be because of the model coherence is a function of L and Γ which changed insignificantly with the mean wind speed for the three stabilities.

Because neither L nor Γ differ significantly between the two sites, and from the fact that high turbulence levels in forested areas increased loads on the rotor, we would like to analyze $\alpha\varepsilon^{2/3}$ further. Figure 2.6 shows the neutral asymptotic limits (Kaimal and Finnigan [1994]): $\varepsilon \propto U^3/Z$ with $Z = z - d$ for Ryningsnäs and $Z = z$ for Høvsøre, where $d = 13$ m is the displacement height (Bergström et al. [2013]). It can be observed from the Z vs. $\alpha\varepsilon^{2/3}$ curve that, at Høvsøre, the dissipation rate decreased with height more slowly than expected, which might be because the site was not completely homogeneous toward the east. It is known that rough-to-smooth transitions can be felt extremely far downstream from the change (Antonia and Luxton [1972]). The lowest points on the Z vs. $\alpha\varepsilon^{2/3}$ curve are influenced by the relatively smooth terrain close to the site, while the points further up have larger ε than expected due to the trees and forest further east. The dots in the right plots of the Figure 2.6 corresponds to the velocity bins measured at $z = 80$ m, where for Ryningsnäs we selected 8 velocity bins from 5-6 to 11-12 m s^{-1}, while for Høvsøre the velocity bins were 5-6, 6-7, 7-8, 8-9, and 10-11 m s^{-1}.

Due to the limited number of realizations n, there is uncertainty in the estimated (cross-) spectra and hence in the corresponding coherences and phases. Kristensen and Kirkegaard [1986] showed that the coherence was systematically overestimated. However, the overestimation was insignificant for the n values in Table 2.3. The variance of the phase estimate for u, v and w from Kristensen and Kirkegaard [1986] increaseed with $k_1 \Delta z$, with the largest value of the standard deviation being 26° and 19° in φ_u for NNU at $k_1 \Delta z \approx 1$ at Ryningsnäs and Høvsøre, respectively.

2.5 Conclusion

Our aim in this study was, to investigate the performance of the RDT based spectral tensor model in predictions of the velocity spectra, co-spectra and cross-spectra over the forested area, and to compare the results with those from the agricultural landscapes. The RDT model was found to be able to fit the one-dimensional spectra quite well over the forested area. In terms of variances and co-variances, the model performed relatively better in forested area, particularly for neutral ABLs. The spectral tensor model needs only three parameters to describe the spectra: the viscous dissipation rate of TKE, a length scale, and a parameter describing the turbulence anisotropy. The dissipation rate of TKE over the forest canopy was 9 times that over smooth agricultural landscapes. No significant difference was observed in the variations of length scales with height between forested and agricultural areas, while the length scales over the forest canopy were more or less similar to those over agricultural landscapes. The turbulence anisotropy remained more or less constant with height over forested area, whereas it decreased slightly with height in agricultural landscapes. No significant difference was observed in the turbulence anisotropy of the two sites.

The coherences from the RDT model were independent of the dissipation rate of TKE, which was also supported by the measurements. Despite good spectral fits, the model overestimated coherence of all the three velocity components for vertical separations. It performed relatively better in predicting the u-coherence in all stabilities; however, its v-coherence prediction was relatively poor at both the sites. The model performed slightly better for neutral stability than for slightly stable and unstable stratification at both the sites. Generally, there was no large difference between the performance of the model in predictions at the forested and agricultural areas. The flow over forest showed similar phase shifts to those over the agricultural areas. Finally, the dissipation rate parameter of the model was evaluated against a standard expression for neutral surface-layer scaling, where the agreement was better at Ryningsnäs than at Høvsøre.

Acknowledgements

This study was a part of the PhD project funded by the Siemens Wind Power A/S and the WindScanner.dk project, which was funded by the Danish Agency for Science. We would like to thank the Test and Measurements Section of DTU Wind Energy for the acquisition of the Høvsøre data. Vindforsk III, a research program sponsored by the Swedish Energy Agency, is greatly acknowledged. We are also obliged to the COMWIND project funded by the Danish Council of Strategic Research (DSF-contract: 09-067216). The financial support from the Danish Energy Technology Development and Demonstration Program (EUDP) (Project title: Demonstration of a basis for tall wind turbine design, Project no: 64011-0352) is greatly appreciated. Finally, the authors are thankful to Mark Kelly from DTU Wind Energy for providing valuable feedback on the manuscript.

Chapter 3

Modeling of the spectral velocity tensor including buoyancy effects

---

3.1 Introduction

Turbulent motions, due to their fundamentally chaotic and irregular nature, are typically treated statistically rather than deterministically. A flow becomes turbulent when the Reynolds number exceeds a critical value, which depends upon the geometric structure of the flow. In the atmospheric boundary layer (ABL), the Reynolds numbers are always high, so the wind in the ABL is nearly always turbulent. There exists a wide spectrum of spatial and temporal scales in the turbulent ABL. Kolmogorov suggested that, statistically, energy is pumped through the large scales, which in turn is transferred to smaller and smaller scales. The small-scale motions are statistically isotropic. When the Reynolds number becomes small enough (i.e. at small scales), the kinetic energy is dissipated into heat by viscous friction. In the stationarity state, the rate of viscous dissipation must be equal to the rate of production of turbulent energy. Turbulence has its origins in the inherent instabilities of laminar flow. The mechanisms for generating and maintaining turbulence in the atmosphere includes the shear in the mean flow, and buoyancy, where the latter is typically due to heating or cooling of the ground. Kaimal and Finnigan [1994] described how the atmospheric boundary layer (ABL) responds to changes in atmospheric stability.

The different processes in the turbulent motions which take place at different scales—i.e. the production of turbulent energy at larger scales, its transfer to smaller and smaller scales, and finally its viscous dissipation— can be studied by means of spectral representation. The spectrum of velocity fluctuations in the ABL covers millimeters to kilometers in spatial scales and fractions of a second to hours in temporal scales (Kaimal and Finnigan [1994]). If we assume that Taylor's hypothesis of "frozen turbulence" is valid, then the measured one-point time series can be related to spatial fluctuations. The Fourier spectra and cross-spectra of the measurements (of wind speed, say) change with atmospheric stability. The processes described above, and their behavior at different scales, can be studied theoretically by modeling of the *spectral velocity tensor* for homogeneous turbulence; such a representation gives the complete second-order structure of ABL turbulence, including spectra of all velocity components and cross-spectra of any combination of velocity components at two arbitrarily chosen points. In addition to the velocity components, the temperature— which acts as an active scalar by modifying the velocity field through buoyancy— and its spectrum can be modeled. In addition to the velocity variances and co-variances, the resulting spectral tensor, which now includes the temperature, also gives the temperature fluxes for different atmospheric stabilities.

The modeling of the spectral velocity tensor has important implications in wind energy. In addition to the single-point spectra derived from the spectral tensor, the cross-spectra of fluctuations at various points are also important for calculation of dynamic loads on wind turbines. The International Electrotechnical Commission (IEC) (IEC [2005]), recommends the use of the three-dimensional spectral tensor model by Mann [1994b] (M94) for estimation of loads on wind turbines through simulation of rotor inflow (Mann [1998]). The spectral shapes and coherences that the model predicts have previously been compared with data measured over sea, over flat rural terrain, and even in boundary-layer wind-tunnels (Mann [1994a]). Examples of other models which describe the spectra and cross-spectra are those developed by Kristensen et al. [1989], Kaimal et al. [1972], etc. The M94 model differs from the other models mentioned above in many respects. It incorporates rapid distortion theory (RDT) (Pope [2000]; Townsend [1976]) with an assumption of uniform mean shear and consideration of wavenumber-dependent eddy life time, while the model by Kristensen et al. is a kinematic model, and the model by Kaimal et al. is an empirical model incorporating many model parameters. The stationary M94 model is applicable for homogeneous neutral surface-layer turbulence. RDT has previously been used in non-stationary spectral tensor modeling of homogeneous turbulent flows— uniformly sheared (Maxey [1982]), unsheared stably stratified (Hanazaki and Hunt [1996]), and sheared stably stratified (Hanazaki and Hunt [2004]). The M94 model contains three adjustable parameters which are determined from single-point measurements. Although the model was never extended to account for buoyancy effects, it has been used to describe one-point spectra for non-neutral conditions (Peña et al. [2010a]; Sathe et al. [2012]). For the simulation of turbulence in the lower atmosphere and subsequent estimation of its loading effects upon structures in the lower atmosphere, it would be useful to augment the spectral tensor model, to include buoyancy effects. Stable and unstable stratification each have different effects upon the mean wind and turbulence.

In this study an attempt is made to investigate the spectral tensor model of wind velocity fluctuations, including temperature fluctuations, due to the effect of mean uniform vertical shear and the mean uniform temperature gradient. The model is based on RDT, which gives the linearized Navier-Stokes equations in Fourier space. The idea of the present model is based on the previous studies made by Mann 1994 and Hanazaki & Hunt 2004 (HH04). We incorporate the general concept of an eddy life time in order to make the model stationary. The parameterized eddy life time from M94 is used. In addition to the three parameters from M94, the model contains two extra parameters as a result of introducing mean uniform temperature gradient. These parameters are: a stability parameter (the Richardson number) and the rate of destruction of temperature variance.

This chapter summarizes the present state of the theory. In Section 3.2, we provide basic definitions, and the properties of the spectral tensor. Section 3.3-3.5, provide the derivation of the momentum, and the temperature equation, with the assumptions and the considerations described within, along with the RDT limit. In Section 3.6, the Fourier transform of the momentum and the temperature equation is provided, resulting in the governing RDT equations. Section 3.7 of this chapter describes the modeling of the spectral tensor starting from the initial conditions, such as the isotropic state and corresponding spectral tensor, modelled via the von Kármán energy spectrum. The resulting spectral tensor is made stationary via eddy life time described in Section 3.8. We compare the model results with the measurements in Section 3.9, with the analysis and discussion provided in Section 3.10. Finally, we conclude our study with future work.

The definitions, properties and the relationships can also be found elsewhere (Kaimal and Finnigan [1994]; Mann [1994a]; Pope [2000]; Stull [2009]; Wyngaard [2010], etc.). For the purpose of the completeness, derivations for the most of the relationships are presented.

3.2 Definitions and properties

In order to provide the mathematical tools, and the definition of the spectral velocity tensor, let us first consider the periodic, three-dimensional fluctuating velocity field $\boldsymbol{u}'(\boldsymbol{x},t)$, where $\boldsymbol{x} = (x,y,z)$ is the position vector in space. The spectral representation of $\boldsymbol{u}'(\boldsymbol{x},t)$ can be written as

$$\boldsymbol{u}'(\boldsymbol{x},t) = \int \boldsymbol{Z}(\boldsymbol{k},t)\mathrm{e}^{\mathrm{i}\boldsymbol{k}\cdot\boldsymbol{x}}\mathrm{d}\boldsymbol{k}, \tag{3.1}$$

where for the periodic case being considered, $\boldsymbol{Z}(\boldsymbol{k},t)$ is given as (Pope [2000])

$$\boldsymbol{Z}(\boldsymbol{k},t) \equiv \sum_{n=-\infty}^{\infty} c_n \delta(\boldsymbol{k}-\boldsymbol{k}_n), \tag{3.2}$$

where $\boldsymbol{k} = (k_1,k_2,k_3)$ is the wavenumber vector, c_n is the complex Fourier coefficient. The integral in Equation 3.1 forms a Fourier transform pair, where $\boldsymbol{Z}(\boldsymbol{k},t)$ is the Fourier transform of the field $\boldsymbol{u}'(\boldsymbol{x},t)$. Since the mean $\overline{\boldsymbol{u}'}(\boldsymbol{x},t)$ is zero, it follows from Equation 3.1 that the means $\overline{\boldsymbol{Z}}(\boldsymbol{k},t)$ are also zero. Also, since $\boldsymbol{u}'(\boldsymbol{x},t)$ is a real vector, for each $\boldsymbol{k}$, $\boldsymbol{Z}(\boldsymbol{k},t)$ is a complex vector that satisfies conjugate symmetry,

$$\boldsymbol{Z}(\boldsymbol{k},t) = \boldsymbol{Z}^*(-\boldsymbol{k},t), \tag{3.3}$$

where an asterisk denotes the complex conjugate. In wavenumber space, the divergence of fluctuating velocity is given by Fourier transforming $\partial u_i'/\partial x_i$ as

$$\begin{aligned}\int \left(\frac{\partial u_i'}{\partial x_i}\right) \mathrm{e}^{-\mathrm{i}\boldsymbol{k}\cdot\boldsymbol{x}} \mathrm{d}\boldsymbol{x} &= -\int u_i' \frac{\partial}{\partial x_i}\left(\mathrm{e}^{-\mathrm{i}\boldsymbol{k}\cdot\boldsymbol{x}}\right) \mathrm{d}\boldsymbol{x} \\ &= \mathrm{i}k_i \int u_i' \mathrm{e}^{-\mathrm{i}\boldsymbol{k}\cdot\boldsymbol{x}} \mathrm{d}\boldsymbol{x} \\ &= \mathrm{i}k_i Z_i \\ &= \mathrm{i}\boldsymbol{k}\cdot\boldsymbol{Z}, \end{aligned} \tag{3.4}$$

where periodicity and partial integration is used to obtain the first equality, and that the continuity equation $\nabla\cdot\boldsymbol{u}' = 0$ implies that $\boldsymbol{Z}$ is normal to $\boldsymbol{k}$:

$$\boldsymbol{k}\cdot\boldsymbol{Z} = 0. \tag{3.5}$$

The indices $i, j = 1,2,3$ can be used for the velocity components, i.e., $(u_1', u_2', u_3') = (u', v', w')$, and/or for the space vector $(x_1, x_2, x_3) = (x, y, z)$. In later sections, where the scalar field (i.e.temperature) is included, we use the index notations: $l, m = 1,2,3,4$, for the three velocity components and the scalar. Also, we use the notation, '$^{-}$' (overbar) for the mean of a velocity component or a scalar, whereas we use symbol $\langle\ \rangle$ for higher order statistics, while by definition, both notations have the same meaning i.e. $\overline{u'} = \langle u' \rangle$.

Given that $\overline{\boldsymbol{Z}}(\boldsymbol{k},t) = 0$, we consider the second-order statistic— the covariance of two Fourier coefficients— as

$$\langle Z_i(\boldsymbol{k}^\circ,t) Z_j(\boldsymbol{k},t)\rangle. \tag{3.6}$$

Using the definition of $\boldsymbol{Z}(\boldsymbol{k},t)$ in Equation 3.1, the above equation can be expanded further as

$$\begin{aligned}\langle Z_i(\boldsymbol{k}^\circ,t) Z_j(\boldsymbol{k},t)\rangle &\equiv \frac{1}{(2\pi)^6}\left\langle \int u_i'(\boldsymbol{x}^\circ,t)\mathrm{e}^{-\mathrm{i}\boldsymbol{k}^\circ\cdot\boldsymbol{x}^\circ}\mathrm{d}\boldsymbol{x}^\circ \int u_j'(\boldsymbol{x},t)\mathrm{e}^{-\mathrm{i}\boldsymbol{k}\cdot\boldsymbol{x}}\mathrm{d}\boldsymbol{x}\right\rangle, \\ &= \frac{1}{(2\pi)^6}\left\langle \int\int u_i'(\boldsymbol{x}^\circ,t) u_j'(\boldsymbol{x},t)\mathrm{e}^{-\mathrm{i}(\boldsymbol{k}^\circ\cdot\boldsymbol{x}^\circ+\boldsymbol{k}\cdot\boldsymbol{x})}\mathrm{d}\boldsymbol{x}^\circ\mathrm{d}\boldsymbol{x}\right\rangle, \\ &= \frac{1}{(2\pi)^6}\int\int \left\langle u_i'(\boldsymbol{x}^\circ,t) u_j'(\boldsymbol{x},t)\right\rangle \mathrm{e}^{-\mathrm{i}(\boldsymbol{k}^\circ\cdot\boldsymbol{x}^\circ+\boldsymbol{k}\cdot\boldsymbol{x})}\mathrm{d}\boldsymbol{x}^\circ\mathrm{d}\boldsymbol{x}. \end{aligned} \tag{3.7}$$

Let, $\boldsymbol{x} = \boldsymbol{x}^{\circ} + \boldsymbol{r}$, where $\boldsymbol{r}$ is the separation vector, $\mathrm{d}\boldsymbol{x} = \mathrm{d}\boldsymbol{r}$, and the covariance tensor:

$$R_{ij}(\boldsymbol{r},t) = \left\langle u_i'(\boldsymbol{x}^{\circ},t)u_j'(\boldsymbol{x}^{\circ}+\boldsymbol{r},t)\right\rangle, \tag{3.8}$$

and using these definitions in Equation 3.7,

$$\langle Z_i(\boldsymbol{k}^{\circ},t)Z_j(\boldsymbol{k},t)\rangle \quad \equiv \quad \int \mathrm{e}^{-\mathrm{i}(\boldsymbol{k}^{\circ}+\boldsymbol{k})\cdot\boldsymbol{x}^{\circ}}\mathrm{d}\boldsymbol{x}^{\circ}\int R_{ij}(\boldsymbol{r},t)\mathrm{e}^{-\mathrm{i}\boldsymbol{k}\cdot\boldsymbol{r}}\mathrm{d}\boldsymbol{r}. \tag{3.9}$$

From above equation, it can be observed that the covariance of two Fourier coefficients ($\equiv \mathrm{d}R_{ij}$) is zero, or equivalently, these coefficients are uncorrelated, unless $\boldsymbol{k}^{\circ} + \boldsymbol{k} = 0$, i.e., $\boldsymbol{k}^{\circ} = -\boldsymbol{k}$, thus all the information that is contained in $\mathrm{d}R_{ij}$ is,

$$\begin{aligned} \mathrm{d}R_{ij}(\boldsymbol{k},t) &= \langle Z_i(-\boldsymbol{k},t)Z_j(\boldsymbol{k},t)\rangle, \\ &= \langle Z_i^*(\boldsymbol{k},t)Z_j(\boldsymbol{k},t)\rangle. \end{aligned} \tag{3.10}$$

From above discussion, it can be shown that $\mathrm{d}R_{ij}(\boldsymbol{k},t)$ is the Fourier transform of the covariance tensor $R_{ij}(\boldsymbol{r},t)$, and for homogeneous turbulence,

$$R_{ij}(\boldsymbol{r},t) = R_{ji}(-\boldsymbol{r},t). \tag{3.11}$$

In homogeneous turbulence, the spectral velocity tensor is defined as

$$\Phi_{ij}(\boldsymbol{k}) = \frac{1}{(2\pi)^3}\int R_{ij}(\boldsymbol{r})\mathrm{e}^{-\mathrm{i}\boldsymbol{k}\cdot\boldsymbol{r}}\mathrm{d}\boldsymbol{r}, \tag{3.12}$$

where $\int \mathrm{d}\boldsymbol{r} \equiv \int_{-\infty}^{\infty}\int_{-\infty}^{\infty}\int_{-\infty}^{\infty}\mathrm{d}r_1\mathrm{d}r_2\mathrm{d}r_3$. Note that the time dependency has been left out for the simplicity. As shown in Equation 3.12, $\Phi_{ij}(\boldsymbol{k})$ and $R_{ij}(\boldsymbol{r})$ form a Fourier-transform pair, where

$$R_{ij}(\boldsymbol{r}) = \int \Phi_{ij}(\boldsymbol{k})\mathrm{e}^{\mathrm{i}\boldsymbol{k}\cdot\boldsymbol{r}}\mathrm{d}\boldsymbol{k}. \tag{3.13}$$

The problem with the definition in Equation 3.1 is that the two-point correlation R_{ij} does not decay for $|r| \to \infty$, so the spectral representation of the field $\boldsymbol{u}'(\boldsymbol{x},t)$, to be considered as non-periodic, can be given in terms of the Fourier-Stieltjes integral

$$\boldsymbol{u}'(\boldsymbol{x}) = \int \mathrm{e}^{\mathrm{i}\boldsymbol{k}\cdot\boldsymbol{x}}\mathrm{d}\boldsymbol{Z}(\boldsymbol{k}) \tag{3.14}$$

where the integration in Equation 3.14 is over all wavenumber space (Batchelor [1953]). It is observed from Equations 3.1 and 3.14 that $\mathrm{d}\boldsymbol{Z}(\boldsymbol{k})$ in the non-periodic case corresponds to $\boldsymbol{Z}(\boldsymbol{k})\mathrm{d}\boldsymbol{k}$ in the periodic case (Pope [2000]). From Equations 3.8, 3.13, and 3.14,

$$\begin{aligned}\int \Phi_{ij}(\boldsymbol{k})\mathrm{e}^{\mathrm{i}\boldsymbol{k}\cdot\boldsymbol{r}}\mathrm{d}\boldsymbol{k} &= \left\langle \int \mathrm{e}^{\mathrm{i}\boldsymbol{k}^\circ\cdot\boldsymbol{x}^\circ}\mathrm{d}Z_i(\boldsymbol{k}^\circ) \int \mathrm{e}^{\mathrm{i}\boldsymbol{k}\cdot(\boldsymbol{x}^\circ+\boldsymbol{r})}\mathrm{d}Z_j(\boldsymbol{k}) \right\rangle \\ &= \int \mathrm{e}^{\mathrm{i}(\boldsymbol{k}^\circ+\boldsymbol{k})\cdot\boldsymbol{x}^\circ} \int \left\langle \mathrm{d}Z_i(\boldsymbol{k}^\circ)\mathrm{d}Z_j(\boldsymbol{k})\right\rangle \mathrm{e}^{\mathrm{i}\boldsymbol{k}\cdot\boldsymbol{r}} \\ &= \int \left\langle \mathrm{d}Z_i^*(\boldsymbol{k})\mathrm{d}Z_j(\boldsymbol{k})\right\rangle \mathrm{e}^{\mathrm{i}\boldsymbol{k}\cdot\boldsymbol{r}}, \end{aligned} \tag{3.15}$$

so the two-point correlations of the Fourier velocity components are related to the spectral tensor by

$$\frac{\left\langle \mathrm{d}Z_i^*(\boldsymbol{k})\mathrm{d}Z_j(\boldsymbol{k})\right\rangle}{\mathrm{d}k_1\mathrm{d}k_2\mathrm{d}k_3} = \Phi_{ij}(\boldsymbol{k}). \tag{3.16}$$

The spectral tensor $\Phi_{ij}(\boldsymbol{k})$ is a complex quantity that has the properties

$$\Phi_{ij}(\boldsymbol{k}) = \Phi_{ji}^*(\boldsymbol{k}) = \Phi_{ji}(-\boldsymbol{k}), \tag{3.17}$$

$$k_i\Phi_{ij}(\boldsymbol{k}) = k_j\Phi_{ij}(\boldsymbol{k}) = 0, \tag{3.18}$$

which can be interpreted from Equations 3.3 and 3.5.

The spectral tensor contains the information about the second-order statistics of all the three velocity components through indices i, j. For example, on setting $\boldsymbol{r} = 0$ in Equation 3.13 we obtain

$$R_{ij}(0) = \langle u_i' u_j' \rangle = \int \Phi_{ij}(\boldsymbol{k})\mathrm{d}\boldsymbol{k}, \tag{3.19}$$

where $\Phi_{ij}(\boldsymbol{k})$ represents the Reynolds-stress 'density' in wavenumber space. The specific turbulent kinetic energy (TKE), K, will be equal to half the trace of the matrix above, i.e. $\frac{1}{2}R_{ii}(0) = \frac{1}{2}\langle u_i' u_i' \rangle$. The directional information in $\boldsymbol{k}$ can also be removed, by considering the magnitude $k = |\boldsymbol{k}|$, and, further, the energy-spectrum function $E(k)$ is provided such that

$$K = \int_0^\infty E(k)\mathrm{d}k. \tag{3.20}$$

Thus, $E(k)$ is defined as the integration of $\frac{1}{2}\Phi_{ii}(\boldsymbol{k})$ over the surface of the sphere (in wavenumber space) with radius k.

The spectral representation of the cross-correlation of the pair of stochastic processes, taken over a separation $\boldsymbol{r} = (0, \Delta y, \Delta z)$ is given as the set of all cross-spectra

$$\chi_{ij}(k_1, \Delta y, \Delta z) = \frac{1}{2\pi}\int_{-\infty}^{\infty} R_{ij}(x, \Delta y, \Delta z)\mathrm{e}^{-\mathrm{i}k_1 x}\mathrm{d}x, \tag{3.21}$$

which is most often used in practical applications, such as estimation of loads on structures. The connection between the components of the spectral tensor and the cross-spectra is

$$\begin{aligned}\chi_{ij}(k_1, \Delta y, \Delta z) &= \int_{-\infty}^{\infty}\int_{-\infty}^{\infty} \Phi_{ij}(\boldsymbol{k})\mathrm{e}^{\mathrm{i}(k_2\Delta y + k_3\Delta z)}\mathrm{d}k_2\mathrm{d}k_3 \\ &= \int \Phi_{ij}(\boldsymbol{k})\mathrm{e}^{\mathrm{i}(k_2\Delta y + k_3\Delta z)}\mathrm{d}\boldsymbol{k}_\perp, \end{aligned}\tag{3.22}$$

where $\int \mathrm{d}\boldsymbol{k}_\perp = \int_{-\infty}^{\infty}\int_{-\infty}^{\infty}\mathrm{d}k_2\mathrm{d}k_3$. Δy and Δz are transverse and vertical separations, respectively. Using Equation 3.21, the single-point power-spectrum of the ith velocity component (where $\Delta y = \Delta z = 0$), can be given as, $F_i(k_1) = \chi_{ii}(k_1, 0, 0)$ (with no index summation).

The cross-spectral properties, the squared coherence and the cross-spectral phase, defined respectively as

$$\mathrm{coh}_{ij}(k_1, \Delta y, \Delta z) = \frac{|\chi_{ij}(k_1, \Delta y, \Delta z)|^2}{F_i(k_1)F_j(k_1)}, \tag{3.23}$$

$$\varphi_{ij}(k_1, \Delta y, \Delta z) = \arg(\chi_{ij}(k_1, \Delta y, \Delta z)). \tag{3.24}$$

With above discussion, the spectral tensor is modeled using Equation 3.16, where the equation for the evolution of the Fourier modes $\mathrm{d}\boldsymbol{Z}(\boldsymbol{k}, t)$ will be deduced from the Navier-Stokes equations (NSE), where the time dependent, random nature of the field $\boldsymbol{u}'(\boldsymbol{x}, t)$ implies the time-dependence and randomness of the field $\mathrm{d}\boldsymbol{Z}(\boldsymbol{k}, t)$ (in Fourier space). In the next section, we derive the Fourier transform of the NSE, where we use the assumptions of homogeneity, and the RDT limit for the modeling in Equation 3.16.

3.3 Navier-Stokes equation

The governing NSE of the turbulent velocity field $\boldsymbol{u}(\boldsymbol{x},t)$, can be written as

$$\frac{\partial u_i}{\partial t}+u_j\frac{\partial u_i}{\partial x_j}=-\frac{1}{\rho}\frac{\partial p}{\partial x_i}+\nu\frac{\partial^2 u_i}{\partial x_j \partial x_j}-\delta_{i3}g, \tag{3.25}$$

where u_i is the instantaneous ith velocity component, p is the pressure, ρ is the density, ν is the kinematic viscosity, g is the acceleration due to gravity, and neglecting the Coriolis force. The flow can be decomposed into mean and fluctuating parts by Reynolds decomposition:

$$\left.\begin{aligned} \boldsymbol{u}&=\overline{\boldsymbol{u}}+\boldsymbol{u}', \\ p&=\overline{p}+p', \\ \rho&=\overline{\rho}+\rho'. \end{aligned}\right\} \tag{3.26}$$

We treat the pressure term in Equation 3.25 by using Equation 3.26,

$$\begin{aligned} -\frac{1}{\rho}\frac{\partial p}{\partial x_i} &= -\frac{1}{\overline{\rho}+\rho'}\left(\frac{\partial \overline{p}}{\partial x_i}+\frac{\partial p'}{\partial x_i}\right) \\ &\simeq -\left(\frac{1}{\overline{\rho}}-\frac{\rho'}{\overline{\rho}^2}\right)\left(\frac{\partial \overline{p}}{\partial x_i}+\frac{\partial p'}{\partial x_i}\right) \\ &= -\frac{1}{\overline{\rho}}\frac{\partial \overline{p}}{\partial x_i}-\frac{1}{\overline{\rho}}\frac{\partial p'}{\partial x_i}+\frac{\rho'}{\overline{\rho}^2}\frac{\partial \overline{p}}{\partial x_i}+\frac{\rho'}{\overline{\rho}^2}\frac{\partial p'}{\partial x_i}. \end{aligned} \tag{3.27}$$

Considering hydrostatic balance, where the vertical mean pressure gradient is balanced by the specific weight of the fluid, Equation 3.27 can be written neglecting the last term; to second order in the fluctuations (Stull [2009]) this becomes

$$-\frac{1}{\rho}\frac{\partial p}{\partial x_i}=-\frac{1}{\overline{\rho}}\frac{\partial p}{\partial x_i}-\delta_{i3}g\frac{\rho'}{\overline{\rho}}. \tag{3.28}$$

The density of dry air can be calculated using the equation of state of an ideal gas, expressed as a function of temperature and pressure:

$$\rho=\frac{p}{RT}, \tag{3.29}$$

where R is the specific gas constant, $T = \overline{T} + T'$ is absolute temperature. Using Reynolds decomposition from Equation 3.26,

$$\begin{aligned}
\overline{\rho} + \rho' &= \frac{\overline{p} + p'}{R(\overline{T} + T')} \\
\overline{\rho}\left(1 + \frac{\rho'}{\overline{\rho}}\right) &= \frac{\overline{p}}{R\overline{T}} \frac{\left(1 + \frac{p'}{\overline{p}}\right)}{\left(1 + \frac{T'}{\overline{T}}\right)}, \\
\frac{\rho'}{\overline{\rho}} &\simeq \frac{p'}{\overline{p}} - \frac{T'}{\overline{T}} \\
\frac{\rho'}{\overline{\rho}} &= \frac{p'}{\overline{\rho} R\overline{T}} - \frac{T'}{\overline{T}} \qquad (3.30)
\end{aligned}$$

or,

$$\frac{\rho'}{\overline{\rho}} = -\frac{T'}{\overline{T}}. \qquad (3.31)$$

The assumption of $p'/\overline{\rho}R\overline{T} \approx 0$ leading to Equation 3.31, can also be validated from a scaling argument, $p' \equiv \overline{\rho}u'^2$, or, further, $\gamma p'/R\overline{T} = \gamma\overline{\rho}u'^2/c^2$, where γ is the ratio of the heat capacity at constant pressure (c_p) to the heat capacity at constant volume (c_v), and $c = \sqrt{\gamma R\overline{T}}$ is the speed of sound in air, where $\gamma\overline{\rho}u'^2 \ll c^2$ (Wyngaard [2010]). Using the relationship $T'/\overline{T} = \theta'/\overline{\theta}$ (Wyngaard [2010]), where $\theta = \overline{\theta} + \theta'$ is the potential temperature (described in Section 5), and, from Equations 3.31, 3.28, and 3.25, the resulting NSE becomes

$$\frac{\partial u_i}{\partial t} + u_j \frac{\partial u_i}{\partial x_j} = -\frac{1}{\overline{\rho}} \frac{\partial p}{\partial x_i} + \delta_{i3} g \frac{\theta'}{\overline{\theta}} + \nu \frac{\partial^2 u_i}{\partial x_j \partial x_j} - \delta_{i3} g. \qquad (3.32)$$

The above equation contains a buoyancy term, which is the second term on the right side of the above equation. An air parcel feels upwards force (positive buoyancy), when it is warmer than its surroundings, where θ' is positive, and vice versa. It should be noted that, $p \equiv p(\boldsymbol{x}), \overline{\rho} \equiv \overline{\rho}(\boldsymbol{x}), \theta' \equiv \theta'(\boldsymbol{x})$. The equation of motion for the ith fluctuating velocity component can be obtained by inserting the decompositions 3.26

into Equation 3.32,

$$\underbrace{\frac{\mathrm{D}u_i'}{\mathrm{D}t}}_{I} + \underbrace{\overline{u}_j \frac{\partial \overline{u}_i}{\partial x_j}}_{II} + \underbrace{u_j' \frac{\partial \overline{u}_i}{\partial x_j}}_{III} + \underbrace{u_j' \frac{\partial u_i'}{\partial x_j}}_{IV} = \underbrace{-\frac{1}{\overline{\rho}} \frac{\partial \overline{p}}{\partial x_i}}_{V} \underbrace{-\frac{1}{\overline{\rho}} \frac{\partial p'}{\partial x_i}}_{VI} + \underbrace{\delta_{i3} g \frac{\theta'}{\overline{\theta}}}_{VII} + \underbrace{\nu \frac{\partial^2 u_i}{\partial x_j \partial x_j}}_{VIII} - \underbrace{\delta_{i3} g}_{IX}, \tag{3.33}$$

where $\mathrm{D}/\mathrm{D}t \equiv \partial/\partial t + \overline{u}_j \partial/\partial x_j$ is the total derivative. We neglect the non-linear fluctuation terms and the effect of viscosity in the above equation; i.e. terms IV and VIII, respectively. We often consider the mean velocity field,

$$(\overline{u}, \overline{v}, \overline{w}) = (U, 0, 0), \tag{3.34}$$

and, by assuming horizontal homogeneity, term II in Equation 3.33 vanishes. Also, in addition to the horizontal homogeneity, by considering the hydrostatic balance, terms V and IX vanish together; Equation 3.33 becomes

$$\frac{\mathrm{D}u_i'}{\mathrm{D}t} = -\frac{1}{\overline{\rho}} \frac{\partial p'}{\partial x_i} + \delta_{i3} g \frac{\theta'}{\overline{\theta}} - u_j' \frac{\partial \overline{u}_i}{\partial x_j}. \tag{3.35}$$

3.4 Poisson's equation

Taking the divergence on both sides of the Equation 3.32, where for the *i*th velocity component, $\nabla \cdot (\ ) \equiv \partial(\ )/\partial x_i$, and, by using the continuity $\nabla \cdot \boldsymbol{u} = 0$ and Equation 3.26,

$$\frac{\partial \overline{u}_j}{\partial x_i} \frac{\partial \overline{u}_i}{\partial x_j} + \frac{\partial \overline{u}_j}{\partial x_i} \frac{\partial u_i'}{\partial x_j} + \frac{\partial u_j'}{\partial x_i} \frac{\partial \overline{u}_i}{\partial x_j} + \frac{\partial u_j'}{\partial x_i} \frac{\partial u_i'}{\partial x_j} = -\frac{1}{\overline{\rho}} \nabla^2 p + g \frac{\partial}{\partial z} \left(\frac{\theta'}{\overline{\theta}} \right), \tag{3.36}$$

or,

$$\frac{\partial^2}{\partial x_i \partial x_j} (\overline{u}_i \overline{u}_j) + 2 \frac{\partial \overline{u}_j}{\partial x_i} \frac{\partial u_i'}{\partial x_j} + \frac{\partial^2}{\partial x_i \partial x_j} (u_i' u_j') = -\frac{1}{\overline{\rho}} \nabla^2 p + \frac{g}{\overline{\theta}} \frac{\partial \theta'}{\partial z} - g \frac{\theta'}{\overline{\theta}^2} \frac{\partial \overline{\theta}}{\partial z}. \tag{3.37}$$

Taking the mean on both sides of the above equation,

$$\frac{\partial^2}{\partial x_i \partial x_j} (\overline{u}_i \overline{u}_j) + \frac{\partial^2}{\partial x_i \partial x_j} \langle u_i' u_j' \rangle = -\frac{1}{\overline{\rho}} \nabla^2 \overline{p}. \tag{3.38}$$

Neglecting the last term in Equation 3.37 since $(\partial\theta'/\partial z) \gg (\theta'/\overline{T})(\partial\overline{\theta}/\partial z)$, and by subtracting Equation 3.38 from Equation 3.37;

$$2\frac{\partial\overline{u}_j}{\partial x_i}\frac{\partial u_i'}{\partial x_j} + \frac{\partial^2}{\partial x_i \partial x_j}(u_i'u_j' - \langle u_i'u_j'\rangle) = -\frac{1}{\overline{\rho}}\nabla^2 p' + \frac{g}{\overline{\theta}}\frac{\partial\theta'}{\partial z}, \tag{3.39}$$

therefore,

$$-\frac{1}{\overline{\rho}}\nabla^2 p' = 2\frac{\partial\overline{u}_j}{\partial x_i}\frac{\partial u_i'}{\partial x_j} + \frac{\partial^2}{\partial x_i \partial x_j}(u_i'u_j' - \langle u_i'u_j'\rangle) - \frac{g}{\overline{\theta}}\frac{\partial\theta'}{\partial z}. \tag{3.40}$$

The consequence of introducing buoyancy term in the momentum equation is the last term in the above equation. The Poisson equation for p' consists of terms which represent interaction between the turbulent field and mean velocity gradient (first term on right side of Equation 3.40); turbulence-turbulence interaction (second term); and, the effect due to the uniform lapse rate through the gradient of potential temperature fluctuation (last term). The first term in the right side of the Equation 3.40 is proportional to the mean velocity gradient $\partial\overline{u}_j/\partial x_i$, and, scales linearly with $\mathcal{S}$, where

$$\mathcal{S} \equiv (2\overline{S}_{ij}\overline{S}_{ij})^{1/2}, \tag{3.41}$$

and

$$\overline{S}_{ij} = \frac{1}{2}\left(\frac{\partial\overline{u}_i}{\partial x_j} + \frac{\partial\overline{u}_j}{\partial x_i}\right). \tag{3.42}$$

The "slow" turbulence-turbulence term, and the last term in Equation 3.40, are independent of $\partial\overline{u}_j/\partial x_i$. In the rapid-distortion limit, where $\mathcal{S} \to \infty$, the first term on the right side of the equation is dominant, whereas the second term is negligible in comparison. Then Equation 3.40 becomes,

$$-\frac{1}{\overline{\rho}}\nabla^2 p' = 2\frac{\partial\overline{u}_j}{\partial x_i}\frac{\partial u_i'}{\partial x_j} - \frac{g}{\overline{\theta}}\frac{\partial\theta'}{\partial z}. \tag{3.43}$$

3.5 Temperature equation

The potential temperature equation, by neglecting molecular diffusivity, is given by

$$\frac{\partial \theta}{\partial t} + u_j \frac{\partial \theta}{\partial x_j} = 0. \tag{3.44}$$

Using Equations 3.26, 3.34, assuming horizontal homogeneity, and neglecting non-linear terms, Equation 3.44 can be re-written as

$$\frac{\mathrm{D}\theta'}{\mathrm{D}t} = -u_3' \left(\frac{\mathrm{d}\overline{\theta}}{\mathrm{d}z} \right), \tag{3.45}$$

where $\partial \overline{\theta}/\partial z \equiv \mathrm{d}\overline{\theta}/\mathrm{d}z$ is the uniform potential temperature lapse rate. The potential temperature of a parcel of fluid at pressure p is the temperature that the parcel would acquire if adiabatically brought to a standard reference pressure p_0, usually 1000-mb (millibars). The mean potential temperature can be given as $\overline{\theta} = \overline{T} + (g/c_p)\delta z$, where δz is the height difference from the 1000-mb level, i.e. $\mathrm{d}\overline{\theta}/\mathrm{d}z = \partial \overline{T}/\partial z + g/c_p$. By neglecting the specific humidity, Equation 3.45 assumes a uniform lapse rate, to be determined. In neutrally stratified air, $\mathrm{d}\overline{\theta}/\mathrm{d}z = 0$, while for unstable and stable stratifications, the slope is, negative ($\mathrm{d}\overline{\theta}/\mathrm{d}z < 0$) and positive ($\mathrm{d}\overline{\theta}/\mathrm{d}z > 0$), respectively.

3.6 Fourier transform

We Fourier transform the resulting Equations 3.35, 3.45 and 3.43, using the following definitions, where we assume homogeneity of the fluctuations, a constant shear, constant temperature gradient, and that $\overline{\theta}(z)$ does not change significantly with z:

$$\left. \begin{aligned} u_i'(\boldsymbol{x},t) &= \int \mathrm{e}^{\mathrm{i}\boldsymbol{k}(t)\cdot\boldsymbol{x}} \mathrm{d}Z_i(\boldsymbol{k}(t),t), \\ p'(\boldsymbol{x},t) &= \int \mathrm{e}^{\mathrm{i}\boldsymbol{k}(t)\cdot\boldsymbol{x}} \mathrm{d}\Pi(\boldsymbol{k}(t),t), \\ \theta'(\boldsymbol{x},t) &= \int \mathrm{e}^{\mathrm{i}\boldsymbol{k}(t)\cdot\boldsymbol{x}} \mathrm{d}\Theta(\boldsymbol{k}(t),t), \end{aligned} \right\} \tag{3.46}$$

where $\mathrm{d}\Pi(\boldsymbol{k}(t),t)$ and $\mathrm{d}\Theta(\boldsymbol{k}(t),t)$ being the Fourier coefficients of pressure and temperature fluctuations, respectively.

First, we Fourier transform Equation 3.43, using Equation 3.46 in Equation 3.43,

$$-\frac{1}{\overline{\rho}}k^2 \mathrm{d}\Pi(\boldsymbol{k}(t),t) = -2\frac{\partial \overline{u}_j}{\partial x_i}\mathrm{i}k_j \mathrm{d}Z_i(\boldsymbol{k}(t),t) + \frac{g}{\overline{\theta}}\mathrm{i}k_3 \mathrm{d}\Theta(\boldsymbol{k}(t),t). \tag{3.47}$$

For mean vertical shear, $\partial \overline{u}_j/\partial x_i \equiv \mathrm{d}U/\mathrm{d}z$, where $i=3, j=1$ and rewriting Equation 3.47,

$$-\frac{1}{\overline{\rho}}\mathrm{d}\Pi(\boldsymbol{k}(t),t) = -\frac{2}{k^2}\left(\frac{\mathrm{d}U}{\mathrm{d}z}\right)\mathrm{i}k_1 \mathrm{d}Z_3(\boldsymbol{k}(t),t) + \frac{g}{\overline{\theta}}\frac{\mathrm{i}k_3}{k^2}\mathrm{d}\Theta(\boldsymbol{k}(t),t). \tag{3.48}$$

Secondly, Fourier transforming Equation 3.35,

$$\frac{\mathrm{D}}{\mathrm{D}t}\mathrm{d}Z_i(\boldsymbol{k}(t),t) = -\frac{1}{\overline{\rho}}\mathrm{i}k_i \mathrm{d}\Pi(\boldsymbol{k}(t),t) + \delta_{i3}\frac{g}{\overline{\theta}}\mathrm{d}\Theta(\boldsymbol{k}(t),t) - \frac{\partial \overline{u}_i}{\partial x_j}\mathrm{d}Z_j(\boldsymbol{k}(t),t). \tag{3.49}$$

By replacing $\mathrm{d}\Pi(\boldsymbol{k}(t),t)$ in the above equation with that from Equation 3.48,

$$\begin{aligned}\frac{\mathrm{D}}{\mathrm{D}t}\mathrm{d}Z_i(\boldsymbol{k}(t),t) &= \mathrm{i}k_i\left[-\frac{2}{k^2}\left(\frac{\mathrm{d}U}{\mathrm{d}z}\right)\mathrm{i}k_1 \mathrm{d}Z_3(\boldsymbol{k}(t),t) + \frac{g}{\overline{\theta}}\frac{\mathrm{i}k_3}{k^2}\mathrm{d}\Theta(\boldsymbol{k}(t),t)\right] \\ &\quad + \delta_{i3}\frac{g}{\overline{\theta}}\mathrm{d}\Theta(\boldsymbol{k}(t),t) \\ &\quad - \left(\frac{\mathrm{d}U}{\mathrm{d}z}\right)\mathrm{d}Z_3(\boldsymbol{k}(t),t),\end{aligned} \tag{3.50}$$

or,

$$\begin{aligned}\frac{\mathrm{D}}{\mathrm{D}t}\mathrm{d}Z_i(\boldsymbol{k}(t),t) &= \left(2\frac{k_i k_1}{k^2} - \delta_{i1}\right)\left(\frac{\mathrm{d}U}{\mathrm{d}z}\right)\mathrm{d}Z_3(\boldsymbol{k}(t),t) \\ &\quad - \frac{g}{\overline{\theta}}\left(\frac{k_i k_3}{k^2} - \delta_{i3}\right)\mathrm{d}\Theta(\boldsymbol{k}(t),t).\end{aligned} \tag{3.51}$$

Finally, Fourier transforming Equation 3.45, we get

$$\frac{\mathrm{D}}{\mathrm{D}t}\mathrm{d}\Theta(\boldsymbol{k}(t),t) = -\left(\frac{\mathrm{d}\overline{\theta}}{\mathrm{d}z}\right)\mathrm{d}Z_3(\boldsymbol{k}(t),t). \tag{3.52}$$

Equations 3.51, and 3.52 constitute the governing RDT equations for homogeneous turbulent flow that is stratified $(\mathrm{d}\overline{\theta}/\mathrm{d}z)$ and sheared $(\mathrm{d}U/\mathrm{d}z)$ in vertical z direction.

3.6.1 Fourier transform of $\mathrm{D}/\mathrm{D}t$; evolution of wavenumber vector

In this section we provide derivation for the Fourier transform of the total derivative:

$$\frac{\mathrm{D}s}{\mathrm{D}t} = \frac{\partial s}{\partial t} + \bar{u}_j \frac{\partial s}{\partial x_j}, \tag{3.53}$$

where s can be any scalar (like a temperature fluctuation) or, a fluctuating velocity component, and its Fourier counterpart $\mathrm{d}S(\boldsymbol{k}(t),t)$ will be defined according to the definitions in Equation 3.46. In homogeneous turbulence, with a uniform mean velocity gradient, where the mean velocity is zero at the origin, the mean velocity field is

$$\bar{u}_j = x_k \frac{\partial \bar{u}_j}{\partial x_k}. \tag{3.54}$$

Using the above equation in Equation 3.53, and expanding the same term further;

$$\begin{aligned}
x_k \frac{\partial \bar{u}_j}{\partial x_k}\frac{\partial s}{\partial x_j} &= \frac{\partial \bar{u}_j}{\partial x_k}\frac{\partial}{\partial x_j}\left[x_k \int \mathrm{e}^{\mathrm{i}\boldsymbol{k}(t)\cdot\boldsymbol{x}} \mathrm{d}S(\boldsymbol{k}(t),t)\right], \\
&= \frac{\partial \bar{u}_j}{\partial x_k}\frac{\partial}{\partial x_j}\left[\int \frac{1}{\mathrm{i}}\left(\frac{\partial}{\partial k_k}\mathrm{e}^{\mathrm{i}\boldsymbol{k}(t)\cdot\boldsymbol{x}}\right) \mathrm{d}S(\boldsymbol{k}(t),t)\right], \\
&\simeq \frac{\partial \bar{u}_j}{\partial x_k}\frac{\partial}{\partial x_j}\left[-\int \frac{1}{\mathrm{i}}\mathrm{e}^{\mathrm{i}\boldsymbol{k}(t)\cdot\boldsymbol{x}} \frac{\partial}{\partial k_k}\mathrm{d}S(\boldsymbol{k}(t),t)\right], \\
&= -\frac{\partial \bar{u}_j}{\partial x_k}\int k_j \mathrm{e}^{\mathrm{i}\boldsymbol{k}(t)\cdot\boldsymbol{x}} \frac{\partial}{\partial k_k}\mathrm{d}S(\boldsymbol{k}(t),t),
\end{aligned} \tag{3.55}$$

where we assume that the term $\int (1/\mathrm{i})(\partial/\partial k_k)\left(\mathrm{e}^{\mathrm{i}\boldsymbol{k}(t)\cdot\boldsymbol{x}}\mathrm{d}S(\boldsymbol{k}(t),t)\right)$, which arises due to the use of the chain rule in third step in the above relationship, is less dominant.

Using Equation 3.54, and 3.55 in Equation 3.53, and interpreting the rate of change of wavenumber as

$$\frac{\mathrm{d}k_k}{\mathrm{d}t} = -k_j \frac{\partial \bar{u}_j}{\partial x_k}, \tag{3.56}$$

$$
\begin{aligned}
\frac{\mathrm{D}s}{\mathrm{D}t} &= \frac{\partial}{\partial t}\int \mathrm{e}^{\mathrm{i}\boldsymbol{k}(t)\cdot\boldsymbol{x}}\mathrm{d}S(\boldsymbol{k}(t),t) - \frac{\partial \bar{u}_j}{\partial x_k}\int k_j \mathrm{e}^{\mathrm{i}\boldsymbol{k}(t)\cdot\boldsymbol{x}}\frac{\partial}{\partial k_k}\mathrm{d}S(\boldsymbol{k}(t),t), \\
&= \int \mathrm{e}^{\mathrm{i}\boldsymbol{k}(t)\cdot\boldsymbol{x}}\left[\frac{\partial}{\partial t}\mathrm{d}S(\boldsymbol{k}(t),t) - k_j\frac{\partial \bar{u}_j}{\partial x_k}\frac{\partial}{\partial k_k}\mathrm{d}S(\boldsymbol{k}(t),t)\right], \\
&= \int \mathrm{e}^{\mathrm{i}\boldsymbol{k}(t)\cdot\boldsymbol{x}}\left(\frac{\partial}{\partial t} + \frac{\mathrm{d}k_k}{\mathrm{d}t}\frac{\partial}{\partial k_k}\right)\mathrm{d}S(\boldsymbol{k}(t),t), \\
&= \int \mathrm{e}^{\mathrm{i}\boldsymbol{k}(t)\cdot\boldsymbol{x}}\frac{\mathrm{D}}{\mathrm{D}t}\mathrm{d}S(\boldsymbol{k}(t),t). \qquad (3.57)
\end{aligned}
$$

The above definition was used in Equations 3.49, and 3.52. The interpretation in Equation 3.56 can be obtained from the solution $\mathrm{D}s/\mathrm{D}t = 0$ (Pope [2000]).

3.7 Calculations

We use non-dimensional time ξ, defined as

$$
\xi = \left(\frac{\mathrm{d}U}{\mathrm{d}z}\right)t \qquad (3.58)
$$

By representing $\mathrm{d}\Theta(\boldsymbol{k}(t),t)$ in terms of the new quantity $\mathrm{d}Z_4(\boldsymbol{k}(t),t)$, where

$$
\mathrm{d}Z_4(\boldsymbol{k}(t),t) = \frac{g}{\bar{\theta}}\left(\frac{\mathrm{d}U}{\mathrm{d}z}\right)^{-1}\mathrm{d}\Theta(\boldsymbol{k}(t),t), \qquad (3.59)
$$

the new quantity defined above will have dimensions (ms^{-1}). From the above two definitions, the RDT equations including buoyancy in Equations 3.51 and 3.52 can be re-written as

$$
\frac{\mathrm{D}}{\mathrm{D}\xi}\mathrm{d}Z_l(\boldsymbol{k}(\xi),\xi) = \mathrm{M}_{lm}(\boldsymbol{k}(\xi),\xi)\mathrm{d}Z_m(\boldsymbol{k}(\xi),\xi), \qquad (3.60)
$$

where $l,m = 1,2,3,4$;

$$\mathrm{M}_{lm}(\boldsymbol{k}(\xi),\xi) = \begin{bmatrix} 0 & 0 & \frac{2k_1^2}{k^2}-1 & -\frac{k_1k_3}{k^2} \\ 0 & 0 & \frac{2k_1k_2}{k^2} & -\frac{k_2k_3}{k^2} \\ 0 & 0 & \frac{2k_1k_3}{k^2} & -\left(\frac{k_3^2}{k^2}-1\right) \\ 0 & 0 & -Ri & 0 \end{bmatrix}; \tag{3.61}$$

and, the Richardson number, defined as (Kaimal and Finnigan [1994])

$$Ri = \frac{(g/\overline{\theta})\left(\mathrm{d}\overline{\theta}/\mathrm{d}z\right)}{(\mathrm{d}U/\mathrm{d}z)^2}, \tag{3.62}$$

$$= \left(\frac{N}{\mathrm{d}U/\mathrm{d}z}\right)^2, \tag{3.63}$$

where N is the Brunt-Väisälä frequency, and $\overline{\theta}$ is representative of the height of interest as $\mathrm{d}U/\mathrm{d}z$ and $\mathrm{d}\overline{\theta}/\mathrm{d}z$ are.

3.7.1 Initial conditions: isotropic turbulence

For mean vertical shear, and from Equations 3.56 and 3.58, the wavenumber vector after strain time ξ is given by

$$\boldsymbol{k}(\xi) = (k_1, k_2, k_{30} - k_1\xi), \tag{3.64}$$

which gives the evolution of the wavenumber vector in time from an initial wavenumber vector, $\boldsymbol{k}_0 = \boldsymbol{k}(0) = (k_1, k_2, k_{30})$, due to the application of mean vertical shear. For the initial condition, at $t = 0$ the spectral tensor is given as

$$\Phi_{lm}(\boldsymbol{k}_0, 0) = \frac{\langle \mathrm{d}Z_l^*(\boldsymbol{k}_0,0)\mathrm{d}Z_m(\boldsymbol{k}_0,0)\rangle}{\mathrm{d}k_1\mathrm{d}k_2\mathrm{d}k_{30}}. \tag{3.65}$$

In the context of an initial condition, we take $k = |\boldsymbol{k}_0|$, otherwise $k = |\boldsymbol{k}|$.

3.7.1.1 Velocity spectra

We assume as an initial condition a state of isotropic turbulence, where for the velocity components the isotropic tensor is given as (Pope [2000])

$$\Phi_{ij}(\boldsymbol{k}_0,0) = \frac{E(k)}{4\pi k^2}\left(\delta_{ij} - \frac{k_i k_j}{k^2}\right), \tag{3.66}$$

which satisfies (conjugate) symmetry, and the incompressibility given in Equations 3.17 and 3.18, respectively.

We use the form of the energy spectrum $E(k)$, given by von Kármán as

$$E(k) = \alpha\varepsilon^{\frac{2}{3}}L^{\frac{5}{3}}\frac{(Lk)^4}{(1+(kL)^2)^{\frac{17}{6}}}, \tag{3.67}$$

where ε is the rate of viscous dissipation of specific turbulent kinetic energy, L is a length scale and $\alpha \approx 1.7$ is the spectral Kolmogorov constant.

The one-point spectra are defined using Equation 3.21 as

$$F_1(k_1) = \int_{-\infty}^{\infty}\int_{-\infty}^{\infty}\Phi_{11}(\boldsymbol{k}_0,0)\mathrm{d}k_2\mathrm{d}k_{30}, \tag{3.68}$$

where the tensor Φ_{11} is integrated in (k_2,k_{30}) coordinates. In the isotropic case, it corresponds to a circle with radius $k_r^2 = k_2^2 + k_{30}^2 = k^2 - k_1^2$, where $k = |\boldsymbol{k}_0|$, and the infinitesimal area change $\mathrm{d}k_2\mathrm{d}k_{30}$ corresponds to $2\pi k_r \mathrm{d}k_r = 2\pi k\mathrm{d}k$, at given k_1, so Equation 3.68 becomes

$$\begin{aligned} F_1(k_1) &= \int_{k_r=0}^{k_r=\infty}\Phi_{11}(\boldsymbol{k}_0,0)2\pi k_r\mathrm{d}k_r, \\ &= \int_{k=k_1}^{k=\infty}\Phi_{11}(\boldsymbol{k}_0,0)2\pi k\mathrm{d}k. \end{aligned} \tag{3.69}$$

Using Equation 3.66 in Equation 3.69,

$$F_1(k_1) = \frac{9}{55}\alpha\varepsilon^{\frac{2}{3}}\frac{1}{\left(L^{-2}+k_1^2\right)^{\frac{5}{6}}}. \tag{3.70}$$

The single-point v- and w-spectra can be obtained by using $F_1(k_1)$ from the relationship

(Pope [2000])

$$F_2(k_1) = F_3(k_1) = \frac{1}{2}\left[F_1(k_1) - k_1\frac{\mathrm{d}F_1(k_1)}{\mathrm{d}k_1}\right], \tag{3.71}$$

therefore,

$$F_2(k_1) = F_3(k_1) = \frac{3}{110}\alpha\varepsilon^{\frac{2}{3}}\frac{3L^{-2}+8k_1^2}{\left(L^{-2}+k_1^2\right)^{\frac{11}{6}}}. \tag{3.72}$$

3.7.1.2 Temperature spectrum

For temperature, the isotropic three-dimensional spectrum is given as

$$\Phi_{\theta\theta}(\boldsymbol{k}_0, 0) = \frac{S(k)}{4\pi k^2}, \tag{3.73}$$

where $S(k)$ is the potential energy spectrum containing the form of the inertial subrange (Kaimal and Finnigan [1994]) as

$$S(k) = \beta_1\varepsilon^{-1/3}\varepsilon_\theta L^{\frac{5}{3}}\frac{(kL)^2}{\left(1+(kL)^2\right)^{\frac{11}{6}}} \tag{3.74}$$

Here ε_θ is the dissipation rate for half the temperature variance and $\beta_1 = 0.8$ is a universal constant (Kaimal et al. [1972]). The initial one-dimensional temperature spectrum is given as

$$F_\theta(k_1) = \int_{-\infty}^{\infty}\int_{-\infty}^{\infty}\Phi_{\theta\theta}(\boldsymbol{k}_0, 0)\mathrm{d}k_2\mathrm{d}k_{30}, \tag{3.75}$$

As discussed in the previous section, where we converted the cartesian coordinates into the polar coordinates, for the isotropic form,

$$F_\theta(k_1) = \frac{3}{10}\beta_1\varepsilon^{-\frac{1}{3}}\varepsilon_\theta\frac{1}{\left(L^{-2}+k_1^2\right)^{\frac{5}{6}}}. \tag{3.76}$$

From Equations 3.59, 3.73, and 3.74,

$$\Phi_{44}(\boldsymbol{k}_0, 0) = \frac{S'(k)}{4\pi k^2}, \tag{3.77}$$

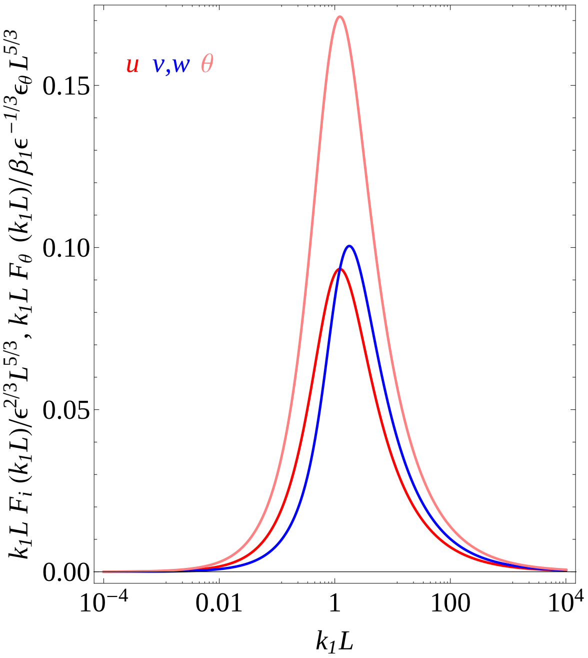

Figure 3.1: Normalized initial velocity and temperature spectra.

where

$$S'(k) = \alpha\varepsilon^{\frac{2}{3}}\beta\eta_\theta L^{\frac{5}{3}}\frac{(kL)^2}{(1+(kL)^2)^{\frac{11}{6}}}, \tag{3.78}$$

$$= \beta\eta_\theta\frac{1+(kL)^2}{(kL)^2}E(k), \tag{3.79}$$

$\beta = \beta_1/\alpha$, and

$$\eta_\theta \equiv \frac{\varepsilon_\theta}{\varepsilon}\left[\frac{g}{\overline{\theta}}\left(\frac{\mathrm{d}U}{\mathrm{d}z}\right)^{-1}\right]^2. \tag{3.80}$$

Finally we combine together the isotropic spectral velocity tensor and three-dimensional temperature spectrum provided in Equations 3.66 and 3.77, and, by assuming zero initial temperature fluxes, letting

$$\mathrm{d}Z_0 = \begin{bmatrix} 0 & k_3 & -k_2 & 0 \\ -k_3 & 0 & k_1 & 0 \\ k_2 & -k_1 & 0 & 0 \\ 0 & 0 & 0 & \sqrt{k^2 \frac{S'(k)}{E(k)}} \end{bmatrix} \times \sqrt{\frac{E(k)}{4\pi k^4}}$$

where

$$\Phi(\boldsymbol{k}_0, 0) = \mathrm{d}Z_0 \cdot \mathrm{d}Z_0^{\mathrm{T}}. \tag{3.81}$$

From the definitions of $E(k)$ and $S'(k)$, $\Phi(\boldsymbol{k}_0, 0)$ becomes a function of $\alpha\varepsilon^{\frac{2}{3}}, L$, and $\beta\eta_\theta$, and can be expressed as

$$\Phi(\boldsymbol{k}_0, 0) \equiv \Phi(\boldsymbol{k}_0, \alpha\varepsilon^{\frac{2}{3}}, L, \beta\eta_\theta). \tag{3.82}$$

The initial velocity and temperature spectra are shown in Figure 3.1.

3.7.2 Anisotropic tensor

We solve the set of RDT Equations 3.60 numerically, using a 4th order Runge-Kutta adaptive time step method (Press et al. [2007]). Let $\mathrm{A} \equiv \mathrm{A}(\boldsymbol{k}, \xi, Ri)$ be the solution matrix obtained for the set of initial conditions I_0, where

$$I_0 = \begin{bmatrix} 1 & 0 & 0 & 0 \\ 0 & 1 & 0 & 0 \\ 0 & 0 & 1 & 0 \\ 0 & 0 & 0 & 1 \end{bmatrix}. \tag{3.83}$$

Therefore the spectral tensor $\Phi(\boldsymbol{k}, \xi)$ formed from the solution of the RDT equations can be given as

$$\Phi(\boldsymbol{k}, \xi) = \mathrm{A} \cdot \frac{\Phi(\boldsymbol{k}_0, 0)}{J} \cdot \mathrm{A}^{\mathrm{T}}, \tag{3.84}$$

where $J = \partial(k_1, k_2, k_3)/\partial(k_1, k_2, k_{30}) = 1$ is the Jacobian. It should be noted that the initial conditions used to obtain the solution matrix A are not that given by Equation 3.81, but by I_0, and that $\Phi(\boldsymbol{k}, 0) = \Phi(\boldsymbol{k}_0)$. From the above equation and Equation 3.61,

$$\Phi(\boldsymbol{k}, \xi) \equiv \Phi(\boldsymbol{k}, \alpha\varepsilon^{\frac{2}{3}}, L, \xi, Ri, \beta\eta_\theta). \tag{3.85}$$

From Equations 3.67, 3.78, and 3.84, it can be proven that

$$\Phi(\boldsymbol{k}, \alpha\varepsilon^{\frac{2}{3}}, L, \xi, Ri, \beta\eta_\theta) = \alpha\varepsilon^{\frac{2}{3}} L^{\frac{11}{3}} \Phi(\boldsymbol{k}L, 1, 1, \xi, Ri, \beta\eta_\theta). \tag{3.86}$$

The application of RDT to flows with both uniform mean shear and constant vertical mean potential temperature gradient has been accomplished in the last decade, but the analysis and focus thus far has mostly been limited to uniform shear with stable stratification, as in Hanazaki and Hunt [2004]. The governing RDT Equations 3.51 and 3.52 have the analytical solutions for $\mathrm{d}Z_3$ and $\mathrm{d}\Theta$ provided in HH04, so the spectral tensor Φ_{lm} with $\{l, m\} = \{3, 3\}, \{4, 4\}$, and $\{4, 3\}$ has an analytical form (Hanazaki and Hunt [2004]). Analytic forms for the other Fourier components are not available ($\mathrm{d}Z_1$ and $\mathrm{d}Z_2$), and hence, for Φ_{lm} with $\{l, m\} = \{1, 1\}, \{1, 2\}, \{1, 3\}, \{1, 4\}, \{2, 2\}, \{2, 3\}$, and $\{2, 4\}$. The Equations 3.60 for Fourier components are solved numerically. The values for Φ_{33}, Φ_{44} and Φ_{43} as functions of ξ from the numerical calculation are compared in Figure 3.2, with that from the analytical solution in Hanazaki and Hunt [2004]. It should be noted that, instead of temperature, the RDT equations in HH04 are in the form of density fluctuations, and that the initial density variance is

$$\Phi_{\rho\rho}(\boldsymbol{k}_0, 0) = \frac{S(k)}{4\pi k^2} 2N^2. \tag{3.87}$$

The purpose of these plots is to show comparisons of the non-stationary solution, and it can be observed (from the last figure in second row), that there is counter-gradient flux (sign change of the $\langle w'\theta' \rangle$ flux), which is untrue for stationary conditions. Also, Φ_{33} from M94 is compared with that from the numerical solution at $Ri = 0$, which is shown in Figure 3.3. The algorithm and the numerics, using the initial conditions mentioned above, were tested by reporducing HH04 results.

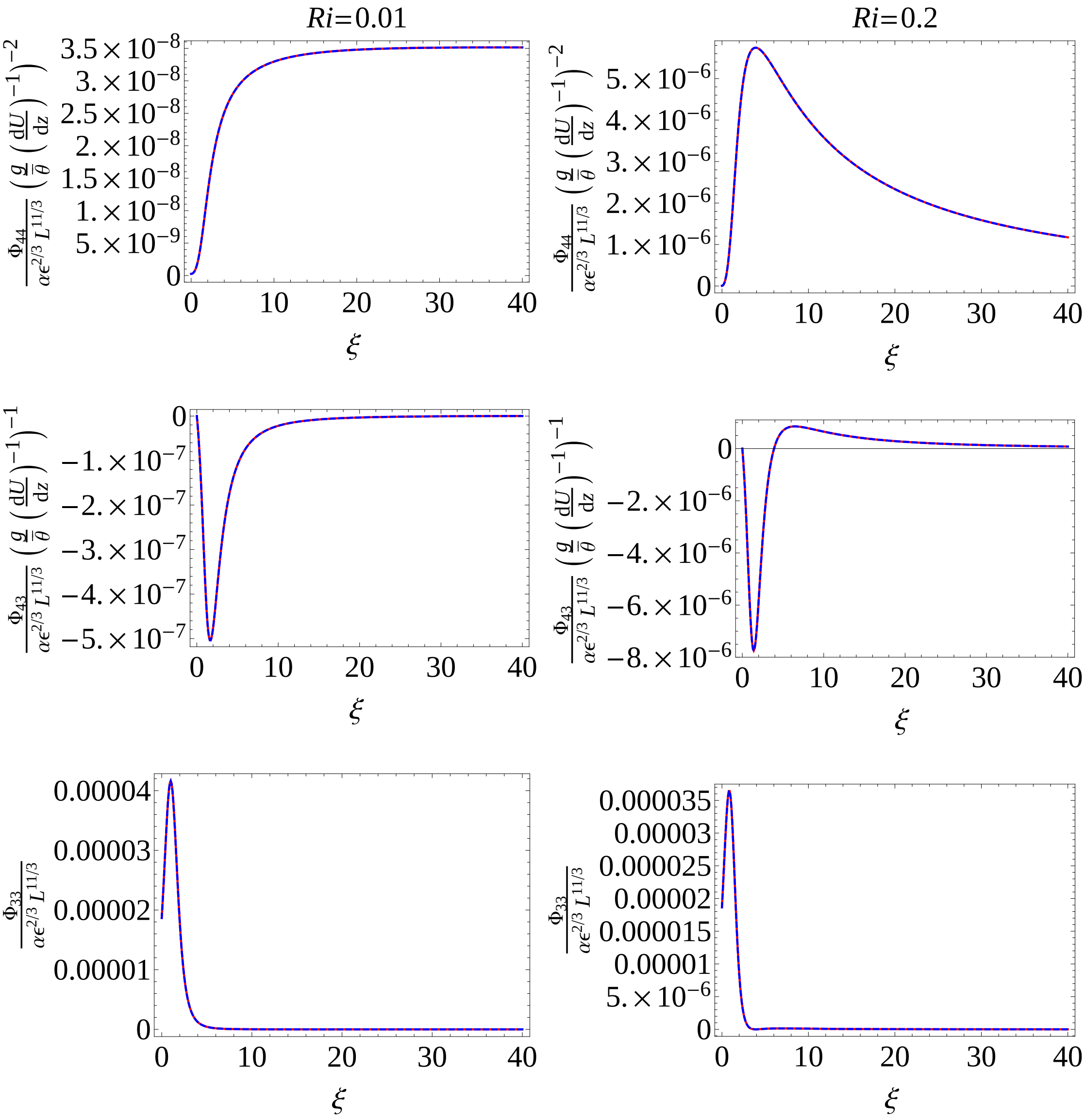

Figure 3.2: The analytical solutions of the spectral tensor components from HH04 (solid lines) shown along with that from numerical calculations (dashed lines) as functions of ξ, at a given initial wavenumber $\boldsymbol{k}_0L = (5,5,5)$, for the same initial temperature variance. The solutions are shown for different values of Ri: $Ri = 0.01$, first column; $Ri = 0.2$, second column; and Φ_{44}, first row; Φ_{43}, second row; Φ_{33}, third row.

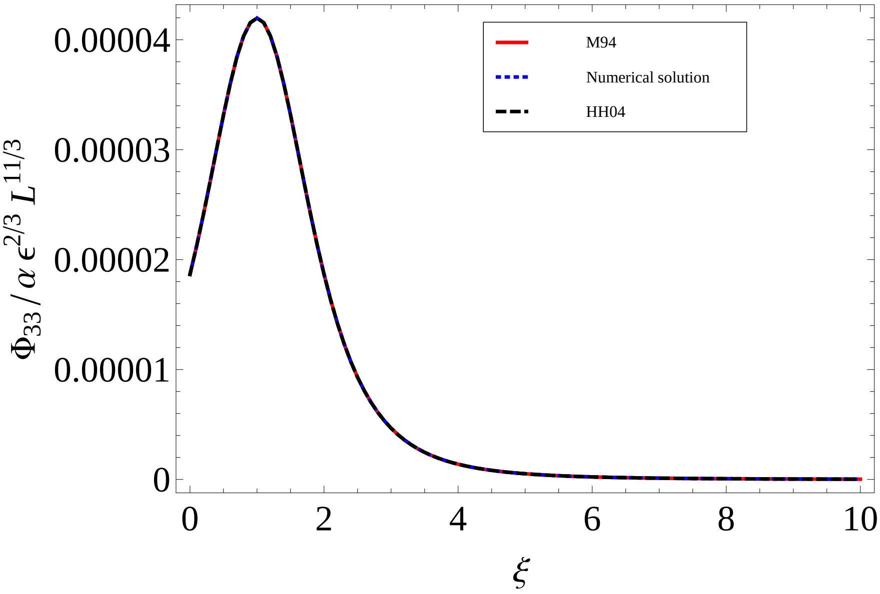

Figure 3.3: Φ_{33} as function of ξ from numerical calculation in comparison with Φ_{33} from M94, for the same initial wavenumber and length scale as in Figure 3.2. Note that the M94 model is a stationary model, and that ξ corresponds to the anisotropy parameter in the model determined from the single point measurement.

3.8 Stationarity and eddy life time

The spectral tensor in Equation 3.86 is non-stationary (time-dependent, via ξ), and the stretching of eddies due to shear for an infinitely long time is unrealistic. The eddies must break at some point due to the stretching. The eddies will stretch or compress depending upon their orientation in the plane of uniform shear. The small scales- more isotropic turbulent eddies, are not affected by shear. In order to make the spectral tensor stationary, we incorporate the general concept of eddy life time from M94 and its parameterization

$$\tau(k) = \Gamma\left(\frac{\mathrm{d}U}{\mathrm{d}z}\right)^{-1}(kL)^{-2/3}\left[{}_2F_1\left(\frac{1}{3},\frac{17}{6};\frac{4}{3};-(kL)^{-2}\right)\right]^{-1/2}, \tag{3.88}$$

where Γ is a parameter to be determined and ${}_2F_1$ is the ‘ordinary’ or ‘Gaussian’ hypergeometric function. We make the spectral tensor in Equation 3.84 stationary by replacing t in Equation 3.58 with the wavenumber-dependent eddy life time given in Equation 3.88, so ξ is exchanged with Γ in the arguments of Φ, and the anisotropic spectral tensor becomes

$$\Phi(\boldsymbol{k}, \alpha\varepsilon^{\frac{2}{3}}, L, \Gamma, Ri, \beta\eta_\theta) = \alpha\varepsilon^{\frac{2}{3}} L^{\frac{11}{3}} \Phi(\boldsymbol{k}L, 1, 1, \Gamma, Ri, \beta\eta_\theta). \tag{3.89}$$

It should be noted that, due to the incorporation of eddy life time in the spectral tensor, the Jacobian term in Equation 3.84 becomes,

$$\begin{aligned} J &= \frac{\partial(k_1, k_2, k_3)}{\partial(k_1, k_2, k_{30})}, \\ &= 1 - k_1 \left(\frac{\mathrm{d}U}{\mathrm{d}z}\right) \frac{\partial \tau(k)}{\partial k_{30}} \\ &= 1 - k_1 \left(\frac{\mathrm{d}U}{\mathrm{d}z}\right) \frac{\partial \tau(k)}{\partial k} \frac{\mathrm{d}k}{\mathrm{d}k_{30}}. \end{aligned} \tag{3.90}$$

For the simplicity, we take $J = 1$, assuming that it might not affect the spectra much but at lower wave numbers it might, and detailed investigation needs to be done. Figure 3.4 illustrates the k dependency of eddy life time and its gradient with k.

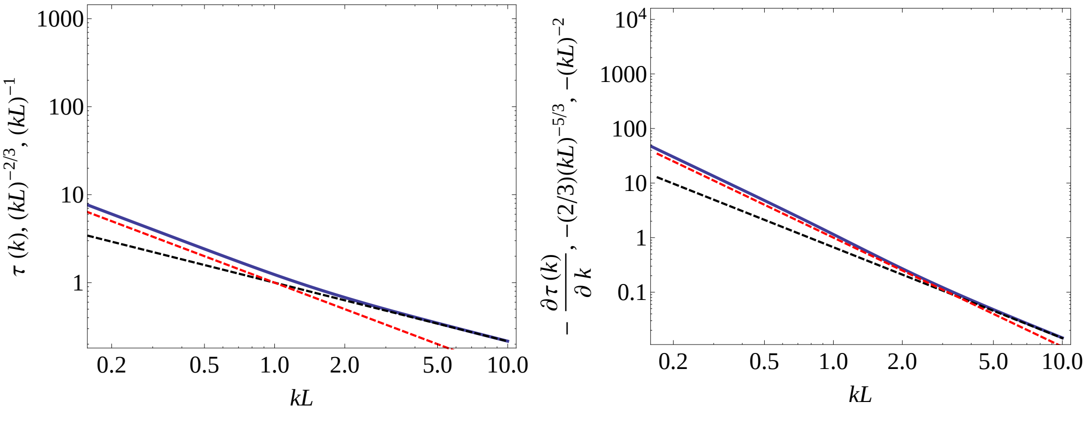

Figure 3.4: Eddy life time (blue) from Mann [1994b] in arbitrary units (left plot), along with its gradient with respect to the wavenumber (right plot). The dashed lines in the left plot are $k^{-2/3}$ (black) and k^{-1} (red), for $k \to \infty$ and $k \to 0$, respectively, and their gradients in the right plot.

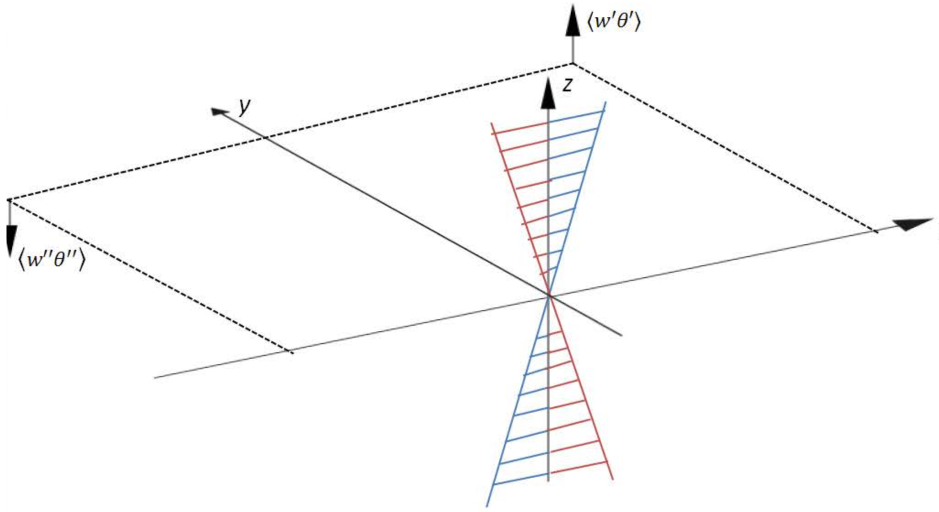

Figure 3.5: Wind velocity field $\boldsymbol{u}(\boldsymbol{x},t)$ subjected to uniform mean shear and uniform temperature gradient along z-axis, as shown in the coordinate system. In this example, the turbulent fluctuations are enhanced by positive heat flux (unstable stratification) and that $\langle w'\theta' \rangle = -\langle w''\theta'' \rangle$, due to 180° rotation of the field about the y-axis.

As described in Mann [1994b], the velocity components of the spectral tensor model in Equation 3.89 satisfiy the symmetry group

$$\left\{ I, \begin{pmatrix} 1 & 0 & 0 \\ 0 & -1 & 0 \\ 0 & 0 & 1 \end{pmatrix}, \begin{pmatrix} -1 & 0 & 0 \\ 0 & 1 & 0 \\ 0 & 0 & -1 \end{pmatrix}, -I \right\}, \tag{3.91}$$

where I is the identity matrix. The statistics should remain unchanged under some rotations and reflections in the coordinate system shown in Figure 3.5. We neglect the effect due to Earth's rotation, so Φ_{ij} should satisfy left-right symmetry (second element in Equation 3.91). We also neglect the effect of gravity, where the fluctuating field has the symmetry about y-axis (third element). So, for any matrix T, from the above symmetry group, the spectral velocity tensor in Equation 3.89 satisfies the relation

$$\Phi(\boldsymbol{k}L, 1, 1, \Gamma, Ri, \beta\eta_\theta) = T \cdot \Phi(T \cdot \boldsymbol{k}L, 1, 1, \Gamma, Ri, \beta\eta_\theta) \cdot T^{\mathrm{T}}, \tag{3.92}$$

where we consider only the velocity component from Φ.

3.9 Data comparison

3.9.1 Method

We estimate the velocity (auto-) spectra and co-spectrum of u and w from the measured time series as

$$F_{ij}(f,z) \equiv \langle \hat{u}_i(f)\hat{u}_j^*(f)\rangle, \tag{3.93}$$

and the temperature spectrum and the component-wise kinematic heat fluxes, respectively as

$$\begin{aligned} F_\theta(f,z) &\equiv \langle \hat{\theta}(f)\hat{\theta}^*(f)\rangle, && (3.94)\\ F_{i\theta}(f,z) &\equiv \langle \hat{u}_i(f)\hat{\theta}^*(f)\rangle, && (3.95) \end{aligned}$$

where $\hat{u}_i(f)$, and $\hat{\theta}(f)$ are the complex-valued Fourier transforms of the ith velocity component, and temperature, respectively at height z.

We select the data according to the classification of atmospheric stability in terms of the Obukhov length L_o following Gryning et al. [2007]. The measured spectra and co-spectra given above change with atmospheric stability (Kaimal et al. [1972]), i.e., $F_{lm}(f,z)$ is a function of L_o.

From Equations 3.22, and 3.89, the model cross-spectrum between any two velocity components, or, between any velocity component and temperature, is given as

$$\begin{aligned} \chi_{lm}(k_1,\Delta y,\Delta z) &= \alpha\varepsilon^{\frac{2}{3}}L^{\frac{5}{3}}\int \Phi_{lm}(\boldsymbol{k}L,1,1,\Gamma,Ri,\beta\eta_\theta)\mathrm{e}^{\mathrm{i}(k_2\Delta y+k_3\Delta z)}\mathrm{d}\boldsymbol{k}_\perp L^2,\\ &\equiv \chi_{lm}(k_1,\alpha\varepsilon^{\frac{2}{3}},L,\Gamma,Ri,\beta\eta_\theta,\Delta y,\Delta z). && (3.96) \end{aligned}$$

The model parameters at any height z, are obtained by fitting model one-dimensional (co-) spectra $\chi_{lm}(k_1,\alpha\varepsilon^{2/3},L,\Gamma,Ri,\beta\eta_\theta,0,0)$, with measured power-spectra (including co-spectra $uw, u\theta$ and $w\theta$) from Equations 3.93, 3.94, and 3.95, and using Taylor's hypothesis: $k_1 = 2\pi f/U$, where U is the mean wind speed at z. The model parameters are used as inputs to estimate the model cross-spectra. Model coherences and cross-spectral phases are compared with those from the measurements.

For vertical separations Δz ($\Delta y = 0$), the set of all the coherences and the cross-spectral phases are given, from Equations 3.23, and 3.24, respectively, as

$$\begin{aligned}\mathrm{coh}_{lm}(\overline{k_1},\Delta z) &= \frac{|\chi_{lm}(\overline{k_1},\alpha\varepsilon^{2/3},\overline{L},\overline{\Gamma},\overline{Ri},\beta\overline{\eta_\theta},\Delta z)|^2}{F_l(\overline{k_1},\alpha\varepsilon^{2/3},\overline{L},\overline{\Gamma},\overline{Ri},\beta\overline{\eta_\theta})F_m(\overline{k_1},\alpha\varepsilon^{2/3},\overline{L},\overline{\Gamma},\overline{Ri},\beta\overline{\eta_\theta})}, \\ &\equiv \mathrm{coh}_{lm}(\overline{k_1},\overline{L},\overline{\Gamma},\overline{Ri},\beta\overline{\eta_\theta},\Delta z), \qquad (3.97) \\ \varphi_{lm}(\overline{k_1},\Delta z) &= \arg(\chi_{lm}(\overline{k_1},\alpha\varepsilon^{2/3},\overline{L},\overline{\Gamma},\overline{Ri},\beta\overline{\eta_\theta},\Delta z)), \\ &\equiv \varphi_{lm}(\overline{k_1},\overline{L},\overline{\Gamma},\overline{Ri},\beta\overline{\eta_\theta},\Delta z), \qquad (3.98)\end{aligned}$$

where $F_l = \chi_{ll}(\overline{k_1},\alpha\varepsilon^{2/3},\overline{L},\overline{\Gamma},\overline{Ri},\beta\overline{\eta_\theta},0,0)$ (no index summation). The parameters $\overline{L},\overline{\Gamma},\overline{Ri}$, and $\overline{\eta_\theta}$, are averaged over two heights z_1 and z_2 (so that $\Delta z = z_2 - z_1$), and $\overline{k_1} = 4\pi f/(U_1+U_2)$. The model coherences and cross-spectral phases are independent of $\alpha\varepsilon^{2/3}$, which can be seen from Equation 3.96 and the definitions above. The cross-spectra, coherences, and cross-spectral phases are calculated from the measurements using general definitions, which can be found in Chougule et al. [2012].

3.9.2 Experimental data

Experimental data are obtained from measurements taken from the 116.5 m tall mast located at the coordinates 56°26′26″N, 08°09′03″E in the Høvsøre test site near the west coast of Denmark. Metek sonic anemometers (USA-1, Basic, Metek Gmbh), with a sampling frequency of $f = 20$ Hz, and measuring in three dimensions, are installed on the mast, at heights of 10, 20, 40, 60, 80, and 100 m. The land to the east of the mast is flat, consisting mostly of agricultural landscapes. Five wind turbines are placed to the north of the mast.

To avoid the wake effects of wind turbines, winds are selected from the region between 60° and 120°. Around 65° and at 8 km from the mast, there are lines of trees and a big forest that extends about 12 km in both north-south and east-west directions. A small village is situated at approximately 100° about 2.8 km from the mast, which could also have affected the flow downstream to west. On the west side of the mast, land extends 1500 m to the North Sea coast, including a dune. More details about the location and instrumentation can be found in Sathe et al., 2012]. The statistical analysis is done using seven years of data from 2004 to 2010, and the analysis is based on 30 minute intervals.

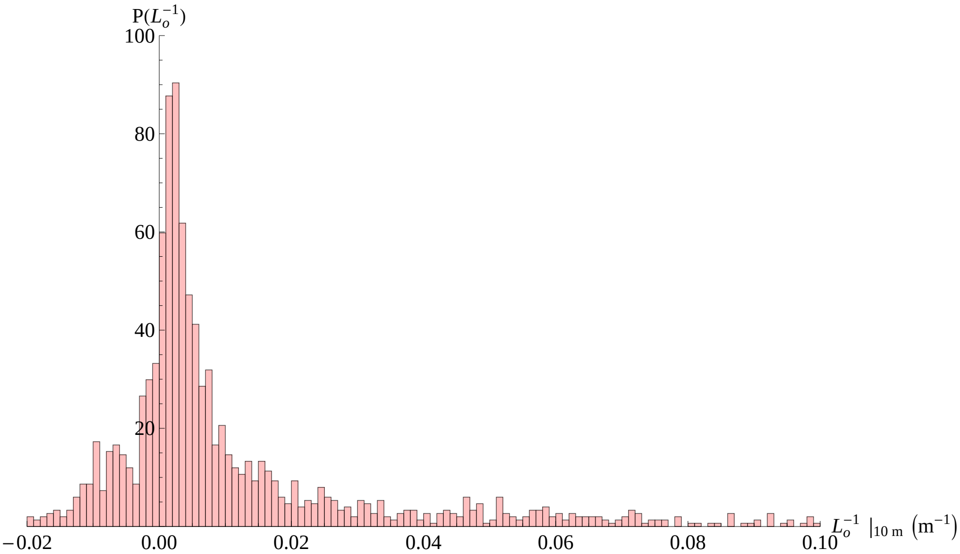

Figure 3.6: Histogram of atmospheric stabilities based on the Obukhov lengths at wind speed 8–9 ms^{-1} for wind directions between 60° and 120° at the Høvsøre test site in the west coast of Denmark.

3.9.3 Data selection

Table 3.1: Classification of atmospheric stability according to inverse Obukhov length intervals (in m^{-1}).

Stable (S)	$0.005 \leq L_o^{-1} \leq 0.02$
Near-neutral stable (NNS)	$0.002 \leq L_o^{-1} \leq 0.005$
Near-neutral unstable (NNU)	$-0.005 \leq L_o^{-1} \leq -0.002$
Unstable (U)	$-0.01 \leq L_o^{-1} \leq -0.005$

Data are selected based on a narrow wind speed interval measured at 80 m height as well as bins of L_o measured at 10 m, where L_o is the Obukhov length (c.f. Chapter 2, Equation 2.2). We analyze S, NNS, NNU, and U stability cases (c.f. Table 3.1). The results for the wind speed bin 8–9 ms^{-1} are provided. Figure 3.6 shows the histogram of atmospheric stability in terms of L_o from the Høvsøre site, for the velocity bin 8–9 ms^{-1}.

3.9.4 Spectra

Just as the temperature Fourier components $\mathrm{d}\Theta$ have been re-dimensionalized by the pre-factor $\frac{g}{\overline{\theta}}\left(\frac{\mathrm{d}U}{\mathrm{d}z}\right)^{-1}$ to become $\mathrm{d}Z_4$, which has the same dimensions as the Fourier velocity components $\mathrm{d}Z_i$ (see Equation 3.59), the corresponding (co-) spectra become

$$F_\theta(k_1) = \left[\frac{g}{\overline{\theta}}\left(\frac{\mathrm{d}U}{\mathrm{d}z}\right)^{-1}\right]^{-2} F_4(k_1), \qquad (3.99)$$

$$F_{i\theta}(k_1) = \left[\frac{g}{\overline{\theta}}\left(\frac{\mathrm{d}U}{\mathrm{d}z}\right)^{-1}\right]^{-1} F_{i4}(k_1). \qquad (3.100)$$

Table 3.2: The pre-factor $(g/\overline{\theta})(\mathrm{d}U/\mathrm{d}z)^{-1}$ in the Equation 3.59 determined from the measurements.

Cases	40 m	60 m	80 m
S	0.7	0.8	0.9
NNS	0.9	1.0	1.2
NNU	1.3	1.8	2.6
U	1.6	2.8	3.7

The pre-factors determined from the measurements at the Høvsøre test site are given in Table 3.2. The spectra and co-spectra are shown in Figure 3.7 at $z = 40$ m for S (top plots) and NNS (bottom plots) atmospheric stabilities, and those for NNU and U are shown in Figure 3.8. It is observed that the model seems to perform better for stable stratifications than that for unstable stratifications, particularly in predicting the $u\theta$ co-spectrum. Also, a sharp increase in the u- spectra at lower wavenumbers, both in NNU, and U stability cases, is noticeable, which also causes an increase in the uw and $u\theta$ spectra at lower frequencies (c.f. Figure 3.8). The parameter values from the model fits are shown in Table 3.3.

3.9.5 Cross-spectra

The normalized cross-spectra, sometimes known as the squared coherences, defined in Equation 3.23, are shown in Figure 3.9 for S, NNS, and NNU, between heights $z_1 = 40$

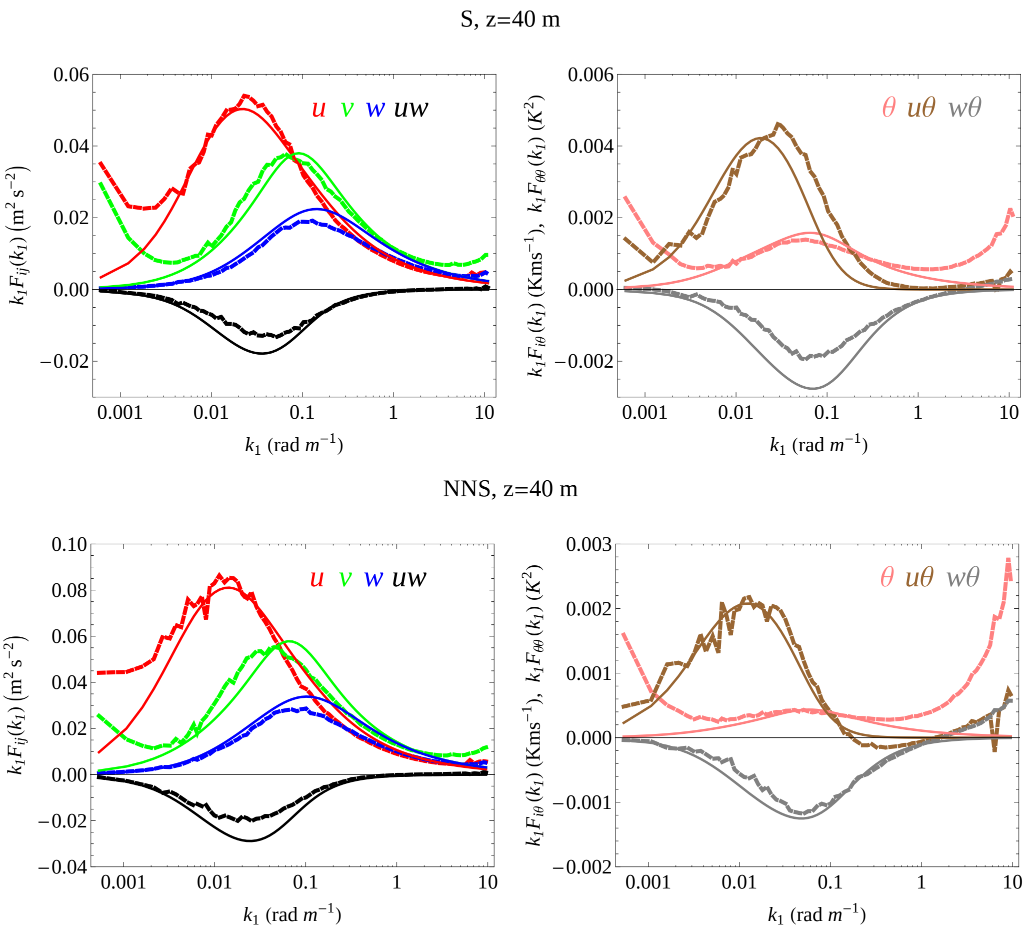

Figure 3.7: Model spectral fits (smooth lines) for S and NNS with the data (ragged lines) at $z = 40$ m and the wind speed bin 8–9 ms^{-1}.

Table 3.3: The spectral tensor parameters from the fits for S, NNS, NNU, and U stability cases at the Høvsøre site for the velocity bin 8–9 m s^{-1}. The number of 30-minute time series n for each case are also provided in the table. The measurements are taken from sonic anemometer located at $z = 40$ m.

Stability	n	$\alpha\varepsilon^{2/3}$ (m$^{4/3}$ s^{-2})	L (m)	Γ	Ri	η_θ
S	359	0.053	15	3.0	0.06	0.02
NNS	298	0.065	20	3.1	0.03	0.012
NNU	71	0.06	30	3.01	-0.032	0.025
U	106	0.0635	35	2.5	-0.033	0.15

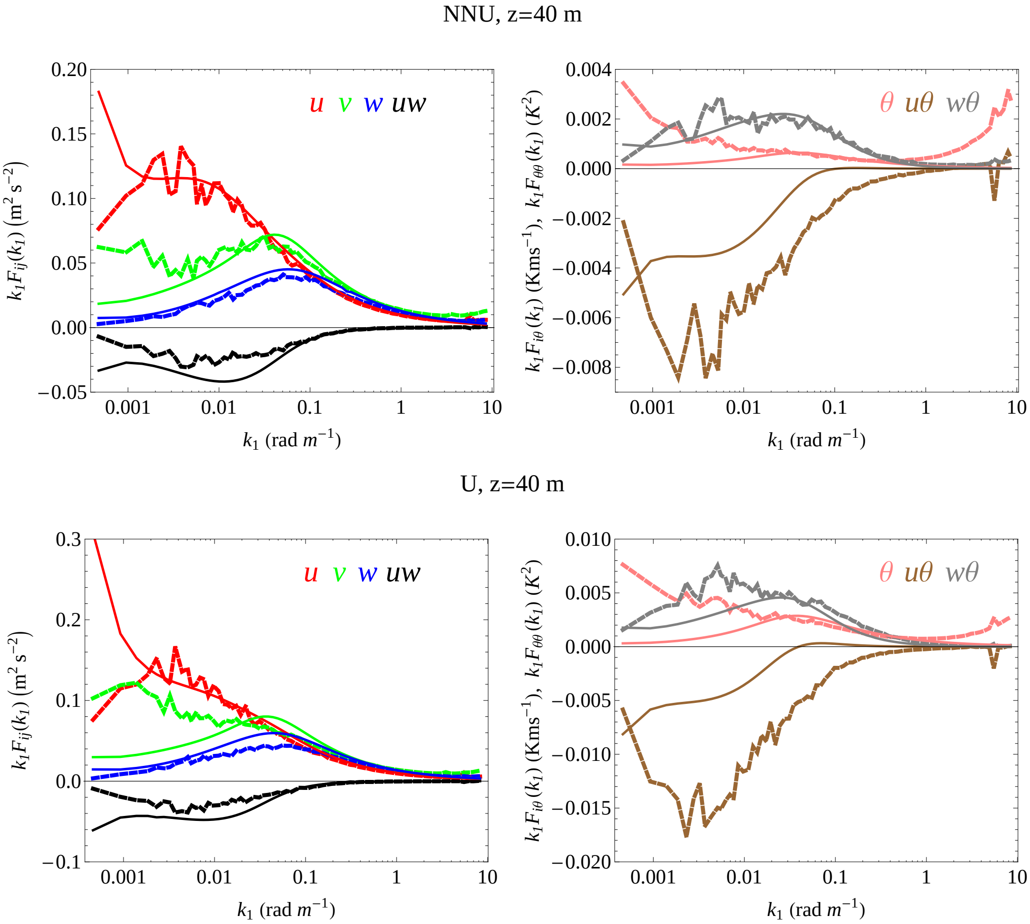

NNU, z=40 m

U, z=40 m

Figure 3.8: NNU and U spectral fits. Notation follows from Figure 3.7.

and $z_2 = 60$ m, along with the cross-spectral phases defined in Equation 3.24.

From their definitions, coherences and cross-spectral phases are not influenced by the weighting factor, so that $\mathrm{coh}_{\theta\theta} = \mathrm{coh}_{44}$, and $\mathrm{coh}_{i\theta} = \mathrm{coh}_{i4}$, and the same is true for phases. We use averaged parameters obtained from the model one-dimensional spectral fits at $z_1 = 40$ m and $z_2 = 60$ m as inputs to estimate model coherences and cross-spectral phases. The averaged parameters are provided in Table 3.4, where the stability class U has been omitted due to the poor performance of the model.

It is observed from the figures that the coherence predictions of the model for stable stratifications are better than that for NNU, except at the lower frequencies. Also, the model predicts u-coherence very well during stable conditions. The phase plots shows that $\varphi_v > \varphi_u > \varphi_w$, and that the model predicts the same. It is also observed that the

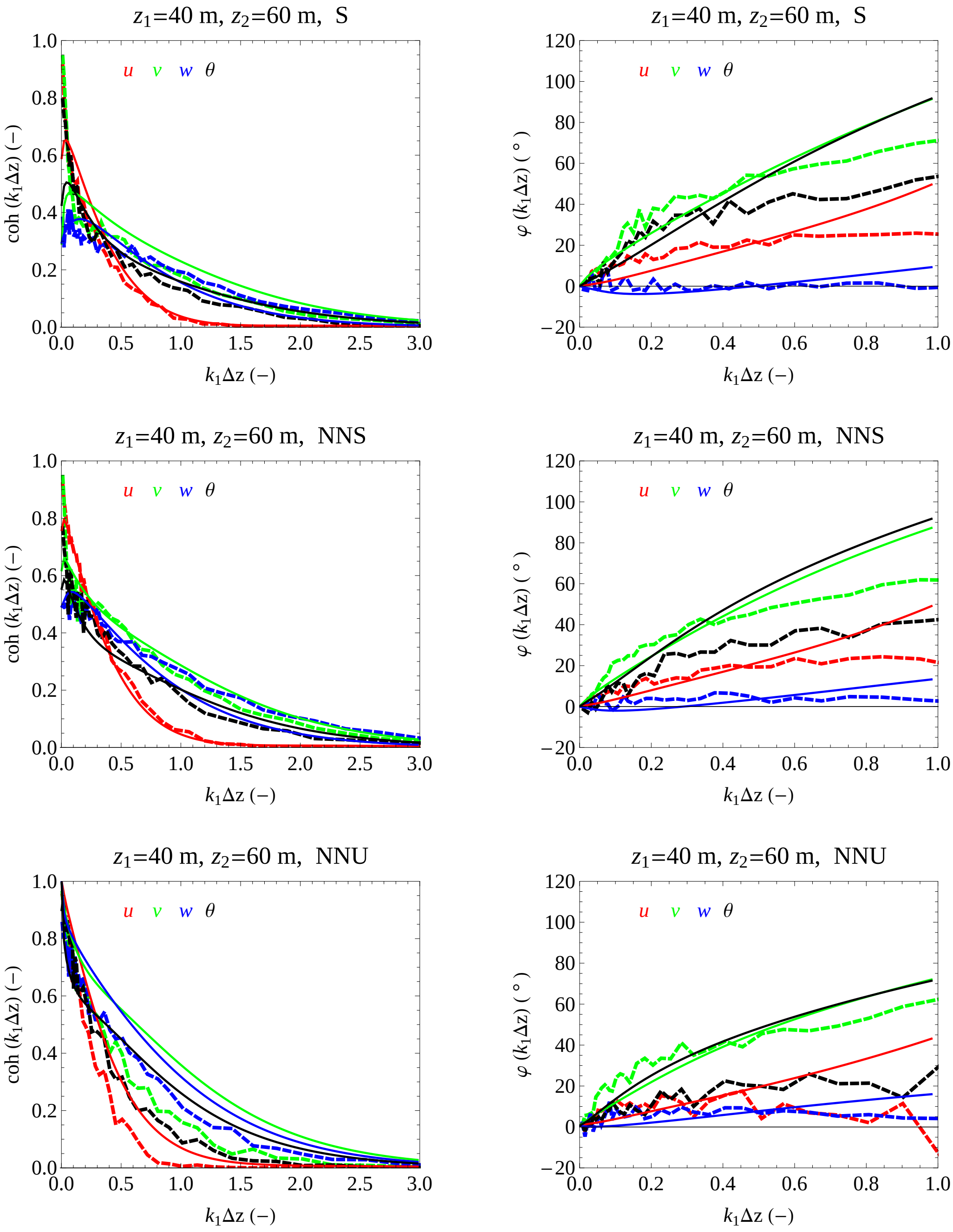

Figure 3.9: Comparisons of the coherences (left plot), and the cross-spectral phases (right plot), from the measurements (dashed lines), and the model predictions (solid lines) from the Høvsøre data, for S, NNS and NNU ABLs. The average of the model parameters between two given heights, 40 and 60 m, is used to determine model cross-spectra using Equation 3.22, and the coherences and the phases are calculated from Equations 3.23, and 3.24, respectively.

Table 3.4: The average of the parameters obtained from the fits at $z_1 = 40$ m and $z_2 = 60$ m for S, NNS, and NNU stability cases at the Høvsøre site for the velocity bin 8–9 m s^{-1}. These parameters are used as inputs to estimates the coherences and the phases given in Equations 3.23 and 3.24, respectively.

Stability	$\overline{L}$ (m)	$\overline{\Gamma}$	$\overline{Ri}$	$\overline{\eta}_\theta$
S	17.5	3.0	0.06	0.027
NNS	22.5	3.05	0.028	0.012
NNU	40	3.0	-0.026	0.037

measured φ_θ lies between φ_v and φ_u, whereas the model shows that $\varphi_v = \varphi_\theta$. More analysis on the phases can be found in Chougule et al. [2012].

3.10 Discussion

In order to get an insight of the ranges of the parameters Ri, and η_θ in the spectral tensor model in Equation 3.89, we use the empirical relations from Kaimal and Finnigan [1994], inspired by Monin-Obukhov similarity theory (MOST). However, we do not incorporate these formulations into our model, and the sole purpose of using these formulations is to get an idea of what ranges of the parameters should be expected. In steady state, ε and ε_θ are given by

$$\varepsilon = -\langle u'w' \rangle \left(\frac{\mathrm{d}U}{\mathrm{d}z} \right) + \frac{g}{\overline{\theta}} \langle w'\theta' \rangle, \tag{3.101}$$

and,

$$\varepsilon_\theta = -\langle w'\theta' \rangle \left(\frac{\mathrm{d}\overline{\theta}}{\mathrm{d}z} \right), \tag{3.102}$$

respectively. The dissipation rate of TKE is equal to the shear production (first term in Equation 3.101) plus the buoyant production (second term in Equation 3.101). The shear production term is always positive, whereas the buoyant production term can be positive (source) or negative (sink), depending upon the vertical temperature flux $\langle w'\theta' \rangle$. The sign of $\langle w'\theta' \rangle$ is generally opposite of the sign of the temperature lapse rate, as described in Figure 3.10, where $\langle w'\theta' \rangle$ is always positive for unstable stratifi-

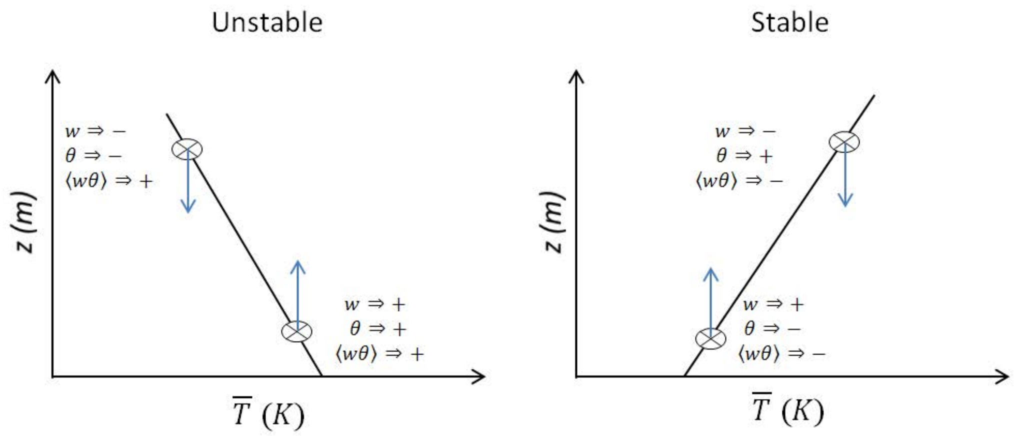

Figure 3.10: An illustration of influence of temperature lapse rate on the vertical temperature flux, which acts as source or sink in the turbulence production via buoyancy term, depending on whether unstable or stable stratification, respectively. An air parcel assumed to be moved adiabatically in the direction of arrow from the position indicated by, $\otimes$.

cation, whereas it is negative for stable stratification. By using the above relationships in Equation 3.80, we get

$$\eta_\theta = \frac{Ri}{R_f^{-1} - 1}, \tag{3.103}$$

where R_f is the flux Richardson number, and can be given as (Kaimal and Finnigan [1994])

$$\begin{aligned} R_f &= \frac{(g/\overline{\theta})\langle w'\theta'\rangle}{\langle u'w'\rangle(\mathrm{d}U/\mathrm{d}z)}, \\ &\simeq \frac{K_h}{K_m} Ri, \end{aligned} \tag{3.104}$$

where K_m, and K_h are the turbulent exchange coefficients for momentum and heat, respectively. Using relationships from Kaimal and Finnigan [1994] for Ri and K_m/K_h,

$$Ri = \begin{cases} z/L_o, & -2 \leq z/L_o \leq 0, \\ (z/L_o)(1+5z/L_o)^{-1}, & 0 \leq z/L_o \leq 1, \end{cases} \tag{3.105}$$

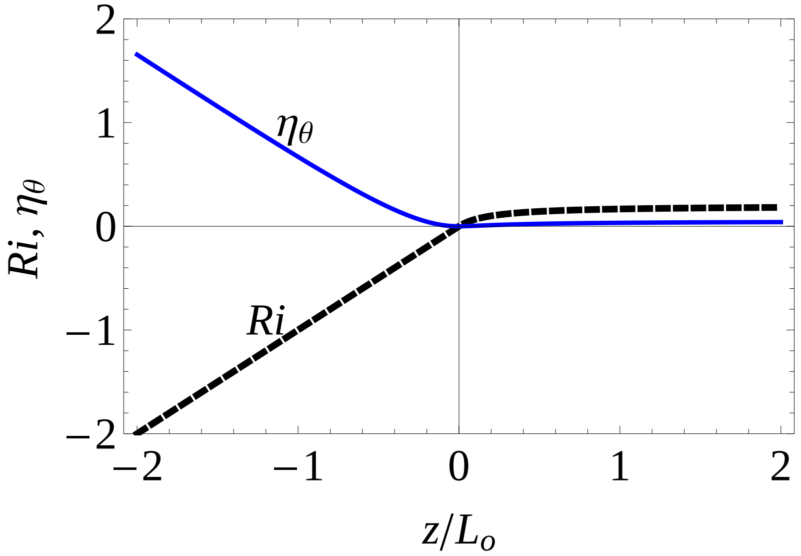

Figure 3.11: The model parameters; Ri, and η_θ, as functions of z/L_o, using empirical relationships from Kaimal and Finnigan [1994] and MOST.

and,

$$\frac{K_m}{K_h} = \begin{cases} (1+16|z/L_o|)^{-1/4}, & -2 \leq z/L_o \leq 0, \\ 1, & 0 \leq z/L_o \leq 1. \end{cases} \tag{3.106}$$

From the above relationships, $Ri \equiv Ri(z/L_0)$, for unstable ($z/L_0 < 0$), neutral ($z/L_0 = 0$), and stable ($z/L_0 > 0$) stratifications. So the η_θ parameter can be expressed from Equation 3.103, as

$$\begin{aligned} \eta_\theta &= \frac{Ri^2}{(K_m/K_h) - Ri} \\ &\equiv \eta_\theta(z/L_o). \end{aligned} \tag{3.107}$$

The parameters; Ri and η_θ are plotted against z/L_o in Figure 3.11. The MOST study and the data comparisons were performed by Businger et al. [1971].

The integrations in Equations 3.19, and 3.22 are performed by using two- and three-dimensional adaptive integration algorithms from the Risø Computer Library, and that the ‘fast and reliable method’ developed by Mann [1994a]. The numerics seemed to work with reasonable speed, where it takes ~ 18-19 seconds to get all the seven spectra and co-spectra, analysed above, for both; the required accuracy in the numerical integration of Equation 3.96 with $\Delta y = \Delta z = 0$, and the relative error in the numerical integration of the partial differential equations (Equations 3.51, and 3.52), is 0.0001.

Table 3.5: Performance of the model in variance and co-variance predictions at $z =$ 40 m. The model overestimation is denoted by '$+$' and underestimation by '$-$'.

Model	Stability	$\Delta\%$						
		u	v	w	uw	θ	$u\theta$	$w\theta$
New RDT	S	-11.5	-17.3	+18.8	+30.4	-24.5	-17.0	+51.6
	NNS	-8.2	-8.0	+21.7	+38.5	-59.0	-6.26	+18.7
	NNU	+9.6	-17.6	+19.6	+61.2	-66.7	-50.0	-10.3
	U	+21.2	-31.7	+31.0	+67.3	-54.4	-67.4	-32.8
M94	S	-5.0	-19.7	+11.7	+47.4			
	NNS	-4.0	-12.8	+7.0	+45.0			
	NNU	-8.0	-24.0	-4.5	+25.8			
	U	-3.7	-34.0	+1.6	+23.8			

In order to see the performance of the model, we adopt a similar method as given in Chapter 2, where we estimate variances and co-variances both from the measured time series and the model. Table 3.5 gives the relative model over/underestimation of the (co-)variances, which are estimated for the spectra shown above for S, NNS, NNU, and U stability cases. We also compare the results with those obtained from the spectral fits from the M94 model. The M94 parameters are shown in Table 3.6. The spectral fits from the M94 are shown in Figure 3.12 for stable and unstable ABL.

Table 3.6: The M94 model parameters from the fits for S, NNS, NNU, and U stability cases at the Høvsøre site for the velocity bin 8-9 m s^{-1}. The number of 30-minute time series n for each case are provided in Table 3.3. The measurements are taken from sonic anemometer located at $z = 40$ m.

Stability	$\alpha\varepsilon^{2/3}$ (m$^{4/3}$ s^{-2})	L (m)	Γ
S	0.05	12	3.1
NNS	0.053	21	3.4
NNU	0.04	45	3.7
U	0.04	75	3.5

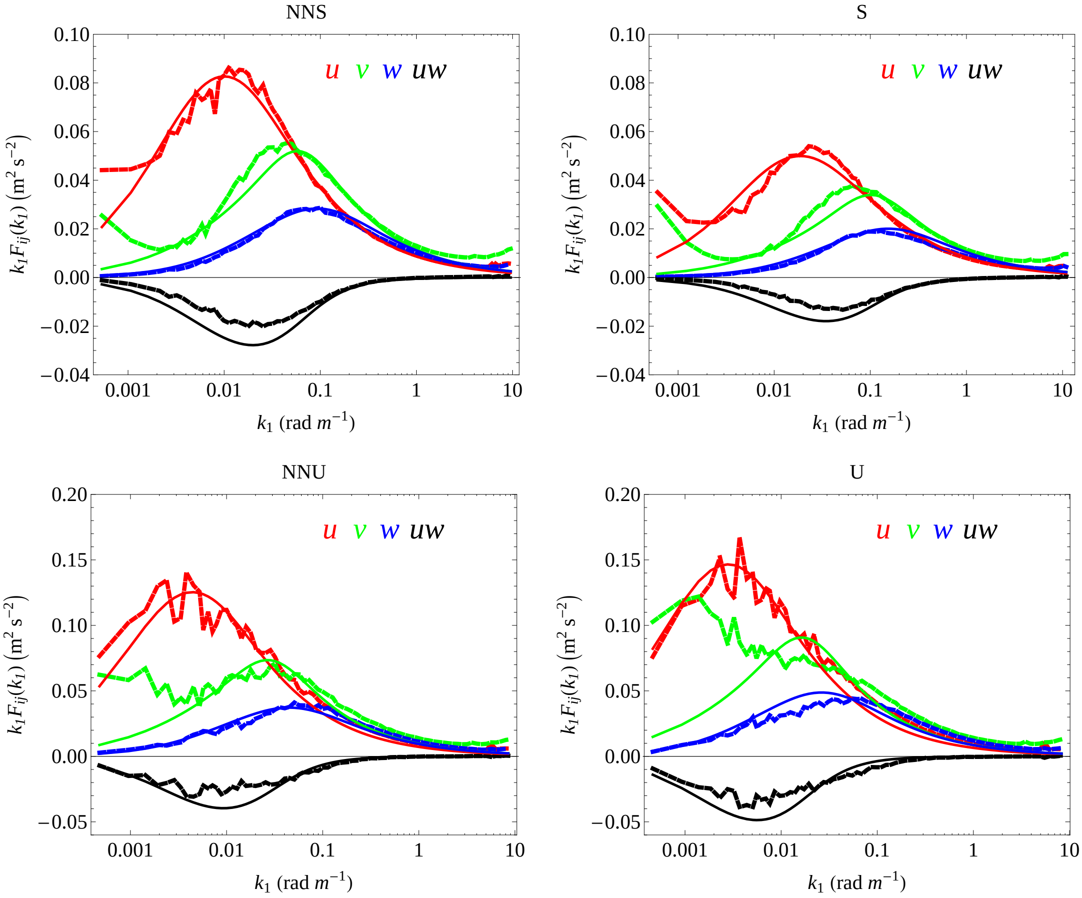

Figure 3.12: The M94 spectral fits (smooth lines) to the data (ragged lines), from Høvsøre at $z = 40$ m for NNS (top left), S (top right), NNU (bottom left), and U (bottom right). The model parameters are provided in Table 3.6.

The parameters in the model are obtained by rough-manual fitting of the model calculations to that from the measurements— the one-dimensional spectra and co-spectra, whereas we perform the χ^2-fits of the M94 model, which is described in Chapter 1 and 2. The reason that we do not perform χ^2-fits to the new model is because of the look-up table, which is required to build the χ^2-fit interpolation functions; in order to make a look-up table we should have an idea of the parameter ranges, especially Ri and η_θ. The look-up table requires many calculations; for example, from the derivation which we have proved in Equation 3.89, we fix $\alpha\varepsilon^{2/3} = L = 1$, and if we keep Ri as fitting parameter, it requires $(\Gamma =)l \times (Ri =)m \times (\eta_\theta =)n$ numbers of (seven) (co-) spectrum calculations, in which each calculation (for all seven (co-) spectrum) takes approximately 18 seconds.

The results which are presented in this chapter are preliminary results, otherwise, apart from that, the model seems to work well for stable ABL, whereas it performs worse for unstable ABL (by looking at the (co-) spectra figures). By looking at the NNU- and U- u-spectra, it is observed that there is a sharp increase in energy for $k_1 \leq 0.002$, which also affects uw, $u\theta$, and $w\theta$- co-spectra roughly below this wavenumber. In terms of Δ values, which are provided in Table 3.5, it is observed that the model performs slightly better for v and uw, both for S and NNS. The large errors in the θ-variance correspond to the noise in temperature spectra at higher frequencies, as well as mesoscale motions at lower frequencies.

The spectral fits are done with the understanding of the role of the parameters in modifying the (co-)spectra, and changing the values of the (co-)variances. For the stable cases, an increase in the Ri value results in shifting the peaks of velocity spectra slightly both to the right along the abscissa and downward (upwards for uw co-spectra) along the ordinate, and the u-spectra is more influenced than the v- and w-spectra (the influence on the v- and w-spectra in very slight). Also, the peaks of the θ-spectrum and $u\theta$ co-spectrum shift upwards, whereas the peak of $w\theta$ shifts downwards, with an increase in Ri, for stable cases. The effect of an increase in the value of η_θ, in stable case, is opposite to that of Ri, except that the peak of the θ-spectrum shifts upwards, similar to that with an increase in Ri, with a decrease in the temperature length scale. In unstable cases, an increase in the absolute value of Ri has similar effect on the $\theta, u\theta$, and $w\theta$ (co-)spectra as that in stable case, whereas the velocity spectra shift upwards and the uw co-spectrum shifts downwards towards lower wavenumber, while η_θ affects the spectra in similar manner to that Ri. The role of the other three parameters, namely $\alpha\varepsilon^{2/3}, L$, and Γ is described in Chapter 2. Also, the anisotropic nature of turbulence in terms of Γ is analysed in a very simple way by analysing the anisotropic tensor mapped in the palne of the principal invariants, called the Lumley triangle (see Appdx B for the description and the results).

The performance of the model in coherence predictions can be determined in terms of the G factor from Equation 2.11 in Chapter 2, which is the absolute area between the smooth and ragged curves in the coherence plots shown in Figure 3.9 for S, NNS, and NNU cases. We also compare the G values determined from the M94 model. It

Table 3.7: Model performance in terms of G factor in coherence predictions (Equation 2.11 in Chapter 2). The coherences are determined from the model and the measurements between heights $z_1 = 40$ and $z_2 = 60$ m. The model performance is compared with that of the M94 model.

		G	
Stability	coh	New RDT	M94
NNS	u	0.03	0.03
	v	0.08	0.10
	w	0.12	0.15
	θ	0.08	–
S	u	0.05	0.05
	v	0.14	0.11
	w	0.09	0.12
	θ	0.09	–
NNU	u	0.18	0.20
	v	0.37	0.43
	w	0.22	0.28
	θ	0.28	–

is observed from Table 3.7 that the new RDT model with the buoyancy effects gives similar performance in the coherence predictions. In terms of G values, the new model seems to work slightly better for NNU, despite the poor spectral fits.

The power law in the inertial sub-range, where the velocity-temperature co-spectra are proportional to $k_1^{-7/3}$, is shown in Figure 3.13. It can be observed that in stable cases, the sub-inertial range exists over a band of k_1, narrower than in unstable cases, while the model also able to predict the same— the energy cascade process in stable and unstable ABL. Also, the difference means that the unstable turbulence is more isotropic than that in stable case, and this can be seen from the anisotropy Γ parameter given in Table 3.3, where Γ for stable case is lager than that for unstable case. The Γ value for stable case, that obtained from the M94 model, is smaller than that for unstable, however. The unstable-$u\theta$ falls much faster with wavenumber than the measured co-spectrum, as observed from Figure 3.13 (right plot).

In the inertial sub-range, the life time of eddies are proportional to $k^{-2/3}$ and the assumption in the M94 model is, at scales larger than the intertial sub-range, eddy

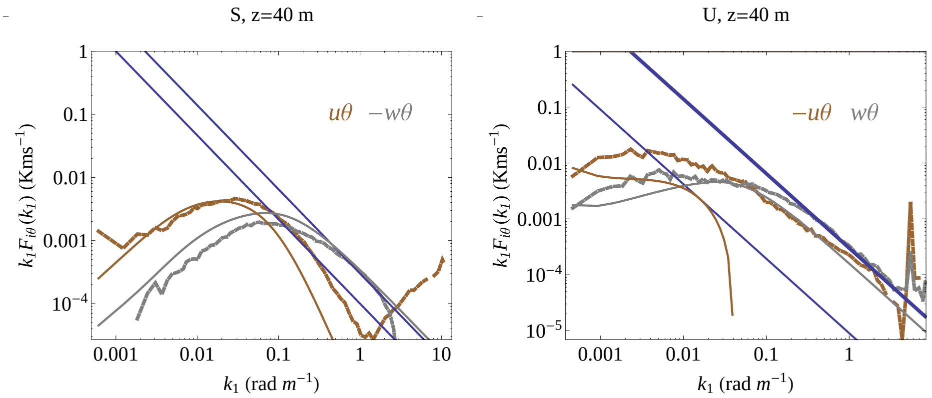

Figure 3.13: The inertial subrange: $F_{i\theta} \propto k_1^{-7/3}$, shown in log-log plot, for $i = 1$ and 3. Smooth lines represents the model co-spectra, whereas the measurements are shown by ragged lines. Straight lines in both the plots are proportional to $k_1^{-4/3}$. Note, for S $-w\theta$, while for U $-u\theta$ are shown in respective plots.

life time is proportional to k^{-1} divided by their characteristic velocity $(\int_k^\infty E(p)(p))^{1/2}$ such that, eddy life time in Equation 3.88 is proportional to $k^{-2/3}$ for $k \to \infty$ and k^{-1} for $k \to 0$. The alternative formulations for eddy life time, which are provided in Mann [1994a] and the references within, give different k-proportionalities for the scales larger than the inertial sub-range, such as, k^{-2} and $k^{-7/2}$ for $k \to 0$. The eddy life time from M94 may not be the only choice, and the use of alternative forms of eddy life time might be the future task. There is some difficulty in RDT modeling of unstable v-spectra at lower frequencies, which might be due to the eddy life time, the non-linear slow pressure term (second term in the right side of the Equation 3.40, which is excluded in RDT), and might be important at larger scales. Also, the presence of the ground, which has been ignored in the model but was incorporated in the US+B model of Mann (1994), could be important in explaining the large v-spectrum at low wavenumbers.

3.11 Conclusion and future work

The new RDT-based spectral tensor model is proposed, which, in addition to the velocity spectra and co-spectra, also gives the temperature spectrum and the temperature fluxes, as a result of including buoyancy effects via a mean uniform temperature gradient. The preliminary results presented in this study show that the model seems to work better for stable than unstable conditions. The model is able to predict well the length scales (corresponding to the peaks of (co-) spectra) of temperature spectrum and temperature-velocity co-spectra, where the length scale of $u\theta$ is roughly equal to that of u-spectra, and the length scales of θ and $w\theta$ are roughly equal to that of w-spectra, in both stable and unstable ABLs. In the intertial subrange, $w\theta$ co-spectrum is proportional to $k_1^{-7/3}$. The model overestimates energy in the u-spectrum at larger spatial scales in unstable stratification, and a relatively large underestimation of the $u\theta$ co-variance is noted. The model is able to predict the θ-coherence, while the prediction is better in stable cases, than in unstable cases. We compare the model predictions against the M94 model predictions in the coherence estimations, where the new model seems to give slightly improved results. The cross-spectral phase results show that the θ-phase lies between the v- and u-phase, whereas the model shows $\varphi_\theta \approx \varphi_v$.

The model in its present state needs to be improved in many ways; e.g. it can be tested against alternative forms of eddy life time. Also the two extra parameters Ri and η_θ are obtained from spectral fits, while the model will be tested against the Ri values determined from the measurements. The temperature spectra from the Høvsøre measurements are noisy, and therefore, in the future we could use other measurements. We have not tested the model using the empirical relationships from the MOST as discussed in the Section 3.10, where the number of parameters is reduced to four instead of five, and that it could be useful to test RDT model against MOST within the surface layer. There is possibility of improving the spectral fits by making the look-up table and making the interpolations function, which will be done by many (co-)spectra calculations as discussed above on a computer cluster of DTU's Wind Energy department.

Appdx A

Journal of Turbulence
Vol. 13, No. 36, 2012, 1–13

Vertical cross-spectral phases in neutral atmospheric flow

A. Chougule[a]*, J. Mann[a], M. Kelly[a], J. Sun[b], D.H. Lenschow[b] and E.G. Patton[b]

[a] *DTU Wind Energy, Technical University of Denmark, Risø Campus, Roskilde, Denmark;* [b] *National Center for Atmospheric Research (NCAR), Boulder, Colorado, USA*

(*Received 11 April 2012; final version received 07 July 2012*)

The cross-spectral phases between velocity components at two heights are analyzed from observations at the Høvsøre test site and from the field experiments under the Cooperative Atmosphere-Surface Exchange Study in 1999. These phases represent the degree to which turbulence sensed at one height leads (or lags) in time the turbulence sensed at the other height. The phase angle of the cross-wind component is observed to be significantly greater than the phase for the along-wind component, which in turn is greater than the phase for the vertical component. The cross-wind and along-wind phases increase with stream-wise wavenumber and vertical separation distance, but there is no significant change in the phase angle of vertical velocity, which remains close to zero. The phases are also calculated using a rapid distortion theory model and large-eddy simulation. The results from the models show similar order in phasing, but the slopes of the phase curves are slightly different from the observations, especially for low wavenumbers.

Keywords: cross-spectra; phases; atmospheric turbulence; wavenumber; vertical distance

1. Introduction

The structure of atmospheric turbulence can be analyzed in terms of two-point statistics such as normalized cross spectra (also known as coherences), which are typically studied both experimentally and theoretically as a function of horizontal separation distance for homogeneous turbulence in the atmospheric surface layer [1, 2]. The coherences of the along-wind, cross-wind, and vertical velocity components (u, v, w) decrease with increasing separation distance, as seen from both observations and theory [2].

In this paper, we attempt to answer the research question, "how and why are the cross-spectral phases with a vertical separation different, for different velocity components in the neutral atmospheric boundary layer (ABL)?"

We investigate cross spectra with particular emphasis on the associated phases φ for vertical separations Δz, using observations at Høvsøre [3, 4] and from Cooperative Atmosphere-Surface Exchange Study in 1999 (CASES-99) [5, 6]. No investigation of the vertical phase angles for all three velocity components (i.e., φ_u, φ_v, and φ_w), including their behavior in the ABL, has been noted in the literature. Mann [2] studied φ_{vw} (the phase angle between v and w) for horizontal separations, and $\varphi_{uu}(\equiv \varphi_u)$ and φ_{uw} for vertical separations, where the w-component was measured further from the surface. Few experimental

---

*Corresponding author. Email: absch@dtu.dk

ISSN: 1468-5248 online only

http://dx.doi.org/10.1080/14685248.2012.711524
http://www.tandfonline.com

investigations have been done on the phases. Heidrick et al. [7] experimentally studied the phases of the axial velocity component in fully developed pipe flow using measurements taken at two different points, where the separation vector was oriented at different angles to the mean flow. Komori et al. [8] studied the phase angle between the vertical velocity component and the temperature in stably stratified open-channel flow. Both Heidrick et al. [7] and Komori et al. [8] assumed turbulent motions approach as wavelike motions. The Sandia (Veers) method [9], which is used in wind engineering for load calculations on wind turbines, assumes an average of zero phase between any two points because of an exponential form of the coherence function as given in Ref. [10]. The Mann method [11], based on the Mann spectral tensor model [2] and widely used in wind engineering, does give non-zero phases.

In addition to the observations, we also evaluate the phase angles from the Mann spectral tensor model [2], which incorporates rapid distortion theory (RDT) [12, 13], and from data generated by large-eddy simulation (LES) [14]. The phases are determined by calculating the two-point cross spectra of velocity components and corresponding spectra as defined in Section 1.2. The observations and the models used for the analysis are described in Section 2 and Section 3, respectively. The results from the observations and the models are given in Section 4. In Section 5, we discuss more details and the mechanism explaining the systematic behavior of the phases, followed by conclusions in Section 6.

1.1. *Motivation*

Mann [2] modeled the evolution of turbulence induced by uniform shear using RDT [12,13] in a neutral surface layer. Mann [11] used the model of [2] to develop a method to simulate the three-dimensional wind in the time domain. The model in [2] and the method in [11] are the industry standards for aeroelastic calculation of wind turbine loads [15]. Turbulence simulations from [11] show systematic behavior in u, v, and w fluctuations in the rotor plane of a horizontal axis wind turbine, and when used to predict the respective phase angles between two heights, we see that $\varphi_v > \varphi_u > \varphi_w$ for $k_1 \Delta z \leq 1$, where k_1 is a stream-wise wavenumber. We expect that this behavior in phasing is due to the vertical shear. In order to confirm that, we analyze observed and LES data in more detail.

Shear-induced turbulence may have an effect on wind turbine loading. Sathe et al. [4] showed that in the ABL under stably stratified conditions, where turbulence is suppressed, large wind gradients lead to increased fatigue loading on the turbine rotor. Due to the presence of the ground in situations where there is no flow reversal or flow separation, one expects that the wind approaches a given point (x, y, z) faster at heights farther from the ground than at smaller z (closer to the surface), and so the turbulence sensed at the higher point “leads” in time that sensed at the lower point for the same (x, y).

The sketch given in Figure 1 illustrates the deformation of an “eddy” by uniform shear. The eddy hits the turbine plane first at point **a**, then at **b**. With increasing wind turbine diameter, the bending moments due to the vertical shear become more prominent. The combination of fatigue loads on wind turbines, due both to wind shear and shear-induced turbulence – with its ability to induce significant coherent phase differences across the vertical extent of a turbine rotor – motivates investigation of the phases in more detail. However, the actual consequences for loads will not be investigated here.

1.2. *Definitions*

The phases are calculated from complex cross spectra. The cross spectrum between velocity components $u_i(t)$ $(i = 1, 2, 3)$ and $u_j(t)$ $(j = 1, 2, 3)$ at heights z_1 and z_2, respectively, is

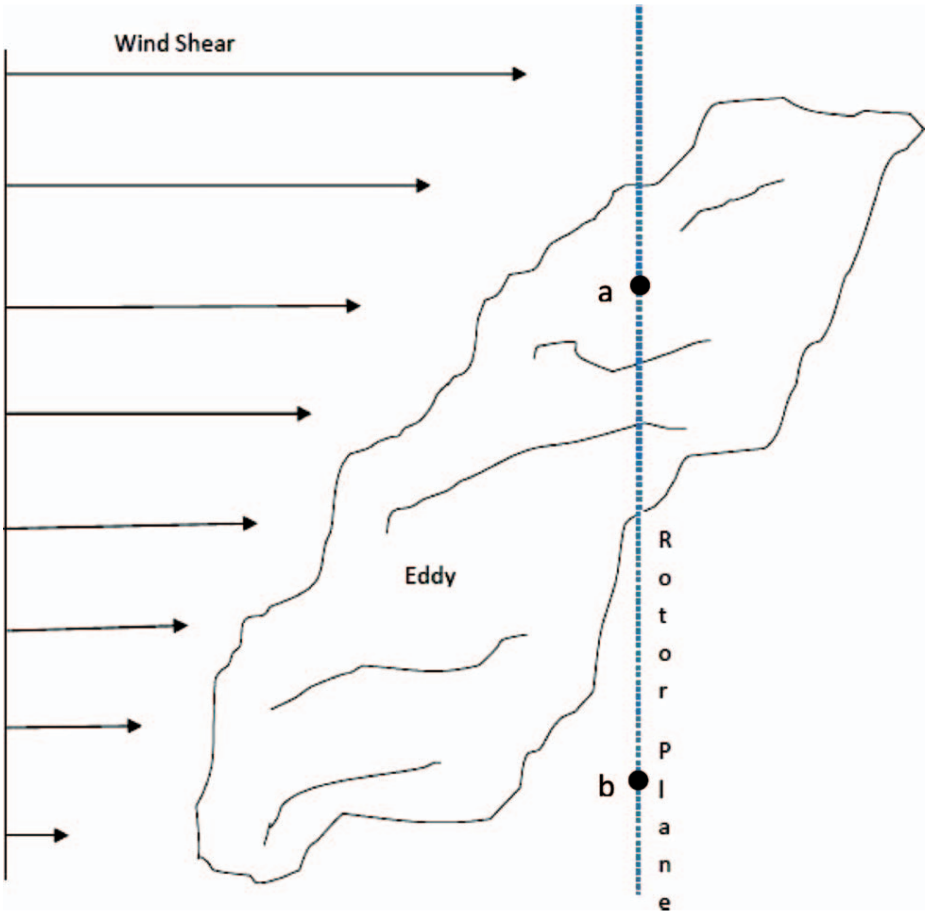

Figure 1. Sketch of the eddy stretching due to the shear. The turbulence sensed at point **a** leads in phase with respect to the turbulence sensed at point **b** in the rotor plane of a horizontal axis turbine.

defined as

$$\chi_{ij}(f, \Delta z) = \langle \hat{u}_i(f, z_1)\hat{u}_j^*(f, z_2)\rangle, \tag{1}$$

where f is frequency, $\Delta z = z_2 - z_1$, $\langle\ \rangle$ denotes ensemble averaging, $*$ denotes complex conjugate, and $\hat{u}_i(f, z_1)$ is the complex-valued Fourier transform of the ith velocity component $u_i(t)$ at height z_1. The phase between the two velocity components is then

$$\varphi_{ij}(f, \Delta z) = \arg(\chi_{ij}(f, \Delta z)). \tag{2}$$

The coherences known as "squared coherences" [16] are frequently used in wind engineering [17] and calculated from the cross spectra and the single-point power spectra [18] via

$$\mathrm{coh}_{ij}(f, \Delta z) = \frac{|\chi_{ij}(f, \Delta z)|^2}{F_i(f, z_1)F_j(f, z_2)}, \tag{3}$$

where $F_i(f, z) = \langle \hat{u}_i(f)\hat{u}_i^*(f)\rangle$ is the single-point power spectrum of the ith velocity component $u_i(t)$ at height z.

If we assume that Taylor's hypothesis of "frozen turbulence" is valid, then the measured time series can be related to spatial fluctuations. So for the stream-wise direction, single-point measurements can be related through $k_1 = 2\pi f/U$, where U is the stream-wise mean wind speed.

2. Observations

Two different datasets are used to investigate the vertical cross-spectral phases: the Høvsøre test site in Denmark and the CASES-99 field experiment. Both provide a unique opportunity to investigate the phase angles between wind components as a function of the vertical separation distance and the distance from the ground.

2.1. *Høvsøre*

The measurements are taken from the 116.5 m tall mast at the Høvsøre test site on the west coast of Denmark. Sonic anemometers, sampling at 20 Hz and measuring in three dimensions, are installed on the mast at heights of 10, 20, 40, 60, 80, and 100 m. The land to the east of the mast can be considered as flat, homogeneous terrain. On the west side of the mast, land extends 1500 m to the North Sea coast, including a dune which can affect the flow. Five wind turbines are situated to the north of the mast. More details about the location and instrumentation can be found in Refs. [3,4].

To avoid the effects from the wind turbine wakes and focus on flow over essentially uniform terrain, winds are selected from directions between 60° and 120°, and the data limited to when the 80 m mean wind speeds fall between 8 and 9 m s^{-1}. The calculations are done for data corresponding to neutral stability conditions, i.e., when the Obukhov length L_o measured at $z = 10$ m is $|L_o| \geq 500$ m. The height interval chosen in the phase analysis spans 40 –100 m. Analysis is done using seven years of data from 2004 to 2010.

2.2. *CASES-99*

The CASES-99 was conducted over relatively flat grassland near Leon, Kansas, US during October 1999. Mean and fluctuating wind components in three dimensions were sampled at 20 Hz from sonic anemometers at six levels on a 60 m scaffolding tower. Although data were collected throughout the diurnal cycle, CASES-99 was primarily focused on the stable, nocturnal boundary layer, including transition periods. Poulos et al. and Sun et al. [5,6,19] described the experiment and discussed some of the results. Here, we use the observations from 40 m and 55 m on the night of 17 October, which had the maximum nighttime wind; for this case, the mean wind averaged over these two heights was $\sim$12 m s^{-1} from the north and $|L_o| \geq 200$ m.

3. Modeling

Two different models are used to predict and analyze the phases in comparison with the observations: the Mann spectral velocity tensor model and National Center for Atmospheric Research's LES model.

3.1. *Spectral tensor model*

The Mann spectral velocity tensor model incorporates RDT [12,13] with an assumption of a mean uniform shear, plus a wavenumber-dependent eddy lifetime, to estimate the structure of turbulence over uniform flat terrain, which has been extended to cover gently varying orography [20]. The model calculates the evolution of turbulence in Fourier modes from an initial isotropic state, the energy spectrum of which is given by the von Kármán form [21].

The Mann model contains three adjustable parameters:

- A length scale L describing the size of energy-containing eddies.
- A non-dimensional anisotropy parameter Γ used in the parameterization of the eddy lifetime.
- A measure of the energy dissipation $\alpha\epsilon^{2/3}$, where the Kolmogorov constant $\alpha = 1.7$ and ϵ is the rate of viscous dissipation of specific turbulent kinetic energy.

The analytical form of the spectral velocity tensor in [2] is a function of these three parameters and can be expressed as $\Phi_{ij}(\boldsymbol{k}, L, \Gamma, \alpha\epsilon^{2/3})$, where $\boldsymbol{k} = (k_1, k_2, k_3)$ is the three-dimensional wave vector. The modeled cross spectra, which also become functions of the three parameters, are given as

$$\chi_{ij}(k_1, L, \Gamma, \alpha\epsilon^{2/3}, \Delta y, \Delta z) = \int \Phi_{ij}(\boldsymbol{k}, L, \Gamma, \alpha\epsilon^{2/3}) \exp(\mathrm{i}(k_2\Delta y + k_3\Delta z)) d\boldsymbol{k}_\perp, \tag{4}$$

where $\int d\boldsymbol{k}_\perp \equiv \int_{-\infty}^{\infty}\int_{-\infty}^{\infty} dk_2 dk_3$ and Δy is the transverse separation distance. The three parameters are determined by fitting model single-point power spectra $F_i(k_1, L, \Gamma, \alpha\epsilon^{2/3}) = \chi_{ii}(k_1, L, \Gamma, \alpha\epsilon^{2/3}, 0, 0)$ (no summation) to the measured single-point power spectra through chi-squared fitting as given in Ref. [2].

Figure 2 gives an example of a model fit of power spectra to the Høvsøre data at 100 m height illustrating extraction of L, Γ, and $\alpha\epsilon^{2/3}$. One hundred seventy-six 30 min time series are used to calculate spectra and co-spectra from the measurements. The three parameters are subsequently used as an input to calculate numerically the cross spectrum between any two velocity components through Equation (4). Thus, for vertical separations ($\Delta y = 0$), the model cross spectra and phases are expressed as $\chi_{ij}(k_1, L, \Gamma, \alpha\epsilon^{2/3}, \Delta z)$ and $\varphi_{ij}(k_1, L, \Gamma, \Delta z)$, respectively. The model phases are unaffected by ϵ.

The distortion of the wave vector due to shear dU/dz is given by $\boldsymbol{k}(t) = (k_1, k_2, k_{30} - k_1(dU/dz)t)$, with the initial wave vector $\boldsymbol{k}_0 = (k_1, k_2, k_{30})$. The model assumes a uniform shear, so dU/dz is constant with height, which is an approximation, but we do not expect that a non-zero d^2U/dz^2 would significantly alter the results. In addition to the uniform shear, the vertically inhomogeneous effect of blocking due to the surface (e.g., ground) was included in [2]; however, it does not produce significantly different results. Nevertheless, as discussed above, χ_{ij}, F_i, and φ_{ij} are functions of L that itself depends on the distance z from the ground. In this way, the model treats vertical inhomogeneity in application.

3.2. *LES model*

The pseudospectral LES code of Sullivan and Patton [14] simulates the ABL over flat, homogeneous terrain, with high temporal and spatial resolution. A database containing LES results from this code has been previously established, for different ABL states and surface conditions; here we use LES results for a neutral ABL, consisting of 1000 instantaneous volumes (snapshots) saved every two time steps. The domain size for the analyzed neutral case is $2400 \times 2400 \times 1000\,\mathrm{m}^3$, with horizontal resolution $\delta x = \delta y = 4\,\mathrm{m}$ and vertical resolution $\delta z = 2.5\,\mathrm{m}$. A geostrophic wind of $u_g = 5\,\mathrm{m\,s}^{-1}$ is imposed, and the time step, which is determined based on a CFL (due to Courant–Friedrichs–Lewy condition) number

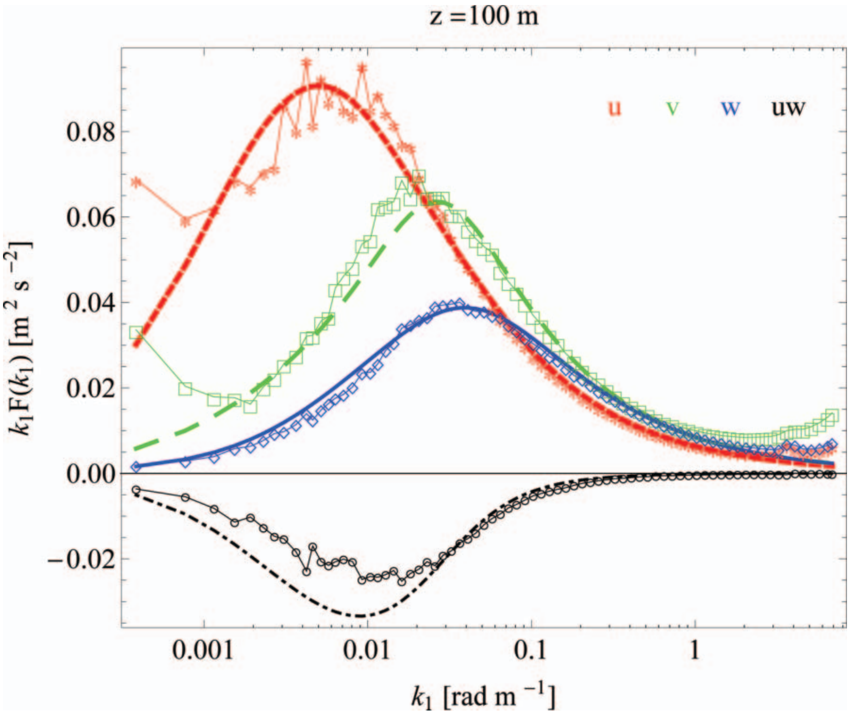

Figure 2. Example of the model fit of single-point spectra to the Høvsøre data at 100 m height to determine the three parameters in the Mann model [2]. One hundred seventy-six 30 min time series are used to calculate spectra from the measurements at Høvsøre. Measurements: u-spectrum; –∗–, v-spectrum; –□–, w-spectrum; –◇–, co-spectrum of u and w; –○–. Model spectra and co-spectrum: u; - - -, v; — — —, w; ——, uw; -··-.

of 0.75, is nearly constant at ∼0.7 s. The simulation meets the "high-accuracy zone" LES criteria established by Brasseur and Wei [22], with essentially resolution-independent results.

The surface is characterized by a roughness of $z_0 = 0.3$ cm and a virtual potential temperature of 300 K, with zero mean surface heat flux prescribed and the surface momentum fluxes dictated by z_0. A uniform virtual potential temperature is initially imposed up to the top of the boundary layer, which is capped by a virtual potential temperature inversion having $dT/dz = 0.003$ K m^{-1}. The boundary layer "top" can thus act dynamically and its structure varies, with a diagnosed mean boundary layer depth z_i of 616 m. The "snapshots" used for the analysis correspond to simulation times long after the initial "spin-up" of the code (∼1 h, much larger than the rough ABL timescale $\sim z_i/u_g$ [23] and larger than the large-eddy turnover timescale z_i/u_*, where u_* is the friction velocity). The (cross) spectra are calculated for each instantaneous snapshot in horizontal planes at two given heights and then averaged over all snapshots. Due to horizontal homogeneity, statistics are constant over the horizontal plane.

In the next section, the results from the observations and the models are provided, followed by discussion in Section 5.

4. Results

The phases from the Høvsøre observations are shown in Figure 3(a) and the coherences in Figure 3(b), along with the predictions from the Mann model. As described in Section 3.1, the three adjustable parameters in the model are determined by fitting the one-dimensional power spectra of the model to that from the data at heights 40 and 100 m (see Figure 2).

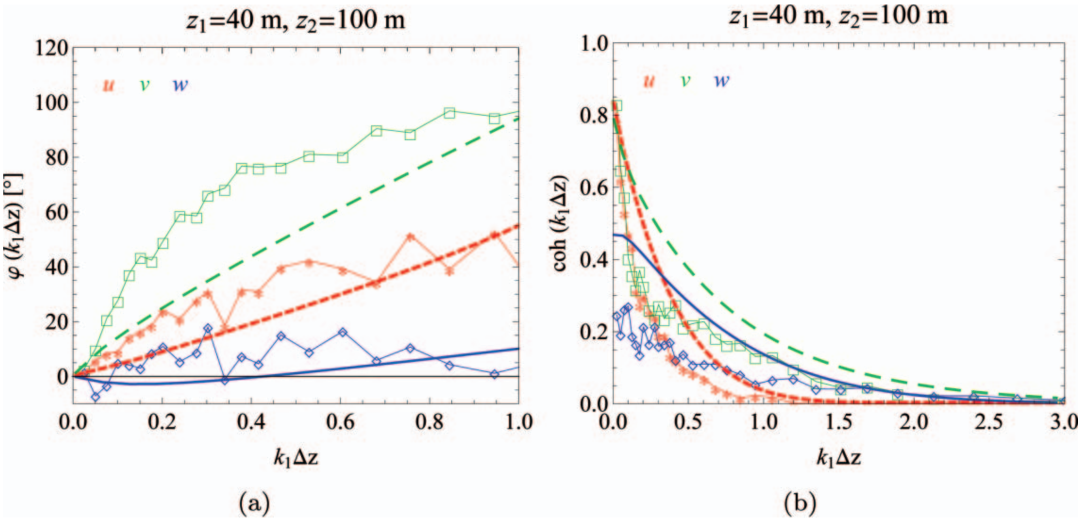

(a) (b)

Figure 3. The phases (a) and the coherences (b) between 40 m and 100 m at Høvsøre for a neutral ABL with the predictions from the Mann model [2]. Phase angles from the measurements: φ_u; –∗–, φ_v; –☐–, φ_w; –◇–. Model phases: φ_u; - - -, φ_v; – – –, φ_w; ——. Similar notations are followed for the coherences.

The average of the parameters at the two heights is used to calculate the model cross spectra. The slopes of the phase curves predicted by the model are different than those calculated from the measurements. However, the model is able to predict the order in phasing, $\varphi_v > \varphi_u > \varphi_w$, for $k_1 \Delta z \leq 1$.

The model overestimates the u-, v-, and w-coherence for $k_1 \Delta z \leq 1$. So at a given length scale, the fluctuations at two corresponding heights in the modeled coherent eddies are more correlated than those from the observation. It is also observed that the modeled phases are smaller than the phase angles from the measurements.

The phase angles from the CASES-99 are shown in Figure 4(a) between heights 40 and 55 m, along with the predictions from the Mann model. The Mann parameters are determined in the same way as described for the Høvsøre case. The same order in phasing

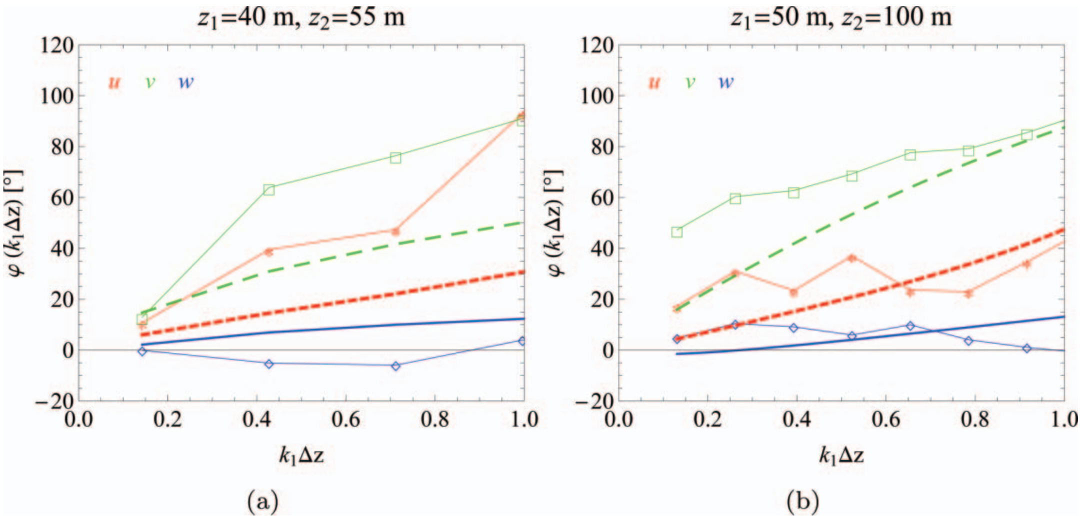

(a) (b)

Figure 4. A comparison of phases from (a) CASES-99 and (b) LES for a neutral ABL with the phases from the Mann uniform shear model. Mann model: φ_u; - - -, φ_v; – – –, φ_w; ——. CASES-99 and LES: φ_u; –∗–, φ_v; –☐–, φ_w; –◇–.

Table 1. The three parameters in the Mann model obtained from single-point power spectra from Høvsøre, CASES-99, and LES data, via chi-squared fits [2]. The averages of the parameters obtained at given heights z_1 and z_2 are provided. Refer to Figure 2 for an example.

Data	z_1 [m]	z_2 [m]	Γ	L [m]	$\alpha\epsilon^{2/3}$ [m$^{4/3}$s^{-2}]
Høvsøre	40	100	3.3	40	0.044
CASES-99	40	55	3.5	85	0.008
LES	50	100	2.9	52	0.028

is seen in the CASES-99. The phase φ_w is close to zero, which can also be seen at Høvsøre. The Mann model underestimates φ_u and φ_v, as compared to the observations at both sites.

Figure 4(b) shows the phases between heights 50 and 100 m from the LES of a neutral ABL. The LES spectra are fitted with the Mann model and the model parameters are obtained to predict the phases. We also observe $\varphi_v > \varphi_u > \varphi_w$.

The three adjustable parameters in the Mann model obtained from the Høvsøre, CASES-99 and LES are provided in Table 1.

5. Discussion

In this section, we describe some more details about the behavior of the phases. As we have seen in Section 4, RDT is capable of explaining the fact that $\varphi_v > \varphi_u > \varphi_w$. However, it is not entirely clear why this ordering is inevitable. In this section, the inequality is supported with simple physical and geometrical arguments.

Thirty-minute time series are used for the analysis of the Høvsøre data. For the neutral ABL, we obtain an ensemble of $n = 176$ realizations. As per the definition of the ensemble average, we require an infinite number of realizations in order to obtain (cross) spectra as defined in Section 1.2. So, due to the limited n, there is uncertainty in the estimated (cross) spectra and hence in the corresponding coherences and phases. Kristensen and Kirkegaard [24] showed that the estimated coherence is systematically overestimated. Letting the true coherence to be denoted as coh, the estimated coherence $\langle \mathrm{coh}_n \rangle$ is given due to [24] by

$$\langle \mathrm{coh}_n \rangle = \alpha_1 \tag{5}$$

with

$$\alpha_1 = 1 - \frac{n-1}{n}(1-\mathrm{coh})^n {}_2F_1(n, n; n+1; \mathrm{coh}), \tag{6}$$

where ${}_2F_1$ is the hypergeometric function. We see that n is large enough to give almost insignificant overestimation of the coherences. For example, for $n = 176$ we get $\langle \mathrm{coh}_{176} \rangle = 0.5014$ for coh $= 0.5$ and $\langle \mathrm{coh}_{176} \rangle = 0.0155$ for coh $= 0.01$ from Equations (5) and (6).

For winds from the west (i.e., from the North Sea), the flow is essentially inhomogeneous, so we might expect the phase angles to be different. But, quite surprisingly, when we examine the phase angles for winds selected between 240° and 300°, we find the same difference and ordering of the phases with slightly greater values. Also when we analyze the data for combinations of heights other than 40 and 100 m, we observe three things: first, with increasing Δz, both φ_u and φ_v increase for $k_1 \leq 0.01$, with no significant change in φ_w;

second, for a given Δz, moving further from the surface we see a slight decrease in φ_u and φ_v but no systematic effect upon φ_w; and third, we still get the same order in phasing, i.e., $\varphi_v > \varphi_u > \varphi_w$ (irrespective of the values of z_1 and z_2, as long as the coherence is non-zero). When we analyze the phases for mean wind speed intervals greater than 8–9 m s^{-1} (corresponding to 80 m height), the phases are insignificantly affected, with the same difference and ordering. In addition to the phases being almost unaffected by the mean wind speed, they show the same trend as in the two cases described above. In this regard, if we observe Figures 3(a) and 4(a), the phases from CASES-99 are smaller than those from Høvsøre (as is Δz).

Sathe et al. [4] showed the variation of the three parameters specifying the spectra as a function of mean wind speed at different atmospheric stabilities. For the neutral case, there is no significant variation in L or Γ with the mean wind speed between 3 and 16 m s^{-1}, but the $\alpha\epsilon^{2/3}$ parameter varies significantly as expected. Interestingly, as we discussed in Section 3.1, the model phases are functions of L and Γ but not $\alpha\epsilon^{2/3}$. With increasing Γ, which represents the degree of turbulence anisotropy, phase angles of all three velocity components increase and the phase curves shift upward. From Ref. [4], for the variations of L and Γ with mean wind speed, the standard deviations are ~ 5.2 m and ~ 0.11, respectively, which has no appreciable effect upon the model phases. This aspect of the model prediction is also consistent with the fact that the phases at Høvsøre are not dependent on the mean wind speed over the intervals described in the previous paragraph. In this regard, if we observe Figures 3(a) and 4(b), we see that the LES phases compare well with those from Høvsøre, although the average of the mean wind speeds at 50 and 100 m in the LES is $\sim$4 m s^{-1}. The vertical variation of the three parameters is described in Ref. [25].

As observed from the results in Section 4, modeled φ_u and φ_v are smaller than those from the measurements; we do not know the exact reason for this, but it could be due to inhomogeneity and as discussed in Section 3.1, the L parameter roughly follows z but does not strictly represent z.

The LES results shown here are based on spatial calculations. When the phases are calculated using simulated time series (i.e., in time-frequency domain) and using Taylor's hypothesis, we obtain a different result, as shown in Figure 5. We do not know the precise reason behind this, but what is noticeable from Figure 5 is that the temporal-u-phase is systematically smaller than the spatial-u-phase and the temporal-v-phase is greater than the

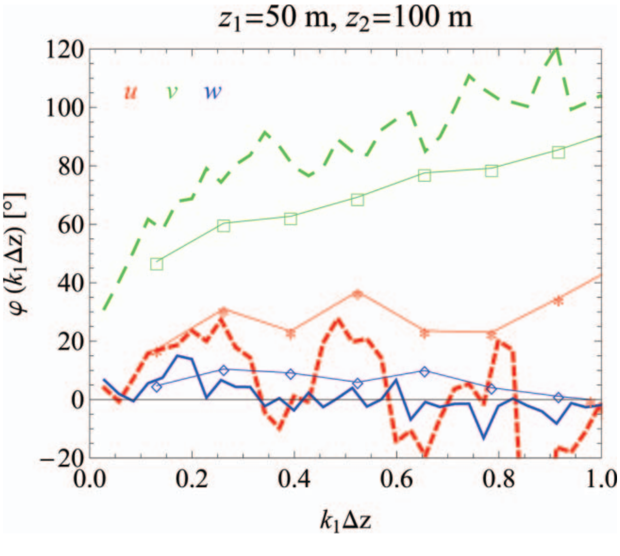

Figure 5. The LES phases based on time- and space-domain calculations. The temporal phases: φ_u; - - -, φ_v; — — —, φ_w;——. The spatial phases: φ_u; –∗–, φ_v; –□–, φ_w; –◇–.

spatial-v-phase. The differences between the time- and space-domain calculations likely result from the limited domain size, applicability of Taylor's hypothesis, and the effect of the LES code zeroing the mean vertical velocity over the horizontal plane at each height and time step. In this connection, we suggest that two pulsed lidars mounted at two different heights on a meteorological mast, staring upwind and measuring at many range gates simultaneously, could shed light on the differences between the temporal and spatial spectral phases. Several such lidars have been deployed in the field [26] but not in this configuration.

5.1. *Mechanism*

The three-dimensional velocity field $\boldsymbol{u}(\boldsymbol{x})$ is decomposed into Fourier modes, so the entire field can be written as a sum (or more precisely an integral) of terms of the form $\boldsymbol{u}(\boldsymbol{k})\exp(-i\boldsymbol{k}\cdot\boldsymbol{x})$, where $\boldsymbol{u}(\boldsymbol{k})$ is a complex vector, the Fourier amplitude. According to Equation (4), all three-dimensional Fourier modes $\boldsymbol{u}(\boldsymbol{k})$ with a particular value of k_1 contribute to the cross spectrum at that one-dimensional wavenumber. In the following, we consider qualitatively all these contributions to the cross spectrum and how they change under the action of a shear dU/dz.

Because of incompressibility, $\nabla\cdot\boldsymbol{u}(\boldsymbol{x}) = 0$, the velocity amplitudes are perpendicular to the wave vectors: $\boldsymbol{k}\cdot\boldsymbol{u}(\boldsymbol{k}) = 0$. Furthermore, since the Fourier amplitude of the vorticity $\boldsymbol{\omega}(\boldsymbol{k}) = -i\boldsymbol{k}\times\boldsymbol{u}(\boldsymbol{k})$, then $\boldsymbol{k}$, $\boldsymbol{u}(\boldsymbol{k})$, and $\boldsymbol{\omega}(\boldsymbol{k})$ are mutually perpendicular. In RDT, the vorticity equation is

$$\frac{D}{Dt}\boldsymbol{\omega}(\boldsymbol{k}) = \boldsymbol{\omega}(\boldsymbol{k})\cdot\nabla\boldsymbol{u}(\boldsymbol{k}), \tag{7}$$

where $\boldsymbol{k}(t) = (k_1, k_2, k_{30} - k_1(dU/dz)t)$ as mentioned in Section 3.1.

In Figure 6, Fourier modes are illustrated, with wavefronts in the vertical x–z plane for some lagging, leading, and normal modes before and after shearing (Figures 6(a) and 6(d), respectively). The corresponding wave vectors are shown in Figures 6(b) and 6(e). All modes shown have a fixed horizontal wavenumber k_1, but for some the fluctuations lead at height z_2 relative to z_1, some have approximately zero phase difference, while for others they lag. The corresponding vorticity $\boldsymbol{\omega}(\boldsymbol{k})$ perpendicular to $\boldsymbol{k}$ is shown in Figures 6(c) and 6(f). In isotropic turbulence, leading and lagging modes are equally energetic, so the resulting phase is zero. Introducing a linear shear as in [2] changes this situation. Here, RDT (Equation (7)) predicts that modes with vorticity roughly aligned with the principal axis of strain become more energetic, while modes with vorticity aligned with the principal axis of compression are suppressed. The consequences for the phase are illustrated by looking at lagging, neutral, and leading modes corresponding, respectively, to red, green, and blue in Figure 6.

For the u-component, the zero phase mode would typically have the most energy $\langle|\boldsymbol{u}(\boldsymbol{k})|^2\rangle$ due to the shape of the energy spectrum, because $k \equiv |\boldsymbol{k}|$ is smallest for all Fourier modes contributing to the cross spectrum with horizontal wavenumber k_1; but the energy in the u-component is zero because $\boldsymbol{u}(\boldsymbol{k})$ is perpendicular to $\boldsymbol{k}$. After some time, the shear will tilt $\boldsymbol{u}(\boldsymbol{k})$ (if it has a vertical component) and some energy will be transferred to the u-component, introducing a leading phase. The phase-lagging mode provides the most energy to the u-component, when $\boldsymbol{u}(\boldsymbol{k})$ is in the x–z plane (in the plane of the figure). That implies that the vorticity $\boldsymbol{\omega}(\boldsymbol{k})$ is mainly perpendicular to the paper plane, which implies that the mode is neither suppressed nor enhanced, since there is no vortex stretching. The

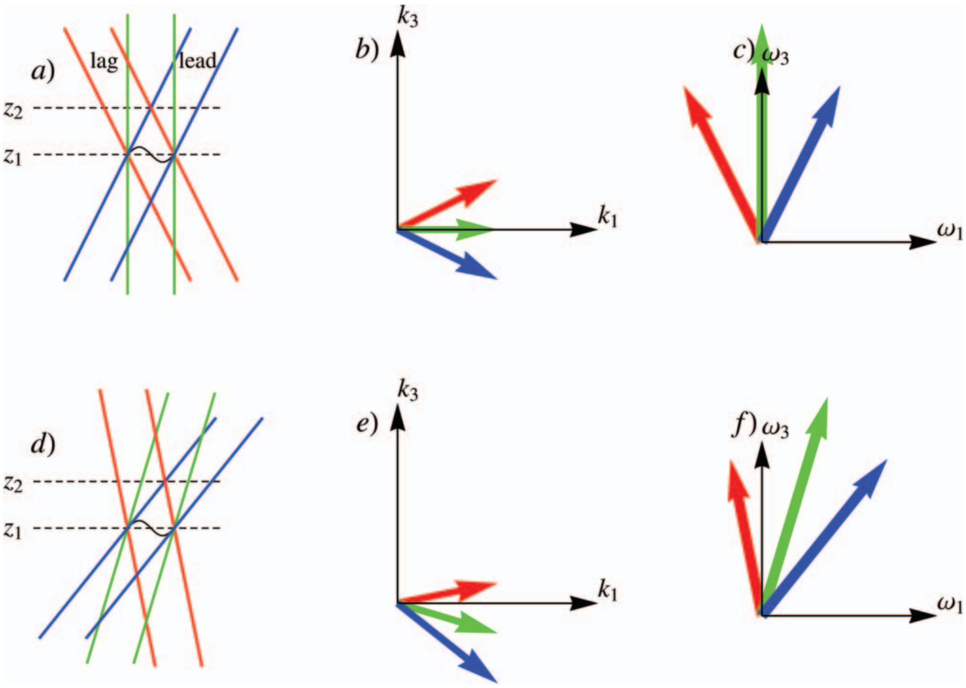

Figure 6. Fourier modes before (*a–c*) and after (*d–f*) being subjected to uniform shear. Physical space modes are shown in *a* and *d*, the corresponding wave vectors in *b* and *e*, and the vorticity Fourier amplitudes in *c* and *f*, provided that the velocity vectors are perpendicular to the paper plane. The red colors correspond to Fourier modes where the fluctuations at the height z_2 lag those at z_1, for green the modes are more or less in phase, and for blue the fluctuations lead at z_2.

same could be said about the leading mode, and we conclude that only because the most energetic modes are tilted forward, we expect a slightly leading phase of the u-component.

Modes with a lot of v energy have $\boldsymbol{u}(\boldsymbol{k})$ pointing mainly perpendicular to the paper plane. That implies that $\boldsymbol{\omega}(\boldsymbol{k})$ will be roughly aligned with the plane. For the mode with lagging phase (red, in Figure 6), the vorticity is then compressed leading to reduced energy, conversely for the leading modes. Here, the vorticity is stretched implying amplified fluctuations and the zero phase is also tilting as in the u-component case discussed above. In conclusion, distortion by the mean shear and tilting both enhance leading modes.

The zero phase mode has a lot of w-energy, but the vorticity is mainly perpendicular to the paper plane, so no amplification occurs. As $\boldsymbol{u}(\boldsymbol{k})$ tilts forward, energy is transferred away from the w-component and into the u-component, so phase shifting for w is suppressed. For the leading mode, which is blue in Figure 6, vorticity is still mainly perpendicular to the paper plane, so no amplification, but w will decrease because of the tilting of $\boldsymbol{u}(\boldsymbol{k})$. For the lagging phase, the tilting increases w at the expense of u. Summing up the various contributions, we must conclude that the w-phase must be very small or even negative.

With these qualitative arguments, one can intuitively deduce the inequality $\varphi_v > \varphi_u > \varphi_w$.

6. Conclusions

The main goal of this study is to understand how and why the vertical cross-spectral phases in the neutral ABL behave as observed. Phases of the cross spectra of all three velocity components show systematic behavior: $\varphi_v > \varphi_u > \varphi_w$ for $k_1 \Delta z \leq 1$. φ_u and φ_v tend to increase with $k_1 \Delta z$, but φ_w remains close to zero. We expect that this behavior is due to the vertical shear, and we show that this is consistent with simple physical and geometrical arguments. RDT and LES both predict the observed phase ordering.

Acknowledgments

This study is a part of the Ph.D. project funded by Siemens Wind Power A/S and WindScanner.dk, which is funded by the Danish Agency for Science. We are also obliged to the COMWIND project funded by Danish Council of Strategic Research (DSF-contract: 09-067216). The National Center for Atmospheric Research is sponsored by the National Science Foundation.

References

[1] C. Tong and J.C. Wyngaard, *Two-point coherence in the atmospheric surface layer*, Bound.-Layer Meteorol. 81 (1996), pp. 105–121.
[2] J. Mann, *The spatial structure of neutral atmospheric surface-layer turbulence*, J. Fluid Mech. 273 (1994), pp. 141–168.
[3] A. Sathe, J. Mann, J. Gottschall, and M.S. Courtney, *Can wind lidars measure turbulence?* J. Atmos. Ocean. Tech. 28(7) (2011), pp. 853–868.
[4] A. Sathe, J. Mann, T. Barlas, W.A.A.M. Bierbooms, and G.J.W. van Bussel, *Influence of atmospheric stability on wind turbine loads*, preprint (2012), Wind Energy, DOI: dx.doi.org/10.1002/we.1528.
[5] G.S. Poulos, W. Blumen, D.C. Fritts, J.K. Lundquist, J. Sun, S.P. Burns, C. Nappo, R. Banta, R. Newsom, J. Cuxart, E. Terradellas, B. Balsley, and M. Jensen, *CASES-99: A comprehensive investigation of the stable nocturnal boundary layer*, Bull. Am. Meteorol. Soc. 83 (2002), pp. 555–581.
[6] J. Sun, S.P. Burns, D.H. Lenschow, R. Banta, R. Newsom, R. Coulter, S. Fraiser, C. Nappo, J. Cuxart, W. Blumen, X. Lee, and X.Z. Hu, *Intermittent turbulence associated with a density current Passage in the stable boundary layer*, Bound.-Layer Meteorol. 105 (2002), pp. 199–219.
[7] T.R. Heidrick, S. Banerjee, and R.S. Azad, *Experiments on the structure of turbulence in fully developed pipe flow: Interpretation of the measurements by a wave model*, J. Fluid Mech. 81 (1977), pp. 137–154.
[8] S. Komori, H. Ueda, F. Ogino, and T. Mizushina, *Turbulence structure in stably stratified open-channel flow*, J. Fluid Mech. 130 (1983), pp. 13–26.
[9] P.S. Veers, *Three-dimensional wind simulation*, Tech. Rep. SAND88-0152, Sandia National Laboratories, 1988.
[10] P.S. Veers, *Modeling stochastic wind loads on vertical axis wind turbines*, Tech. Rep. SAND88-1909, Sandia National Laboratories, 1984.
[11] J. Mann, *Wind field simulation*, Prob. Eng. Mech. 13(4) (1998), pp. 269–282.
[12] S.B. Pope, *Turbulent Flows*, Cambridge University Press, UK, 2000.
[13] A.A. Townsend, *The Structure of Turbulent Shear Flow*, 2nd ed., Cambridge University Press, UK, 1976.
[14] P.P. Sullivan and E.G. Patton, *The effect of mesh resolution on convective boundary layer statistics and structures generated by large-eddy simulation*, J. Atmos. Sci. 68 (2011), pp. 2395–2415.
[15] IEC, *Wind turbines Part 1: Design Requirements*, IEC 61400-1, International Electrotechnical Commission, Geneva, Switzerland, 2005.
[16] J.S. Bendat and A.G. Piersol, *Random Data: Analysis and Measurement Procedures*, 2nd ed., Wiley, New York, 1986.
[17] C. Dyrbye and S.O. Hansen, *Wind Loads on Structures*, Wiley, West Sussex, 1997.
[18] J.C. Wyngaard, *Turbulence in the Atmosphere*, Cambridge University Press, UK, 2010.
[19] J. Sun, D.H. Lenschow, S.P. Burns, R.M. Banta, R.K. Newsom, R. Coulter, S. Frasier, T. Ince, C. Nappo, B.B. Balsley, M. Jensen, L. Mahrt, D. Miller, and B.S. kelly, *Atmospheric disturbances that generate intermittent turbulence in nocturnal boundary layers*, Bound.-Layer Meteorol. 110 (2004), pp. 255–279.
[20] J. Mann, *The spectral velocity tensor in moderately complex terrain*, J. Wind Eng. Ind. Aerod. 88 (2000), pp. 153–169.

[21] T. von Kármán, *Progress in the statistical theory of turbulence*, Proc. Natl. Acad. Sci. 34 (1948), pp. 530–539.

[22] J.G. Brasseur and T. Wei, *Designing large eddy simulation of the turbulent boundary layer to capture law-of-the-wall scaling*, Phys. Fluids 22 (2010), pp. 1–21.

[23] E.G. Patton, R.H. Shaw, M.J. Judd, and M.R. Raupach, *Large-eddy simulation of windbreak flow*, Bound.-Layer Meteorol. 87 (1998), pp. 275–306.

[24] L. Kristensen and P. Kirkegaard, *Sampling problems with spectral coherence*, Risø Rep. Risø-R-526, 1986.

[25] A. Peña, S. Gryning, and J. Mann, *On the length-scale of the wind profile*, Q. J. R. Meteorol. Soc. 136 (2010), pp. 2119–2131.

[26] J. Mann, J.P. Cariou, M.S. Courtney, R. Parmentier, T. Mikkelsen, R. Wagner, P. Lindelöw, M. Sjöholm, and K. Enevoldsen, *Comparison of 3D turbulence measurements using three staring wind lidars and a sonic anemometer*, Meteorol. Z. 18 (2009), pp. 135–140.

Appdx B

The anisotropy (stress) tensor resulting from the M94 model and calculations from NCAR's LES (c.f. Appdx A, Section 3.2) is analyzed. The anisotropy tensor is defined as

$$b_{ij} = \frac{R_{ij}(0)}{2K} - \frac{1}{3}\delta_{ij}, \tag{108}$$

where $K = \frac{1}{2}R_{ii}(0)$ and $R_{ij}(0) = \langle u'_i u'_j \rangle$ (See Equations 3.20 and 3.19). From Equation 108, the anisotropy tensor has zero trace, i.e. $b_{ii} = 0$. Since R_{ij} is a symmetric second order tensor so is b_{ij}, with the three principal invariants given by

$$\begin{aligned} \mathrm{I}_b &= b_{ii}(=0), & (109)\\ \mathrm{II}_b &= \frac{1}{2}b_{ij}b_{ji}, & (110)\\ \mathrm{III}_b &= \det(\mathbf{b}). & (111) \end{aligned}$$

It is also convenient to define two variables, p and q as (Pope [2000])

$$\begin{aligned} 6p^3 &= 3\mathrm{III}_b = b_{ij}b_{jk}b_{ki}, & (112)\\ 6q^2 &= -2\mathrm{II}_b = b_{ij}b_{ji}. & (113) \end{aligned}$$

The matrix $\mathbf{b}$ can also be transformed into principal axes with eigen-values λ_1, λ_2 and λ_3, where off-diagonal terms become zero, i.e. $b_{ii} = \lambda_1 + \lambda_2 + \lambda_3 = 0$. So, using $\lambda_3 = -(\lambda_1 + \lambda_2)$ and from Equations 110–113, we get

$$\begin{aligned} p^3 &= -\frac{1}{2}\lambda_1\lambda_2(\lambda_1 + \lambda_2), & (114)\\ q^2 &= \frac{1}{3}(\lambda_1^2 + \lambda_1\lambda_2 + \lambda_2^2). & (115) \end{aligned}$$

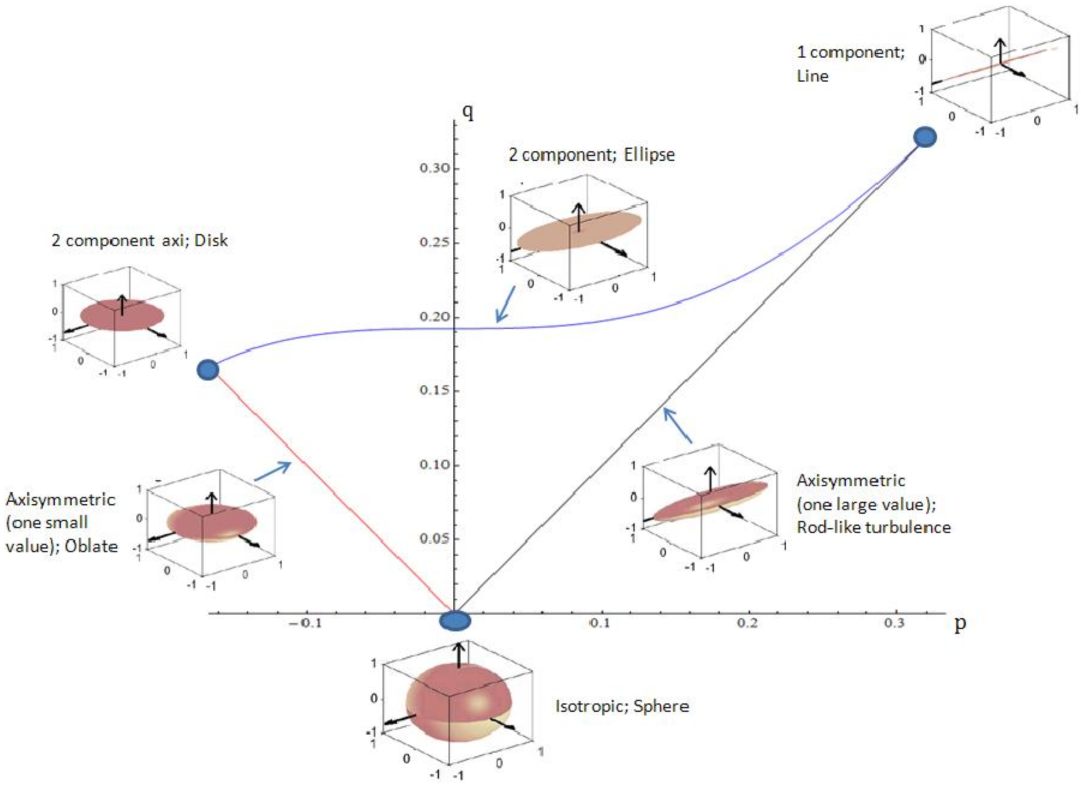

Figure 14: Lumley triangle with axisymmetric limits showing different ellipsoid shapes formed by different states of the Reynolds stress tensor. Source: A. J. Simonsen and P.-Å. Krogstad, *Turbulent Stress Invariant Analysis: Clarification of Existing Terminology*.

In summary, given the Reynolds stress tensor, p and q are calculated from either Equations 112–113 or 114–115. For M94, b_{ij} is calculated numerically (as discussed in Chapter 3). From the definition given in Equation 3.19 and relationship in Equation 2.7, in its normalized form, b_{ij} becomes only function of the Γ parameter, and the state of the anisotropy tensor can be represented in a p-q plane with varying Γ (between 0 to 4, say).

At any time and point in turbulent flow, the state of Reynolds stress tensor can be presented as point in the p-q plane. There are some special states of Reynolds stress tensor that correspond to particular points and curves in this plane, called the Lumley triangle (Pope [2000]) and shown in Figure 14.

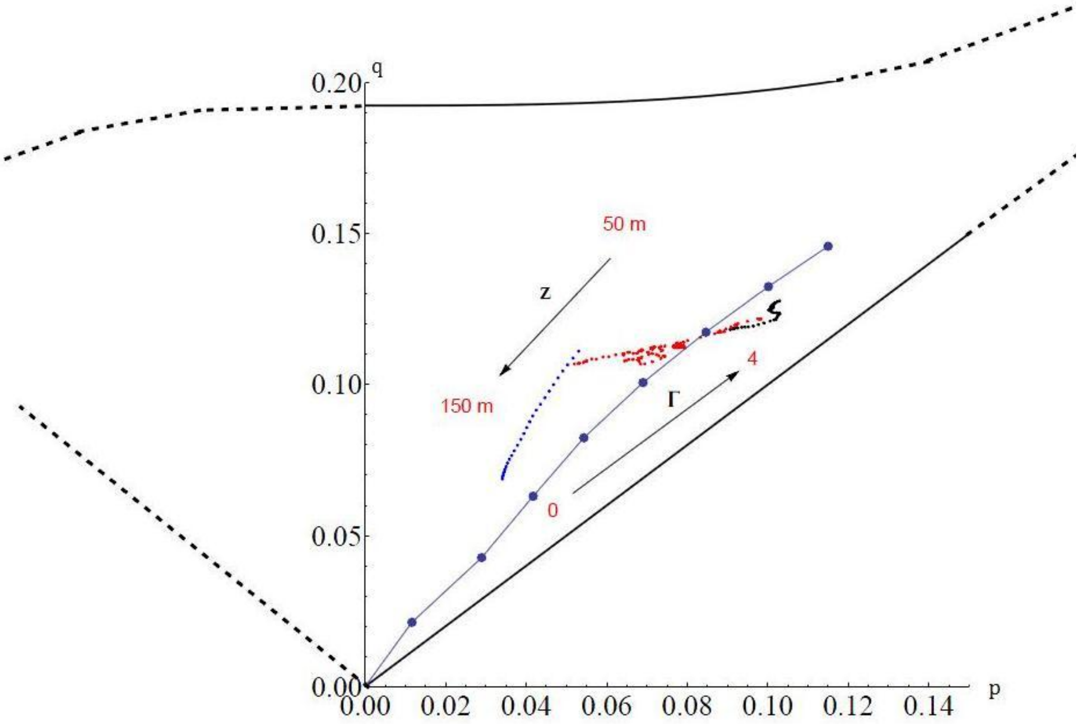

Figure 15: Anisotropy invariants calculated from the M94 model and NCAR's LES. Black points, Neutral; Red points, Stable; Blue points, unstable; M94, –●– (Direction of arrows indicates increase of height z for LES— stable, unstable and neutral, and increase of Γ for M94 from 0 to 4).

The anisotropy tensor was also calculated from high temporal and spatial resolution LES of the atmospheric boundary layer over flat, homogeneous terrain for varying stability from NCAR, kindly provided by Ned Patton (see Chougule et al. [2012]). The calculations are done for three different stability cases: moderately stable ($z_i/L_o = 2$), unstable ($z_i/L_o = -10$) and neutral ($z_i/L_o = 0$), where z_i is boundary layer depth. The LES dataset consists of instantaneous three-dimensional fields, between heights 50 to 150 m. The variance and covariance are calculated for each stability case for each snapshot and at each z level in horizontal slice and then averaged over all snapshots. The results are plotted as shown in Figure 15. More details on the LES data can be found in Chougule et al. [2012].

The LES neutral data falls closer to the curve which corresponds to values of Γ between 3-4. The deficiency of M94 can be observed when compared with unstable LES. The stable LES crosses the curve. The origin in Lumley triangle represents isotropic turbulence where anisotropy tensor is zero ($p = q = 0$). This state of isotropic turbulence corresponds to $\Gamma = 0$ on the curve. In addition to the Γ parameter, b_{ij} from the spectral tensor model with buoyancy effects, which is described in Chapter 3, would become function of Ri using MOST, which can be seen from Equation 3.89.

Bibliography

R.A. Antonia and R.E. Luxton. The response of a turbulent boundary layer to a step change in surface roughness. part 2. rough-to-smooth. *J. Fluid Mech.*, 53(4):737–757, 1972. 31

G. K. Batchelor. *The theory of homogeneous turbulence*. Cambridge University Press, UK, 1953. 40

H. Bergström, H. Alfredsson, J. Arnqvist, I. Carlén, E. Dellwik, J. Fransson, H. Ganander, Matthias Mohr, A. Segalini, and Stefan Söderberg. Wind power in forests: Winds and effects on loads. Report, March 2013. http://www.elforsk.se/Global/Vindforsk/Rapporterts.pdf. 17, 31

J. A. Businger, J. C. Wyngaard, Z. Y. Izumi, and E. F. Bradley. Flux-profile relationships in the atmospheric surface layer. *J. Atmos. Sci.*, 28:181–189, March 1971. 69

A. Chougule, J. Mann, M. Kelly, J. Sun, D. H. Lenschow, and E. G. Patton. Vertical cross-spectral phases in neutral atmospheric flow. *J. Turbul.*, 13(36):1–13, 2012. 1, 3, 10, 11, 14, 16, 29, 61, 67, 92

A. G. Davenport. The spectrum of horizontal gustiness near the ground in high winds. *Q. J. R. Meteorol. Soc.*, 87:194–211. 13

SE. Gryning, E. Batchvarova, B. Brümmer, H Jørgensen, and S Larsen. On the extension of the wind profile over homogeneous terrain beyond the surface boundary layer. *Bound. Layer Meteorol.*, 124:251–268, 2007. 5, 16, 60

H. Hanazaki and J. C. R. Hunt. Linear processes in unsteady stably stratified turbulence. *J. Fluid Mech.*, 318:303–337, 1996. 14, 36

H. Hanazaki and J. C. R. Hunt. Structure of unsteady stably stratified turbulence with mean shear. *J. Fluid Mech.*, 507:1–42, 2004. 14, 36, 55

T. R. Heidrick, S. Banerjee, and R. S. Azad. Experiments on the structure of turbulence in fully developed pipe flow: interpretation of the measurements by a wave model. *J. Fluid Mech.*, 81:137–154, 1977. 2

IEC. Wind turbines - part 1: Design requirements. Technical Report IEC 61400-1, 2005. 2, 14, 35

J. C. Kaimal and J. J. Finnigan. *Atmospheric boundary layer flows*. Oxford University Press, New York, 1994. x, 13, 16, 31, 34, 35, 37, 50, 52, 67, 68, 69

J. C. Kaimal, J. C. Wyngaard, Y. Izumi, and O. R. Coté. Spectral characteristics of surface-layer turbulence. *Q. J. R. Meteorol. Soc.*, 98(417):563–589, 1972. doi:10.1002/qj.49709841707. 13, 14, 16, 35, 52, 60

S. Komori, H. Ueda, F. Ogino, and T. Mizushina. Turbulence structure in stably stratified open-channel flow. *J. Fluid Mech.*, 130:13–26, 1983. 2

L. Kristensen and P. Kirkegaard. Sampling problems with spectral coherence. Risø report Risø-R-526, February 1986. 13, 32

L. Kristensen, D. H. Lenschow, P. Kirkegaard, and M. Courtney. The spectral velocity tensor for homogeneous boundary-layer turbulence. *Bound. Layer Meteorol.*, 47: 149–193, 1989. 13, 14, 35

J. Mann. Models in micrometeorology. PhD Thesis Risø Rep. R-727(EN), University of Aalborg, 1994a. 1, 2, 6, 7, 14, 35, 37, 69, 74

J. Mann. The spatial structure of neutral atmospheric surface-layer turbulence. *J. Fluid Mech.*, 273:141–168, 1994b. ix, 13, 16, 31, 35, 58, 59

J. Mann. Wind field simulation. *Prob. Engng. Mech.*, 13(4):269–282, 1998. 2, 14, 35

J. Mann. The spectral velocity tensor in moderately complex terrain. *J. Wind Eng. and Ind. Aero.*, 88:153–169, 2000. 6

M. R. Maxey. Distortion of turbulence in flows with parallel streamlines. *J. Fluid Mech.*, 124:261–282, 1982. 14, 36

A. Peña, SE. Gryning, and J. Mann. On the length-scale of the wind profile. *Q. J. R. Meteorol. Soc.*, 136:2119–2131, October 2010a. 14, 36

A. Peña, SE. Gryning, J. Mann, and C. B. Hasager. Length scales of the neutral wind profile over homogeneous terrain. *J. Appl. Meteor. Climat.*, 49:792–806, 2010b. 14

S. B. Pope. *Turbulent flows*. Cambridge University Press, UK, 1st edition, August 2000. 2, 13, 35, 37, 40, 49, 51, 52, 90, 92

G. S. Poulos, W. Blumen, D. C. Fritts, J. K. Lundquist, J. Sun, S. P. Burns, C. Nappo, R. Banta, R. Newsom, J. Cuxart, E. Terradellas, B. Balsley, and M. Jensen. Cases-99: A comprehensive investigation of the stable nocturnal boundary layer. *Bull. Amer. Meteor. Soc.*, 83:555–581, 2002. 1

W. H. Press, S. A. Teukolsky, W. T. Vetterling, and B. P. Flannery. *Numerical recipes: The art of scientific computing*. Cambridge University Press, New York, 3 edition, 2007. 54

A. Sathe, J. Mann, J. Gottschall, and M. S. Courtney. Can wind lidars measure turbulence? *J. Atmos. Oceanic. Technol.*, 28(7):853–868. 4, 18, 61

A. Sathe, J. Mann, T. Barlas, W. A. A. M. Bierbooms, and G. J. W. van Bussel. Influence of atmospheric stability on wind turbine loads. *Wind Energy*, 2012. DOI: dx.doi.org/10.1002/we.1528. 1, 4, 11, 14, 18, 30, 36, 61

R. B. Stull. *An introduction to boundary layer meteorology*, volume 13. Springer, 2009. 37, 42

J. Sun, S. P. Burns, D. H. Lenschow, R. Banta, R. Newsom, R. Coulter, S. Fraiser, C. Nappo, J. Cuxart, W. Blumen, X. Lee, and Xin-Z. Hu. Intermittent turbulence associated with a density current passage in the stable boundary layer. *Bound.-Layer Meteorol.*, 105:199–219, 2002. 1

H. Tennekes and J. L. Lumley. *A first course in turbulence*. MIT Press, Cambridge, 1972. 13

C. Tong and J. C. Wyngaard. Two-point coherence in the atmospheric surface layer. *Bound. Layer Meteorol.*, 81:105–121, 1996. 1, 13

A. A. Townsend. *The structure of turbulent shear flow*. Cambridge University Press, UK, 2nd edition, 1976. 2, 13, 35

P. S. Veers. Modeling stochastic wind loads on vertical axis wind turbines. Technical Report SAND88-1909, Sandia National Laboratories, September 1984. 2

P. S. Veers. Three-dimensional wind simulation. Technical Report SAND88-0152, Sandia National Laboratories, March 1988. 2, 13, 14, 15

T. von Kármán. Progress in the statistical theory of turbulence. *Proc. Nat. Acad. Sci.*, 34:530–539, 1948. 6, 19

J. C. Wyngaard. *Turbulence in the atmosphere*. Cambridge University Press, UK, 2010. 37, 43